ON THE DARK MOLECULAR GAS AS REVEALED BY 18CM OH EMISSION

by

Michael Peter Busch

A dissertation submitted to Johns Hopkins University
in conformity with the requirements for the degree of
Doctor of Philosophy

Baltimore, Maryland
January, 2022

Abstract

We explore the use of the 18cm hydroxyl (OH) lines as a novel tool for observing and characterizing molecular gas on Galactic (kpc) scales. We report the results from a highly sensitive ($\Delta T_{\mathrm{mb}} \sim$ 3mK) survey for thermal OH emission at 1665 and 1667 MHz over a dense, 9 x 9-pixel grid covering a $1^\circ \times 1^\circ$ patch of sky in the direction the Perseus spiral arm of our Galaxy. We explore the possible physical conditions of the observed features using a set of diffuse molecular cloud models. Both OH and CO emission disappear at current sensitivity limits below an $\mathrm{A_v}$ of 0.2 mag. CO emission does not appear in the context of the models unless the volume density exceeds 100-200 cm^{-3}. These results demonstrate that a combination of low column density ($\mathrm{A_v}$) and low volume density (n_{H}) can explain the lack of CO emission along sight lines exhibiting OH emission. We then present the serendipitous discovery of an extremely broad ($\Delta V_{\mathrm{LSR}} \sim$ 150 km s^{-1}), faint ($T_{\mathrm{mb}} <$ 10mK), and ubiquitous 1667 and 1665 MHz ground-state thermal OH emission towards the 2nd quadrant of the outer Galaxy ($R_{\mathrm{gal}} > 8$ kpc) with the Green Bank Telescope. The longitude-velocity distribution of the emission unambiguously suggests large-scale Galactic structure. Our results imply the existence of a thick ($-200 < z < 200$ pc) disk of diffuse ($n_{\mathrm{H_2}} \sim 5 \times 10^{-3}$ cm^{-3}) molecular gas in the Outer Galaxy previously undetected in all-sky CO surveys. Finally, we present the first extragalactic detection of thermal, ground-state 18cm (1667 and 1665 MHz) OH emission from the Southern galactic disk of M31. The velocity distribution of the OH emission is found to be similar to the HI distribution. At face value, these results may indicate the ubiquity of abundant ‘CO-dark‘ molecular gas at large galactic radii in spiral galaxies. We conclude this thesis with a technical overview of the field of radio observations of 18cm OH as a molecular gas tracer in the future and review upcoming telescopes which may enable large surveys of faint OH emission in the future.

Primary Reader: Joshua Peek
Secondary Reader: David Neufeld

Dedication

To my family: Dad, Mom, Ron, Jen and Ken.

What an adventure we have all had.

Acknowledgements

Someone much wiser than myself once said that it takes a village to raise a child. I can think of no more appropriate proverb to describe my journey of receiving a Ph.D in astrophysics. This is a journey I have been on for practically my entire life–ever since I was exposed to the vastness of the universe when I was five years old at a planetarium show at Griffith Observatory, and I have had so many mentors and friends to help me along the way that I fear I may not be able to list every single person that has impacted me–just know that you are loved and appreciated and you know who you are.

I would like to start by thanking and remembering my late Ph.D. advisor, Ronald J. Allen. Ron gave me the opportunity to work in the field of molecular astrophysics through the lens of radio astronomy, even though at our first meeting I confessed I wasn't really interested in molecular astrophysics–and that I was *dedicated* to observational cosmology. Perhaps sensing my future trajectory, Ron gave a knowing grin and said, "Sure, why not." and allowed me to be his student of radio astronomy and molecules anyway. In those years that I worked with Ron, I grew so much as a scientist and astronomer. He was also the mentor and friend I needed at that exact time of my Ph.D career–when I was having so much trouble with it and was contemplating leaving the program altogether. We had many adventures together, most of which comprised of formulating theories of what one might see with the Green Bank Telescope given a set of observational parameters, then getting in his car and driving for five hours to Green Bank and setting up the observations of the OH molecule and carrying it out through many observing nights. It was in this way that we discovered together the realization that the "disk" of OH emission in the outer galaxy was indeed real–when the emission obeyed simple laws of galactic geometry. "Always do your physics before your observations." Was his favorite saying to students. I will miss him dearly. To Jan Allen and the Allen family; thank you for letting me grieve Ron's passing with you. He was the type of scientist I would like to emulate, and it was an honor being his student.

Secondly, I would like to thank the plethora advisors and mentors who came to offer support and aid after Ron passed. There are so many of you and you helped me tremendously during a trying time. Specifically, Susan Kassin, Christine Chen, Ken Sembach, David Neufeld, Toby Marriage, Colin Norman and Nadia Zakamska. Those first few months without Ron's guidance were extremely tough.

It wasn't until Josh Peek accepted me under his wing as a student–an arrangement that Susan Kassin suggested–that I gained my "sea legs" again so-to-speak, and began to do science confidently again. Josh accepted me as a "late stage graduate student" graciously, and helped me in so many ways only an advisor can: helping draft emails to potential postdoc advisors, making sure I traveled to relevant conferences, talking to me about my science and bouncing ideas off of each other on his backyard deck. I am indebted to him for offering his time, support and guidance to my career when I needed it the most.

I would also like to thank the many, many friends and colleagues who helped me along the way. Firstly, I'd like to thank the colleagues I have worked with during the course of my thesis. To Philip Engelke and Dave Hogg, thank you for the exhilarating run we had observing OH at the Green Bank Observatory and the discoveries we all made together. I am very proud of the work we have achieved together with Ron.

To the friends and colleagues in my field that I have made along the way, thank you for your scientific discourse and insight whenever I needed it: to Josh Peek, Colin Norman, David Neufeld, Mark Wolfire, Karl Menten, Jo Dawson, Jay Lockman, Anita Peltzer, Claire Murray, Enrico Di Teodoro, Arshia Jacob, Michael Rugel, Katie Jameson, Kendall Hall, Christina Willecke, Catherine Zucker, Pedro Salas, Kimberly Emig and probably many others– thank you. To the entire scientific staff and control room observers at the Green Bank Observatory, thank you for sharing your knowledge and insight with me as well.

My journey has been made easier thanks to being blessed with many friends in my life. Thanking all of them here would be impossible, but you should all know that I appreciate every single one of you. In my cohort: Bingjie, Hsiang-Chih, Alex, Peter, Tom, Josh, Lucas, Oz and Weichen. In the department (and those that have graduated before me): Erini, Duncan, Raymond, Kim, Jose, Ryan, Thomas, Alvin, Yasuo, Bastian, Rocio, Liza, and

Chris. Outside the department: Tim, Raeid, Myles, Jack, Jaime, and Amartya. To my online friends in the Batleth Discord, thanks for all the laughs. To the forsilvra.net community, thanks for being my creative writing outlet. My many thanks to Brendan White for being my best friend for many years now.

Last but not least, I must thank my parents and family. My Dad and Mom raised me with a healthy respect for receiving higher education, having never had much opportunities in education themselves. My father never went to college and my mother, who emigrated at a very young age from Mexico, never finished high school–but they taught me my most important lessons as only parents could. To them I owe my tenacity, determination, perseverance and spirit. Along with those lessons and their unconditional love, support and encouragements, my parents and siblings have been a constant source in my life and I couldn't have completed this academic journey without them.

Table of Contents

List of Tables

List of Figures

Chapter 1

Introduction

1.1 Overview

To the unaided eye, it may seem like the space between stars is empty and void. For most of recorded history the field of astronomy has concerned itself with the cataloging of bright celestial objects that move or appear in the sky. In reality, interstellar space is not a complete state of vacuum. This space between stars, and the material in it is collectively known as the interstellar medium (ISM). The ISM is an incredibly dynamic place, with gaseous material and dust in many phases of temperature and density. The interplay between the different phases of the ISM plays a fundamental role in how galaxies appear to us, how stars form, and how energy is transported in the galaxy. The distribution of gas in the galaxy informs our knowledge of star formation history, as gas is the fuel for molecular clouds to form. It is in the cold and dense molecular clouds that the required densities where stars can finally form. The elements the gas is comprised of can come in forms of ionized, atomic or molecular, the constituents of the mass of the ISM is summarized

Phase	M (10^9 $M_\odot$)	fraction
Total Ionized Hydrogen (HII)	1.12	23%
Total Atomic Hydrogen (HI)	2.9	60%
Total Molecular Hydrogen (H_2)	0.84	17%
Total HII, HI, and H_2	4.9	
Total Gas (including He)	6.7	

Table 1.1: Constituent mass of HI, HII and H_2 in the Milky Way's ISM (R < 20kpc), adapted from Draine (2011).

in 1.1. The study and understanding of the ISM is thus imperative for many fields of astronomy.

Because stars are typically created in molecular clouds the enterprise of observing molecules in the galaxy became important to the overall understanding of the galactic ecosystem. Unfortunately for astronomers, the most abundant molecule is molecular hydrogen (H_2), and as a symmetric molecule with no dipole moment, the allowed quadrupole radiation at 28μm ($h\nu/k_B \sim$ 500 K) occur at energies much too energetic to be present at the cold quiescent molecular phase of the ISM, where the temperatures are below regularly 100K. The solution for observing the bulk of molecular gas in the galaxy, and in other galaxies, has been for some time to observe trace molecules, assumed to be well-mixed with H_2 and apply either a mass-to-light ratio (in the case of CO) or an abundance ratio of the molecules to estimate the content of H_2.

1.2 The Dark Molecular Gas and This Thesis

The CO molecule has for years been the workhorse for tracing the bulk of the molecular gas content in our galaxy and others, and for good reason, CO is bright and abundant and easily observable from ground based millimetre observatories at the J=1-0 3mm rotational line. There is, however, convincing evidence that CO does not trace *all* of the molecular gas. Grenier, Casandjian, and Terrier (2005) coined the term *dark molecular gas* for this phase of molecules not well traced by CO, but early evidence hinted at this phenomenon even earlier Blitz, Bazell, and Desert (1990). Research into this phenomenon has suggested that the gas not traced well by CO is diffuse molecular gas, where the CO molecule is either not collisionally excited or shielded by ionizing photons from the ambient ISM (Wolfire, Hollenbach, and McKee, 2010; Planck Collaboration et al., 2011; Murray et al., 2018; Seifried et al., 2019).

The main scientific goal of this thesis is to pioneer the use of the molecule OH to search for molecular gas in extremely diffuse phases of the ISM, where the canonical observational method of observing the CO molecule appears to fail to trace a large fraction of H_2 in this environment. The thesis is presented in three major chapters.

First, we present a survey completed with the Green Bank 100m Telescope of the 18cm OH emission towards the Perseus Arm region of the Outer Galaxy. The main goal of this chapter was map the structure of the OH emission and compare it to that of the CO emission. The survey is called (unimaginatively) the "One-Square-Degree" survey because it covers one square degree of sky. The observed OH and CO profiles are presented in a heat map to show that the detectable OH extends to far greater spatial extents than the CO in this region. Physical models to deduce the conditions of the gas are also presented. The goal of the chapter is so ascertain why OH is a good tracer of H_2 in regions where CO is not, and to present observations that fueled this conjecture. The first chapter of this thesis is published in *The Astrophysical Journal* as a paper titled, ’The Structure of Dark Molecular Gas in the Galaxy. II. Physical State of "CO-dark" Gas in the Perseus Arm’ (Busch et al., 2019), with formatting revisions to adapt to the requirements of the thesis

Next, we present the discovery of a large 18cm OH emission structure towards the Outer Galaxy, found (mainly) accidentally with the Green Bank 100m Telescope and later confirmed with the 20m telescope at the Green Bank Observatory (GBO). The discovery spectra are presented, along with initial analysis of follow-up in galactic longitude to show that the emission obeys simple laws of galactic structure, suggesting that the OH structure is incredibly large and present throughout the entire outer galaxy. While completely undetected in CO surveys, this discovery may indicate a large amount of molecular gas hidden in extremely low density environments. This chapter was published in *The Astrophysical Journal* titled, ’Observational Evidence for a Thick Disk of Dark Molecular Gas in the Outer Galaxy’ (Busch et al., 2021), with formatting revisions to adapt to the requirements of the thesis.

Finally, we present the first detection of 18cm thermal OH emission in another galaxy for the first time. While OH has been detected in *absorption* towards bright background sources, it has never been detected in the emission from the ground state in another galaxy. The discovery spectra from, once again, the Green Bank 100m Telescope are presented and discussed along with the comparable archival CO spectrum. The detection was towards one pointing in the outer parts of the southern disk of M31 (Andromeda), with follow up planned. This chapter opens the door for the use of OH as an extragalactic tracer of dark molecular gas. At the time of writing a manuscript is in preparation for submission to an astronomical journal.

References

Blitz, L., D. Bazell, and F. X. Desert (1990). *ApJ* 352, p. L13.

Busch, M. P. et al. (2019). *ApJ* 883.2, p. 158.

Busch, M. P. et al. (2021). *ApJ* 914.1, p. 12.

Draine, B. T. (2011). Princeton University Press, p. 540.

Grenier, I. A., J.-M. Casandjian, and R. Terrier (2005). *Sci* 307.5713, pp. 1292–1295.

Murray, C. E. et al. (2018). *ApJ* 862.

Planck Collaboration et al. (2011). *A&A* 536, p. 16.

Seifried, D. et al. (2019).

Wolfire, M. G., D. Hollenbach, and C. F. McKee (2010). *ApJ* 716.2.

Chapter 2

The Structure of Dark Molecular Gas in the Galaxy: The Green Bank Telescope "One-Square-Degree" Survey for 18cm OH

2.1 Introduction

The formation of molecular hydrogen gas H_2 from atomic hydrogen H I in galaxies is widely considered to be a critical step for the formation of new stars from the interstellar gas, and hence it is one of the most important processes that occurs in the interstellar medium (ISM). Unfortunately, as a symmetric molecule without a dipole moment, H_2 is practically invisible in emission at the temperature range of 10-100K expected for the bulk of the ISM in the Galaxy, and indirect estimates are required that make use of surrogate tracers. The most universally-accepted surrogate tracer for H_2 in the ISM is the lowest-energy rotational spectral line of ^{12}CO(1-0) at $\lambda = 3$mm. This line is relatively bright and easily observed, often with instrumentation designed specifically for that purpose. CO observations are commonly used jointly with an empirically-derived conversion factor, usually called the "X-factor" (see Bolatto, Wolfire, and Leroy, 2013, for a review). The strength of the 3-mm CO line emission is measured in units of K km s^{-1} and, by multiplying this line strength by the X-factor, one directly obtains an estimate of the H_2 column density. Under a number of assumptions, this conversion factor has an estimated uncertainty of about 30%.

A growing body of observational evidence points to an extra component of the ISM not traced by either the 21-cm H I line or ^{12}CO(1-0) emission. This excess component is usually referred to as "dark gas" (Grenier, Casandjian, and Terrier, 2005; Wolfire, Hollenbach, and McKee, 2010). This dark gas may be a large fraction of the total molecular gas content in the Galaxy (Pineda et al., 2013; Li et al., 2015). Quantifying how much dark gas exists is therefore of great interest in an effort to calibrate the X-factor and work towards a single prescription for scaling between a molecular tracer line emission and an accurate total molecular mass of H_2. Wolfire, Hollenbach, and McKee (2010) constructed models of molecular cloud surfaces and determined that dark gas in molecular cloud surfaces can amount to $\sim$ 30% of the total molecular mass of the cloud. Here, the column density is large enough so that H_2 has sufficient column to remain self-shielded against the ambient UV flux, but CO is photodissociated and the carbon is the form of C or C^+. However, a large fraction of the faint CO gas might also arise in the diffuse ISM (Papadopoulos, Thi, and Viti, 2002; Liszt, Pety, and Lucas, 2010; Allen et al., 2012; Allen, Hogg, and Engelke, 2015; Xu et al., 2016a).

Initially discovered in absorption at centimeter radio wavelengths in the diffuse ISM[1], OH has also recently been detected in the far-IR (Wiesemeyer et al., 2016), also in absorption. The work reported here mainly concerns new 18-cm emission observations in the outer Galaxy. Allen et al., 2012 reported faint and widespread 18-cm OH emission in a blind survey of a small region in the second quadrant of the Galactic plane using the 25-m radio telescope at Onsala, Sweden. However, owing to spectrometer limitations and radio interference in the spectra, the Onsala blind survey was limited to the 1667 MHz OH line and to within 2 kpc of the Sun. Similar results were presented by Dawson et al., 2014 with the SPLASH survey using the Parkes Telescope; however, their survey of OH encountered high levels of background synchrotron continuum emission from the inner Galaxy at levels approaching the typical excitation temperatures of the 18-cm OH lines, effectively suppressing the extended OH emission outside of the 'CO-bright' clouds. In the outer Galaxy, we can typically avoid this issue as the integrated background synchrotron emission is much weaker. More recent observations in the outer Galaxy by Allen, Hogg, and Engelke (2015, hereafter Paper 1) using the GBT have shown main-line (1665 and 1667 MHz) OH emission to be present in regions largely devoid of CO emission, strongly suggesting that OH may be a good tracer of the dark gas. The main lines of OH emission in these regions are observed to be in the 5:9 ratio characteristic of optically-thin emission lines with level populations in local thermodynamic equilibrium (LTE). This makes calculating a column density of OH relatively straightforward as long as a good estimate for the

---

[1] Additional historical information on the discovery and early observations of the 18-cm radio lines of OH both in emission and absorption can be found in Allen et al., 2012 and Allen, Hogg, and Engelke, 2015.

excitation temperatures can be found. With an OH column density known from emission observations, the H_2 column density can be directly estimated using the $N(H_2)/N(OH)$ ratio of approximately 10^{-7} measured from UV absorption data (Weselak et al., 2010; Nguyen et al., 2018; Engelke and Allen, 2018).

In this paper we present the results of a densely-sampled, blind, highly-sensitive GBT emission survey of the two main OH lines in a one-square-degree field of the Perseus Arm. The purpose of this survey is to further explore the apparent connection of extended OH emission to the so-called 'dark molecular gas', and attempt to resolve structures of diffuse molecular gas on a large scale that are otherwise invisible to CO observations.

In Paper 1, we were able to compare sparse OH survey measurements taken with the GBT (FWHM $\sim 7.6'$) with spectra provided directly from archives of the CFA CO survey (Dame, Hartmann, and Thaddeus, 2001), since both data sets were observed at closely similar angular resolution ($\sim 7.6'$ for the GBT vs $\sim 8.4'$ for the CfA telescopes). However, the Five College Radio Astronomy Observatory (FCRAO) ^{12}CO "Outer Galaxy Survey" (Heyer et al., 1998) has significantly higher angular resolution ($\sim 50''$) than the CFA ^{12}CO survey, and hence significantly better sensitivity when smoothed to the GBT beam. We have therefore compared our OH data with a smoothed version of the FCRAO data. This allows for a direct, dense, observational comparison between these two important molecular tracers with comparable sensitivities for the first time.

It was observed in Paper 1 that OH emission was widespread, and that there was varying structure to the emission profiles on scales of ~ 30 pc at the distance of the Perseus Arm feature. In an attempt to resolve the structure of this emission a new observing program was undertaken to increase the coverage of the original 2015 sparse survey. In this paper we therefore chose to restrict our analysis to the Perseus Arm feature in particular in an attempt to map the OH emission spatially and compare it to the CO emission at the ~ 7 pc scale, as we show in Sect. 2.4.2. Due to the absence of the kinematic distance ambiguity in the outer Galaxy, we are able to differentiate components of the OH spectra (see Fig. 2.2). The distance of the Perseus Arm offered us the best consistently apparent option to measure this structure. The availability of accurate parallax distances in this direction (see Sect. 2.2.4) made this spatial comparison possible. Statistical and spatial comparisons of OH and CO emission between the local and inter-arm features would also be interesting and will be the subject of future papers.

2.2 Observations and Data

We carried out highly-sensitive observations of main-line OH emission at 18 cm with the Robert C. Byrd Green Bank Telescope (GBT) in project AGBT14B_031 at the 81 locations indicated with small circles in Fig.2.1. For comparison with the OH data, we used the ^{12}CO(1-0) data from the FCRAO survey, as explained above.

2.2.1 OH Observations

Paper 1 reported the results of a ′sparse′ survey with the GBT at 0.5° spacing interval at sightlines indicated with "X" in Fig.2.1. The observations discussed in this paper were made between September 11, 2015 and January 31, 2016, also with the GBT. The receivers selected are situated at the Gregorian Focus and operate in the frequency range 1.15 to 1.73 GHz (L-Band). There is one beam on the sky, with dual polarizations. The amplifiers are cooled Field Effect Transistors (FET) with an effective system temperature of 20 K or less in good weather and for intermediate elevations of the GBT. These observations were made with linear polarization.

In particular, an unanticipated but significant amount of observing time was obtained in irregular periods beginning in December 2013 and finally completed in August 2015 with the GBT under project number AGBT14B_031B, providing a highly-sensitive ($\Delta T_{mb} \sim 3.0 - 3.5 mK$ in 0.55 km/s channels) survey with unprecedented detail over a one-square-degree (OSD) patch of sky in the direction of the Outer Galaxy.

The spectrometer employed to measure the spectra was Vegas (Prestage et al., 2015), an extremely versatile FPGA-based instrument which can be deployed in a variety of configurations. In the present application eight bands were centered on 1420.405 MHz, 1617.40 MHz, 1666.400 MHz, and 1720.530 MHz, providing polarization data on neutral Hydrogen, the two main OH lines at 1665.401 MHz and 1667.358 MHz, and the two satellite lines of OH at 1612.231 MHz and 1720.533 MHz. Each band contained 16384 channels of width 1.0300 KHz(0.1853 km/s at 1666 MHz; 0.2174 km/s at 1420 MHz).

Observations were made in the frequency-switching mode because of the potential difficulty in locating a nearby reference position which would be free of an OH signal. Switching was done +/- 2 MHz with respect to the center frequency. For the mainlines of OH the center frequency was chosen such that the two lines were included in each of the two switching cycles in order to improve the integration time by a factor of two. The resulting spectrum is approximately 12.8 MHz in width. For the main lines of OH this spectrum lies between 1660.0 and 1672.8 MHz.

The observations were taken using the L-band wide receiver system operating in the frequency range of 1.15 - 1.74 GHz. The receiver is a single-beam, dual polarization instrument with an effective system temperature ranging from 16 - 20K depending on weather and the Galactic background continuum. A bandwidth of 12.5 MHz is chosen to minimize the appearance of radio frequency interference.

This new OSD survey covers a 9×9 grid of GBT sightlines, which roughly corresponds to 60×60 pc region at a 3.2 kpc distance to the Perseus Arm, centered on $l = 105.0^\circ$, $b = 2.5^\circ$ and at intervals of $0.125^\circ = 7.5'$, closely corresponding to the angular resolution of the GBT at the frequency of the OH main lines (FWHM $\sim 7.6'$). At each position 12 individual scans, each of duration 10 minutes, were made. For an individual scan, in one polarization, the effective integration time was approximately 292 seconds, and the expected rms in a single channel in the corresponding spectrum is approximately 34 mK. The effective integration time of the final spectrum after combination of the data from all scans, in both polarizations, is just under two hours.

2.2.2 Archival CO Data

The ^{12}CO(1-0) observations were made between 1995 and 1998 using the 14m telescope of the FCRAO (Heyer et al., 1998). This FCRAO "Outer Galaxy Survey" observed a 336 square degree region of the second quadrant of the Galaxy sampled at 50$''$ intervals with a FWHM beamwidth resolution of 45$''$. For the purposes of our direct comparison, this survey was first smoothed to the GBT resolution. The final CO spectra have a sensitivity of 60 to 100 mK rms, and a velocity resolution of 0.8 km s^{-1}.

2.2.3 Data Reduction

The GBT OH data were reduced using the *GBTIDL* software (Garwood et al., 2006). The quality of this data is generally very high, and each polarization of each 10 minute scan was reviewed for the presence of radio frequency interference and problems from instrumental effects. It was quickly evident that the spectra would be heavily influenced by the baseline ripple discovered during commissioning of the GBT (Fisher, J. R., Norrod, R.D., and Balser, D.S. 2003, Electronic Division Internal Report No. 312). The dominant feature is a broad ripple with an approximate periodicity of 9 MHz. Fisher et al. deduce that this ripple is caused by multipath reflections in which a part of the system noise enters the receiver system directly and a part is returned from the subreflector. Typical values of the amplitude are 0.4 K in Y and 0.1 K in X, the orthogonal polarized channel. Because the periodicity of this ripple is much larger than the frequency range expected for the OH signal, the ripple can in general be satisfactorily removed by fitting and subtracting a polynomial of low order to the baseline.

The residual spectrum shows an additional ripple feature that is more problematic. This ripple is comprised of several components having frequencies in a range between 1.3 and 1.8 MHz according to Fisher et al. The ripple is stronger in the Y polarization, is variable with a dependence on the configuration of the main reflector and the subreflector, and is presumed to also arise in multipath reflections from the circumferential gaps between the surface panels. The amplitude of the ripple is larger in the Y linear polarization whose E-vector is parallel to the plane of symmetry of the telescope. Typical worst case amplitudes are about ±1.5 mK in the Y polarization. The placement of the pattern in the bandpass is a strong function of the position of the subreflector. An attempt was made to reduce the amplitude of the ripple by observing the same position with the subreflector set at focus positions differing by $\lambda/8$. Some improvement was noted, but the ripple was never completely canceled out.

All of the data for a given position were assembled and reviewed for quality. Where necessary, data contaminated by (infrequent) interference or equipment instability were edited out. The data for each polarization were averaged, and the 9 MHz ripple was removed by fitting a baseline polynomial of order 5 to the spectrum in the frequency range 1661.4 MHz to 1671.4 MHz. Each spectrum was then used to compare the 1667 and 1665 MHz lines to judge if the emission is in LTE line ratio. The relative intensities of the four lines are 1:5:9:1 for the 1612-, 1665-, 1667-, and 1720-MHz lines respectively. Instances where the ratio differed from the LTE value proved to be rare. The comparison of the two spectra also provided a useful validation of faint spectral features.

The next step was to average the two polarizations in order to improve S/N, and to smooth the data by a Gaussian function to an effective spectral resolution of 1.0 km s^{-1}. For these spectra the rms of an individual point is 2.2 mK, but there is variation from spectrum to spectrum because of the remaining uncertainty in the determination of the baseline. Including baseline uncertainties, the resultant RMS uncertainty in the OH spectra is on the order of 3mK in T_{mb} units. The final spectrum was shifted to the rest frame velocity of the 1665 or 1667 MHz line for further detailed parameterization. An example spectrum from the OSD is shown in Fig. 2.2, the OH emission from the local gas, inter-arm, and Perseus spiral arm are observed at $V_{LSR} \sim 0$, -20 and -65 km s^{-1} respectively.

The final step was to make the best estimate of OH emission from the Perseus Arm Region. We assumed that emission from the Perseus Arm would be limited to a spectral region of width 25 km/s centered on the expected velocity. For the expected velocity we were guided by the profile of the neutral hydrogen as mapped in the DRAO "LRDS" survey, in the vicinity of -75 to -50 km s^{-1} (Higgs and Tapping, 2000; Higgs et al., 2005)

To remove the residual effects of the 1.6 MHz ripple we defined two regions proximate to the OH window, each of width 10 km/s, and fitted a linear baseline to these regions. At the same time the CO emission from the region is computed from the archival data from the FCRAO (Heyer et al., 1998) over the same velocity range.

A 9 MHz spectral ripple is removed by a high-order polynomial fit to the spectra in places where signal is absent. We note that a shorter, low-noise ripple on the order of 1.5 MHz is present that we have not yet found a way to subtract confidently. As such the GBT is currently limited to $\triangle T_{mb} \sim 3.0 - 3.5mK$, and further integration would not lower the error below this instrumental threshold.

The finished products from the ^{12}CO data sometimes suffer from a long-wavelength ripple in the spectra, which has been removed by a similar polynomial fit. However, negative values are sometimes recovered owing to the variation in spectra where there is no CO signal (as is the case in most of the sightlines in the area studied here), see e.g. Figure 1 in Heyer et al., 1998, where there is a demonstrative negative feature, a probable artifact of this baseline ripple, at roughly the Perseus Arm velocity range.

2.2.4 Distance to the Perseus Arm

The physical size of the Perseus Arm structures that we are observing are known from precise VLBI distance measurements (Reid et al., 2009; Reid et al., 2014; Choi et al., 2014). In the direction of $l = 105.00°, b = +2.50°$ we use the Bayesian Distance Calculator[2] from The Bar and Spiral Structure Legacy Survey (BeSSeL) (Reid et al., 2016) to estimate the distance to our observed Perseus Arm sources. We note that the galactic rotation model utilized by the BeSSeL project does not incorporate the so-called “rolling motions” of the Perseus Arm (Yuan and Wallace, 1973; Foster and Cooper, 2010), and that the Bayesian Distance Calculator treats the Perseus Arm V_{LSR} as constant

---

[2] http://bessel.vlbi-astrometry.org/bayesian

with galactic latitude. While many of our observed features at high latitudes contain LSR radial velocities inconsistent with the Perseus Arm V_{LSR} range provided by the BeSSeL model, we believe that rolling motions account for this variation in V_{LSR} and that our observed features do indeed fall within the Perseus Arm. We therefore use the parallax distances from the calculator as opposed to the kinematic distance PDF; we adopt a distance estimate of 3.2 kpc to the Perseus Arm. As noted in the previous section, any feature we observe in the vicinity of -75 to -50 km s^{-1} we associate with the Perseus Arm.

2.2.5 Determining Line Strengths

The line strengths of all features corresponding to the Perseus Arm velocity interval ($V_{LSR} \sim -65$ km s^{-1}, see Fig. 2.2) of the 81 1667 MHz OH spectra in the survey were calculated. The line profile strengths of the CO and OH lines are plotted against each other in Fig. 2.3. All 81 Perseus features in the OH spectra were manually identified and the velocity range's integration limits were chosen from visual inspection of the OH spectra. The corresponding line strengths from the CO spectra were obtained over the same velocity range. The expression used to calculate the line strengths is:

$$S = \sum T_{mb} \times \Delta V, \tag{2.1}$$

in units of K km s^{-1}, where T_{mb} is in units of main-beam brightness temperature, and ΔV is the channel spacing of the data. Note that, for the GBT, T_a and T_{mb} are the same to within 5%. The summation is done numerically over the channels containing measurable signal for each Perseus Arm feature in the 81 OH spectra. After this process, the ^{12}CO(1-0) spectrum is extracted from a spatially-smoothed version of the FCRAO data cube and integrated over the same velocity range. This process was repeated for all 81 Perseus Arm features (and lack of features around $V_{LSR} \sim -65$ km s^{-1}) until all of the data in the OSD was processed. The error analysis is the same procedure as outlined in Allen, Hogg, and Engelke, 2015 section 4.2. We also computed the scaled difference between the 1665 and 1667 MHz lines with each sightline and find that most emission is the LTE ratio of 5:9, as is expected if these lines are excited chiefly by collisions.

2.2.6 Estimating the Continuum and Excitation Temperatures

In order to fit our OH observations and the corresponding CO data to models of diffuse clouds in the ISM, we need estimates of the column density of OH based on our line strength data. OH column densities are calculated from OH 1667 MHz emission lines using the following equation see, e.g. Liszt and Lucas, 1996:

$$N(\mathrm{OH}) = C\frac{T_{ex}}{T_{ex} - T_C}\int T_b(\nu)d\nu, \tag{2.2}$$

which in turn means that values for the continuum temperature in the background of the OH and of the excitation temperature of the 1667 MHz line are both needed as inputs. The coefficient $C = 2.3x10^{14}$ for the 1667 MHz line yields N(OH) in terms of cm^{-2}. However, determining the exact value of the continuum temperature is difficult, as observations have been made at 408 MHz, 1420 MHz, and 2695 MHz, but not at 1667 MHz; moreover, there are different components to the continuum, each of which have different spectral indices, making interpolation complicated. In order to estimate T_C at 1667 MHz, we use the "diffuse component" of the continuum at 1420 MHz as reported by Reich, Reich, and Fürst (1997), and at 2695 MHz as reported by Furst et al. (1990), and we estimate the diffuse component from Haslam et al., 1969 as reported in Taylor et al., 2003. We then made a quadratic interpolation on a logarithmic plot among the continuum temperature at these three frequencies to estimate the diffuse component of the continuum at 1667 MHz. Uncertainty still remains, however, since we do not know how much of the Galactic background portion of the continuum exists in the foreground versus the background of the OH. As such, we choose two possible values representative of the range of plausible T_C values of 4.0 K and 5.0 K for this work. The value T_C = 5.0 K assumes that the continuum is mainly in the background, and T_C = 4.0 K assumes that half of the continuum is in the background, using Xu et al. (2016b) Figure 2 as a rough basis.

The excitation temperature is another unknown quantity, but reasonable estimates are possible. Given that at the coordinate $104.75°, 2.75°$ CO is detected while the corresponding OH signal is very faint, and also that the source component of the continuum contains a small elevated patch in this vicinity which has been catalogued as the probable HII region GB6 B2214+5950 Gregory et al., 1996, it seems plausible that at this coordinate the higher value of T_C is close to the value of T_{ex}. That would put T_{ex} at approximately 1 K above the surrounding value of T_C. Although this is the most likely scenario, since a T_{ex} value closer to T_C would have a significant effect on the resulting column densities, we also try a value of T_{ex} only 0.5 K above the surrounding T_C in our analysis.

2.3 Results

Here we present the main results of this survey, beginning with a scatter plot of OH and CO profile integrals to demonstrate the presence of extended OH emission outside of CO-bright clouds in Fig. 2.3. In addition, we display a 9 × 9 color-coded *heatmap* based on profile integral strengths, which shows spatially the ubiquitous OH emission in the Perseus Arm in contrast to the relatively compact CO emission in Fig. 2.4. Each square in the heatmap represents a GBT beam which, at the assumed distance of the Perseus Arm, corresponds to roughly 7 pc in spatial extent. In a following subsection we present and discuss theoretical models of diffuse clouds which allow us to explore the physical environments of this gas in Fig. 2.6.

2.3.1 Cloud Model Predictions

We have compared the observed ^{12}CO(1-0) and OH 1667 MHz profile integrals with the predictions of a set of diffuse cloud models. Here, we used the model described by Hollenbach et al., 2012, with the modifications discussed by Neufeld and Wolfire, 2016, to obtain predicted CO profile integrals and OH column densities. These were obtained as a function of the thickness of the cloud – measured in magnitudes of visual extinction, $A_V(\mathrm{tot})$ – and the volume density of H nuclei, n_{H}. Results are shown in Fig. 2.6, where colored contours representing fixed values of n_{H} and black contours representing fixed values of $A_V(\mathrm{tot})$ are plotted in the plane of observable quantities (i.e.

the velocity-integrated brightness temperatures for the OH and CO transitions with the OH converted to column density.) All of the predictions shown here were obtained for an assumed cosmic-ray ionization rate of $2 \times 10^{-16}\,\mathrm{s}^{-1}$ (primary ionizations per H atom) – the mean Galactic value favored by Neufeld and Wolfire, 2017–and an assumed interstellar ultraviolet radiation field equal to that given by Draine, 1978.

The resulting values of gas volume density predicted by the cloud model for three representative values of the factor F = $T_{ex}^{67}/(T_{ex}^{67} - T_C)$ are displayed in Table 2.1. Note that for all three cases of input values of T_C and T_{ex}^{67}, the predicted average volume density is greater for the CO-bright gas than it is for the CO-dark gas. As the CO-dark gas volume density predictions are upper limits, this result is further strengthened.

The diffuse cloud models suggest that the portion of the survey that is OH-bright, CO-dark gas is mainly molecular. According to the model, in the representative case where $A_V(\mathrm{tot}) = 0.3$ mag and $n_H = 166\,\mathrm{cm}^{-3}$, the molecular fraction of the gas is found to be 0.7. We also find that the predicted $A_V(\mathrm{tot})$ is greater than $\sim 0.2, 0.25, 0.3$ mag for F = 5, 6, 11 respectively. This lower limit to $A_V(\mathrm{tot})$ most likely results from the sensitivity of the observations and the required OH line strength to be detected above the noise.

2.4 Discussion

2.4.1 Comparing OH and CO Line Strengths

Fig. 2.3 shows the 81 data points resulting from a profile analysis of the OH and CO features, over the same velocity ranges, in the Perseus Arm.

Table 2.1: H Nuclei Volume Density Results for Molecular Gas in the One Square Degree Survey.

T_C (K)	T_{ex}^{67} (K)	F	CO-Bright Mean Volume Density (cm^{-3})	CO-Dark Mean Volume Density (cm^{-3})
4.0	5.0	5.0	400 ± 70	$< 210 \pm 20$
5.0	6.0	6.0	280 ± 40	$< 200 \pm 20$
5.0	5.5	11	160 ± 15	$< 120 \pm 10$

OH emission appears widespread in this region and, if there is a CO signal detected, it is roughly correlated with the OH signal. It is apparent that a substantially larger region of the ISM contains molecular gas than is indicated by the ^{12}CO line.

It is noteworthy to mention that the area of this survey (densely covering one square degree) and that of Allen, Hogg, and Engelke (2015, sparsely covering four square degrees) are quite different, and yet they both statistically show very similar results: 40% of the pointings in Paper I. showed 3σ CO emission, while all of the pointings showed OH emission. In the present survey, 19% of the analyzed pointings showed CO emission and 86% showed OH emission. Both these results reveal large amounts of ’CO-dark’ molecular gas in the ISM. The present survey is dense, showing structure on the scale of the GBT beam itself is 7 pc at the 3.2 kpc distance to the Perseus Arm in this direction, whereas the survey of Allen, Hogg, and Engelke, 2015 was not restricted to certain features in velocity space and was a sparse, blind OH survey that showed ’CO-Dark’ gas structures on larger scales with large gaps between sight lines.

2.4.2 Dark Gas Morphology on 0.125 Degree Intervals

The structure of dark gas is of interest for many reasons. Indirect observational evidence suggests that the diffuse molecular gas surrounds the ‘CO-bright’, molecular gas. Direct mapping of OH emission is extremely difficult due to sensitivity requirements but also shows observationally consistent results: the OH is extended beyond the CO-bright clouds (Wannier et al., 1993;

Allen et al., 2012; Allen, Hogg, and Engelke, 2015; Xu et al., 2016a). If one assumes that the OH molecule can trace all of the diffuse molecular gas, then the extent of the OH emission can tell us how extended this ’CO-faint’ component of the molecular gas actually is. In this regard, we visually identified three interesting regions of note in Fig. **??**:

- Feature A: A CO-bright region centered on l = 104.7, b = 2.75, on the order of 12x12 pc, surrounded by extended OH emission;
- Feature B: A CO-bright region centered on l = 105.25, b = 2.25. A dimmer and smaller structure than feature A, surrounded by extended OH emission, and;
- Feature C: A CO-dark region around l = 105.25, b = 2.875 which shows no CO emission but significant amounts of OH emission. This latter feature extends beyond feature A and B by at least 10-12 pc.

In the case of Feature C, we note that there is clearly a CO-dark region with corresponding OH emission. Note also that our survey is also not fully sampled, that is: the intervals are beamwidths and not half-beamwidths. Finally, while the structure of the CO-bright regions are compact clouds which appear to be localized in our survey area, the structure of the OH emission is more diffuse and we cannot reliably conclude from our limited survey just how extended the dark gas actually is in relation to the CO-bright regions. Grenier, Casandjian, and Terrier, 2005 have described the ‘dark gas’ as being ‘similar in extent to that of atomic HI; it appears to surround all CO-bright regions and bridges the dense cores to the more extended atomic distribution’.

Our results show that OH emission is morphologically and quantitatively consistent with this description of the dark gas.

2.4.3 The Physical Environment of the Dark Molecular Gas

The physical state of the dark molecular gas is inferred to be diffuse clouds of H_2, without the necessary volume density to collisionally excite the 3mm CO(J=1-0) line. The Planck satellite detected an overabundance of IR emission in the column density ranges corresponding to $A_v < 2$ (Planck Collaboration et al., 2011). Wolfire, Hollenbach, and McKee, 2010 theoretically studied the dark gas phenomenon at the surface of molecular cloud surfaces and concluded that in this density range H_2 self-shields while CO can be photo-dissociated. As noted before, the OH-bright, CO-dark gas maintains a high molecular fraction (~ 0.7) in the models and remains a good candidate tracer of the dark molecular gas. However, for lower column and volume density regimes than studied in this paper, this may not be the case and further study is warranted.

Fig. 2.6 shows the diffuse cloud model predictions for the CO emission line strength and OH column densities, along with our Perseus Arm observations overplotted (see 2.3.1). We observe a density effect that is responsible for the CO-faint gas at the current sensitivities of the observations. In the context of these models, variations in the gas density are the most likely explanation for why some positions with detectable OH emission show CO emission above our detection threshold whereas other such positions do not. A density dependence arises because the CO J = 1 state is subthermally populated over much of the density range of interest, and thus the rate of CO emission per molecule is roughly proportional to the density. The OH lambda-doubling transitions, by contrast, become thermally-populated at much lower densities, owing to their much smaller spontaneous radiative decay rates. Thus, the OH emission rate per molecule is independent of density, and the CO/OH line ratio is an increasing function of density in the regime of relevance. Given the line sensitivities achieved in these observations, this behavior results in OH detections that are unaccompanied by CO detections when the gas density is low.

A simple physical explanation for this effect is that for a given state of a molecule to be sufficiently populated for the given transition, the volume density of the environment of the molecule must roughly reach the critical density for that particular molecular transition, where the stimulated emission equals the spontaneous emission ($n^* = A_{ul}/\gamma_{ul}$, where A is the Einstein A coefficient for spontaneous emission and γ is the collisional de-excitation rate coefficient). This concept is an oversimplification, as it neglects the molecular abundances and column density considerations. However, the theoretical predictions of a modified model (Hollenbach et al., 2012) seem to reinforce the argument that the dark molecular gas can be explained by low volume density environments. While molecular lines in the UV and optical are routinely observed in environments more diffuse than their critical density, this radiation is dominated by spontaneous emission, due to a difference in frequency that factors into the Einstein A coefficient as ν^3: $A_{ul} = \frac{64\pi^4}{3hc^3}\nu_{ul}^3|\mu_{ul}^2|$ where ν is the frequency and μ is the mean electric dipole moment of the transition.

The critical density for the CO line is usually estimated as $\sim 10^3$ (Bolatto, Wolfire, and Leroy, 2013). However, this estimate is likely to be oversimplified; the CO emission is generally aided by radiative trapping which can reduce the critical density to well below the optically-thin approximation, possibly by as much as an order of magnitude, depending on the optical depth see e.g. Shirley, 2015. Conversely, we observe OH even in very low density environments, and as the CO non-detections only provide upper limits the OH-bright gas could be in even lower density environments. The critical density for the OH molecule at 1665 and 1667 MHz is $n^{*} \sim 1cm^{-3}$, significantly lower than the CO molecule[3].

The results presented in Table 2.1 for the mean volume density of the CO-bright and CO-dark gas imply that, for the current level of sensitivity discussed in this paper, molecular gas becomes CO-dark below a volume density of H nuclei of $\sim 100 - 200$ cm^{-3} in the survey region, which corresponds to a gas volume density of $\sim 50 - 100$ cm^{-3} if the gas is primarily molecular hydrogen. The result that molecular gas becomes CO-dark below $\sim 50 - 100$ cm^{-3} is consistent with the fact that the critical density for the ^{12}CO(1-0) line is 1000 times larger than that of OH 18 cm transitions see e.g. Wilson, Rohlfs, and Hüttemeister, 2013, Chap. 16.2.1 and Fig. 16.1. Since the OH emission lines at 1665 MHz and 1667 MHz are observed to be approximately in the LTE ratio of 5:9, collisions are expected to be the dominant source of excitation in this environment (Elitzur and Moshe, 1992). The measured fraction of CO-dark molecular gas will depend on the detection threshold and velocity resolution of the comparison CO data set used (Donate and Magnani, 2017; Li

---

[3] However, it could be higher once stimulated emission and absorption of the cosmic microwave background are included (Wannier et al., 1993; Rugel et al., 2018)

et al., 2018).

2.5 Conclusions

The results presented in this paper demonstrate that a substantial fraction of molecular gas is invisible in ^{12}CO(1-0) emission at the current sensitivity level of the FCRAO survey, and this component of the molecular ISM can be effectively traced by sensitive 18-cm OH observations.

- We presented a dense OH survey in the outer Galaxy with particular attention to the Perseus Arm molecular cloud velocity range ($V_{LSR} \sim -65$ km s^{-1}). We showed that OH emission is widespread, which reaffirms previous observational results (see Allen et al., 2012; Allen et al., 2013; Allen, Hogg, and Engelke, 2015), and can be spatially decoupled from CO emission.
- We presented diffuse cloud models to predict the physical conditions of the molecular clouds studied in this paper. We demonstrated that the data, with reasonable assumptions for T_{ex}^{67} and T_C, prefer theoretical densities that are well below the optically-thin critical density approximation for the ^{12}CO(1-0) line. This offers a simple physical explanation for the simultaneous lack of observed CO emission, and yet the presence of extended OH emission in this region. The reason for this is because in the radio regime of low density molecular gas spectral line emission, stimulated emission is the dominant radiation mechanism (Wilson, Rohlfs, and Hüttemeister, 2013).

- The 18-cm OH lines appear to trace the behavior of the dark molecular gas, the CO-dark component of the molecular ISM that has been revealed from analysis of Planck data (Planck Collaboration et al., 2011), gamma-ray (Grenier, Casandjian, and Terrier, 2005; Ackermann et al., 2009; Ackermann et al., 2011), and [CII] data (Velusamy et al., 2010; Glover and Smith, 2016).

- We demonstrated that the additional application and analysis of OH as a low-density molecular gas tracer can also constrain the volume density of molecular clouds with corresponding CO data, if used in conjunction with theoretical models as presented in Fig. 2.6.

- We presented the spatial distribution of the observed OH and CO emission in a one-square-degree patch of the outer galaxy, demonstrating the extended OH emission on scales of $\sim$ 10's of pc. However, we note that our survey area is still too limited to draw conclusions as to the typical full extent of this emission. Grenier, Casandjian, and Terrier, 2005 pointed out that the dark gas appears to 'bridge' the dense molecular gas and the atomic gas; our OH results are consistent with this observation. A wide-field, sensitive OH survey could reveal such a connection in the future.

We also showed how CO and OH data, examined jointly with simulations of the diffuse ISM, can reveal the physical conditions of the dark gas. The large-scale distribution of 18-cm OH emission in the galaxy could shed light on the features of the galactic molecular ISM not revealed by conventional CO mapping observations. Future observations by the 500m FAST telescope (Li and Pan, 2016), and the SKA (Dickey et al., 2013) may help to reveal a portion of this dark molecular ISM content through OH absorption studies; however, the low excitation temperature of the 18-cm OH lines (Engelke and Allen, 2018) remains an impediment to the straightforward interpretation of OH observations in the inner Galaxy in the presence of substantial ambient nonthermal continuum emission. An all-sky survey for OH emission in the outer Galaxy would not be hindered by the much weaker continuum of the galactic background there; however, an effective OH emission survey may be presently out of reach of current instruments owing to the long integration times required to obtain the necessary sensitivity. Nevertheless, such a survey could be critical for an understanding the true extent of diffuse molecular gas in the outer Galaxy.

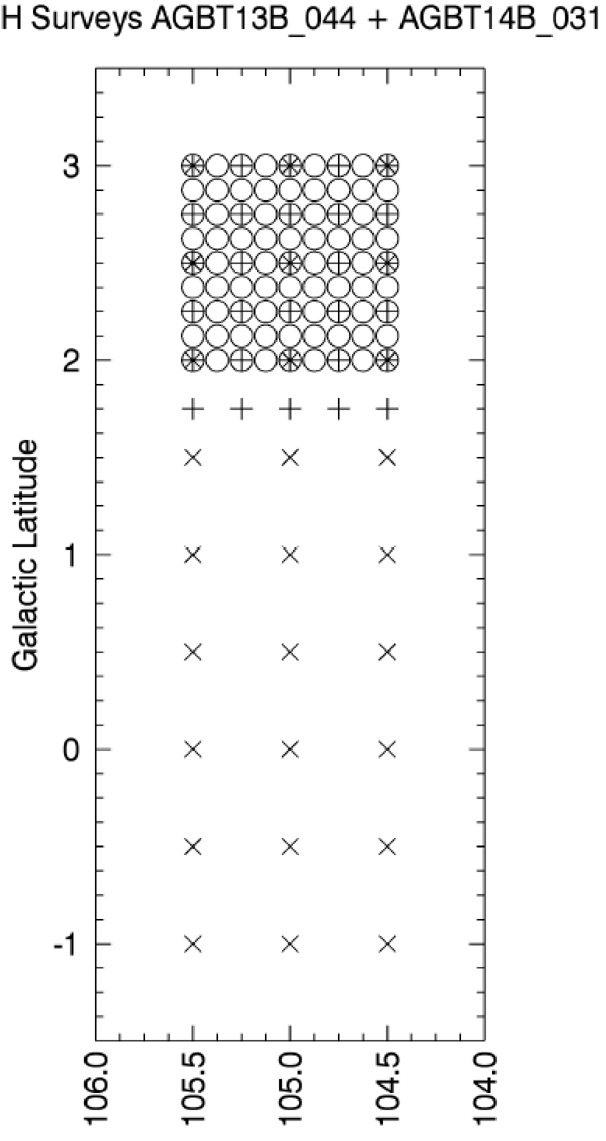

Figure 2.1: The blind survey areas discussed in this work. The “X” markers indicate the original 3x9 ‘sparse’ survey carried out with the GBT ACS spectrometer in program AGBT13B_044 as reported in Paper 1. The set of 9 “X” sightlines in the range of +2° to +3° were later re-observed using the newer VEGAS backend for consistency with the remaining sightlines. The "+" markers indicate the next 5x6 survey carried out in program AGBT14B_031. As unexpected but significant L band GBT observing time became available, we changed the observing goal to sample an entire square degree. The "O" markers indicate the final "One-Square-Degree" 9x9 dense 81-point grid, also carried out under AGBT14B_031. These data are the subject of this paper.

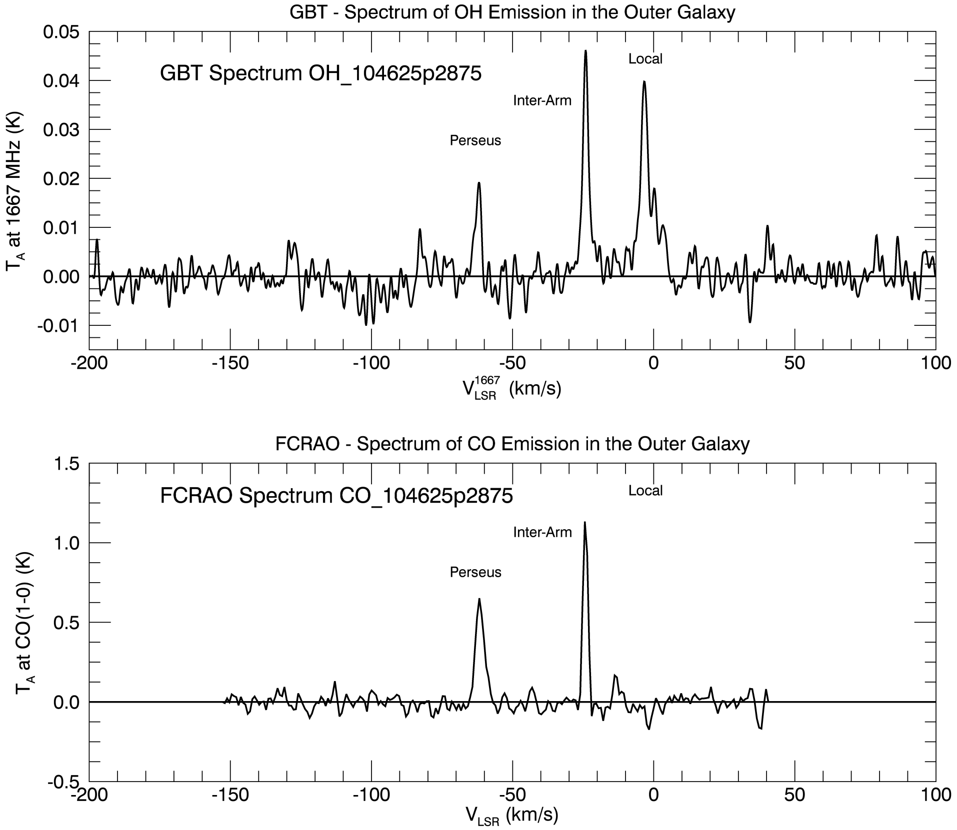

Figure 2.2: Above: Example of a 1667 MHz OH spectrum from the One Square Degree survey. This spectrum was taken at $l = 104.625^\circ, b = +2.875^\circ$ with 2 hr of exposure time on the GBT. We consider any feature detected between -75 and -50 km s^{-1} to be associated with the Perseus Arm. In this spectrum, the OH feature associated with Perseus Arm is located near -65 km s^{-1}. Smaller OH features, possibly spurious, can be observed sometimes at -80 km s^{-1} and at -120 km s^{-1}, corresponding to the Outer Arm and Outer Scutum-Crux Arm respectively. The RMS on this spectrum as calculated by *GTBTIDL* between -190 and -130 is 2.3 mK with a velocity resolution of 1 km s^{-1}. Below: The corresponding example FCRAO CO spectrum in the same direction. Profile integrals are calculated over the same velocity range in both the CO and OH spectrum in the vicinity of the Perseus Arm. While this example does not demonstrate the CO-dark gas at the Perseus Arm velocity, it clearly does at local velocities. However, as shown in Fig. **??**, a large portion of this survey is CO-dark at the velocity range of the Perseus Arm. The velocity resolution of the CO spectra is 0.8 km s^{-1}, and the rms ranges between 60 mK to 100 mK.

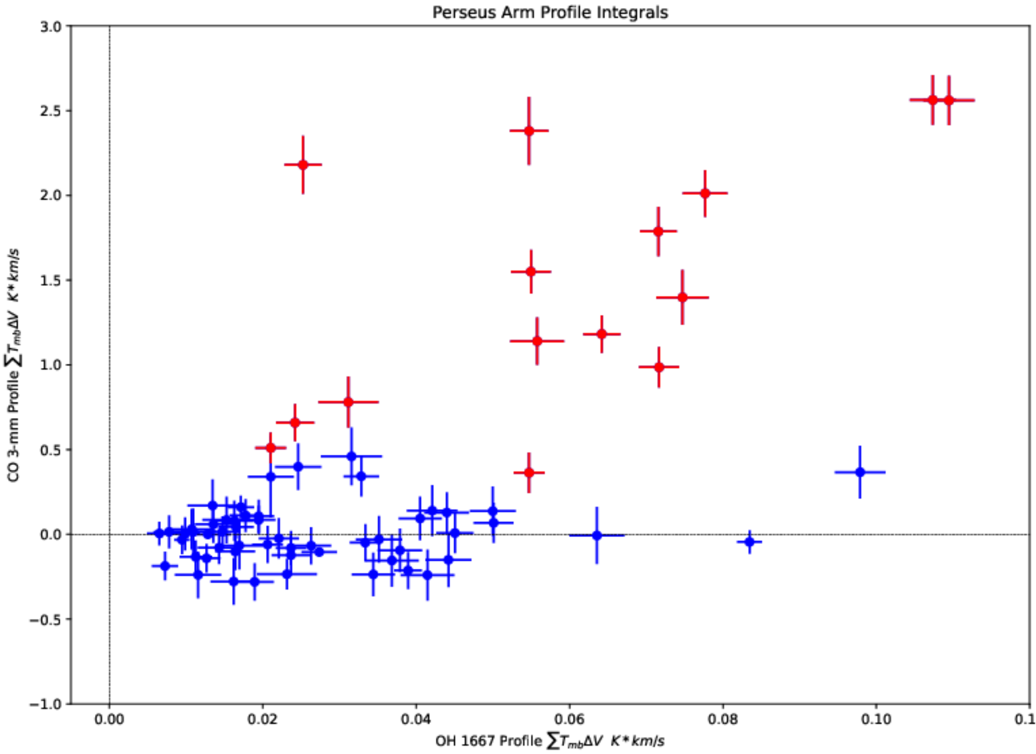

Figure 2.3: The OH 1667 MHz emission line strength and the ^{12}CO(1-0) line strength integrated over the same velocity range near $V_{LSR} \sim -65$ km s^{-1}, corresponding the Perseus Arm. The pointings with detectable (above 3 σ) CO and OH are marked in red. Pointings only with detectable OH are marked in blue. There are 9 pointings with no detections in either OH or CO that are not shown on the plot. We note that there are no pointings that have a CO detections and an OH non-detection.

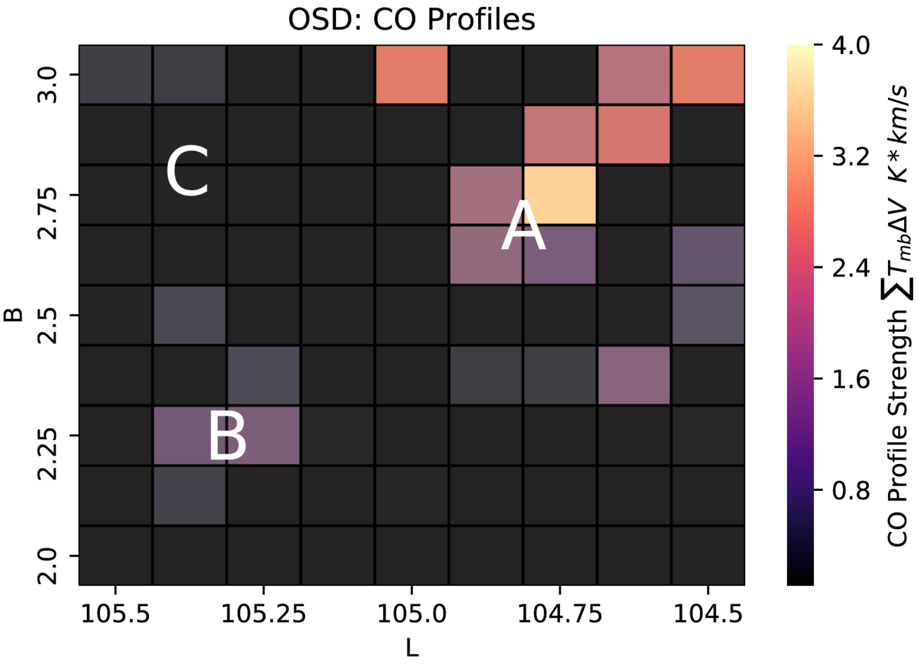

Figure 2.4: The profile integral strengths for the CO line in the Perseus Arm velocity range ($V_{LSR} \sim -65$ km s^{-1}). The squares in these "heatmaps" are 7 pc on a side assuming they are at the distance of the Perseus Arm ($\sim$ 3.2 kpc). Extended OH emission is detected outside and surrounding the standard 'CO-bright' molecular gas, to distances on the order of 10-20 pc. The detections displayed here are in excess of $3\sigma_{rms}$ for both the CO and OH data; locations that are below that detection threshold are set to zero. The letters correspond to interesting features that we highlight, by eye, in Section 4.2.

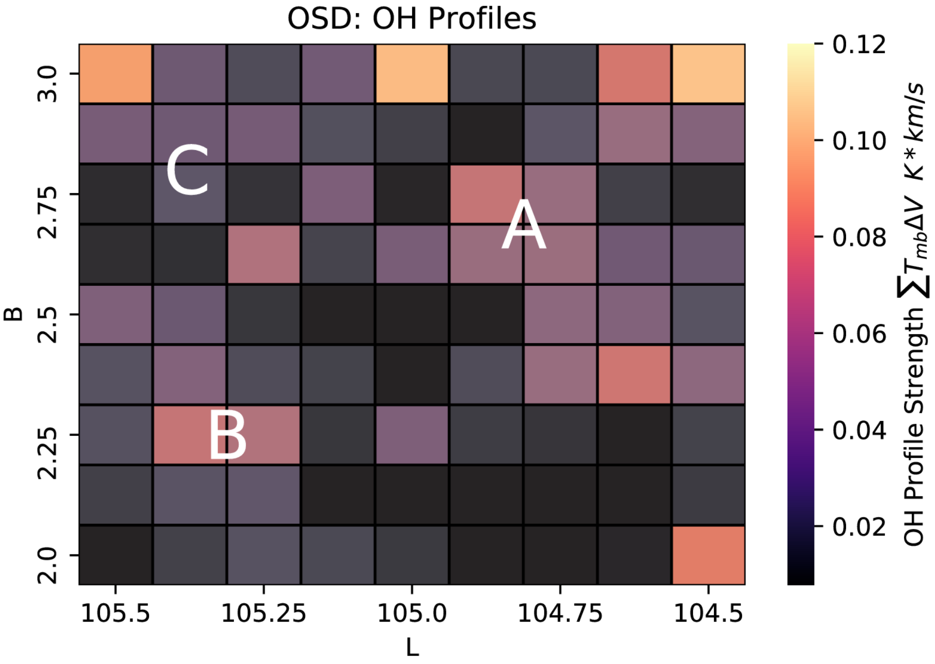

Figure 2.5: The same figure as 2.4 but showing the OH profile integral strengths.

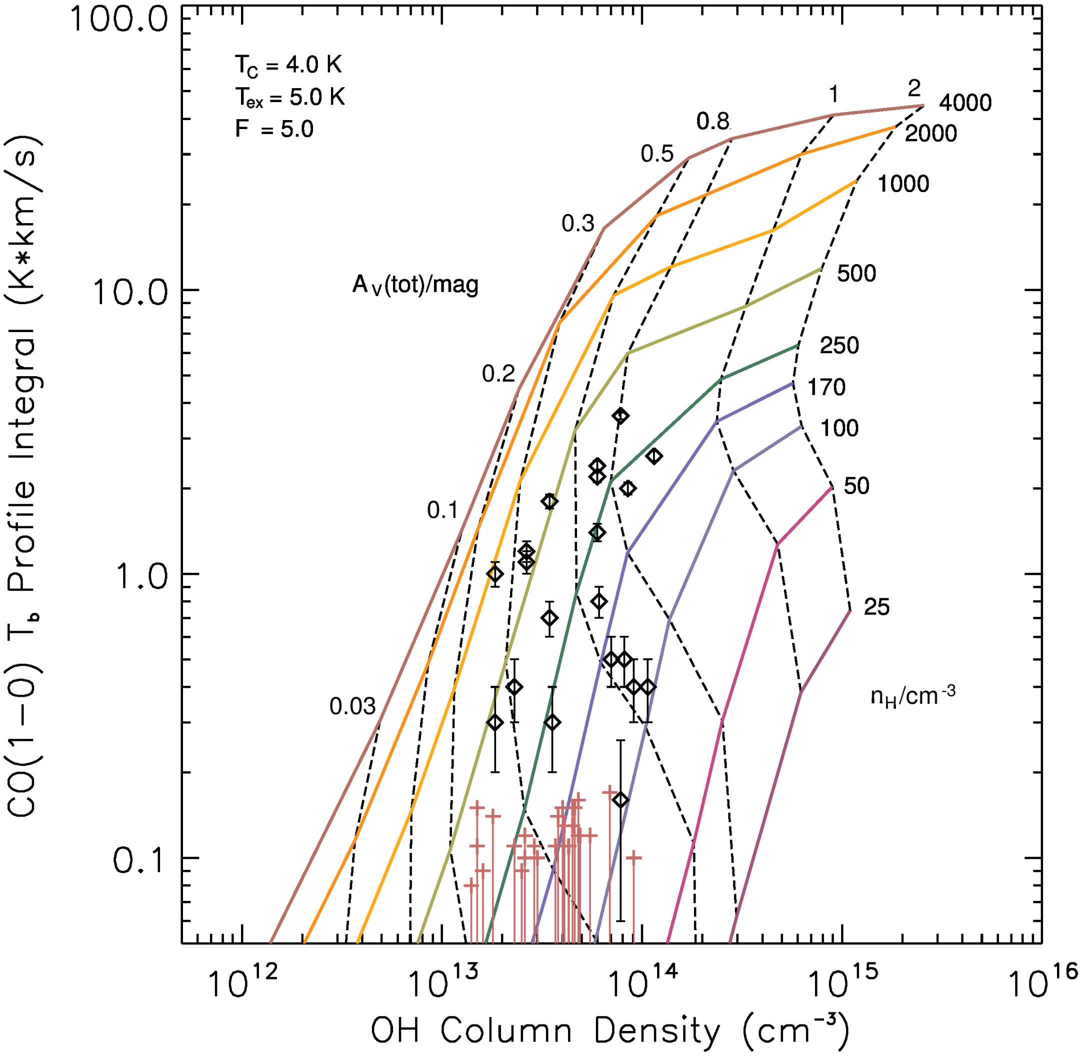

Figure 2.6: The predicted OH column densities and brightness temperatures of the CO(1-0) line as a function of the thickness of the cloud and the volume density of H nuclei ($n_H = n_{HI} + 2\ n_{H_2}$). The colored contours indicate volume density of H nuclei, and the black dashed curves indicate thickness of the cloud in terms of visual extinction. OH Column densities calculated for each of our OH observations and the FCRAO Outer Galaxy CO data are plotted on the model curves. The data indicate that this region of the Perseus Arm exhibits low volume and low column densities and that the volume densities are typically lower for CO-dark gas than for CO-bright gas. The model was run with three sets of input values of T_C and T_{ex}^{67}, and the factor F = $T_{ex}^{67}/(T_{ex}^{67} - T_C)$ representative of the plausible value range for this region. Error bars from the noise level on the OH observations are not shown but would be comparable in size to the size of the data markings.

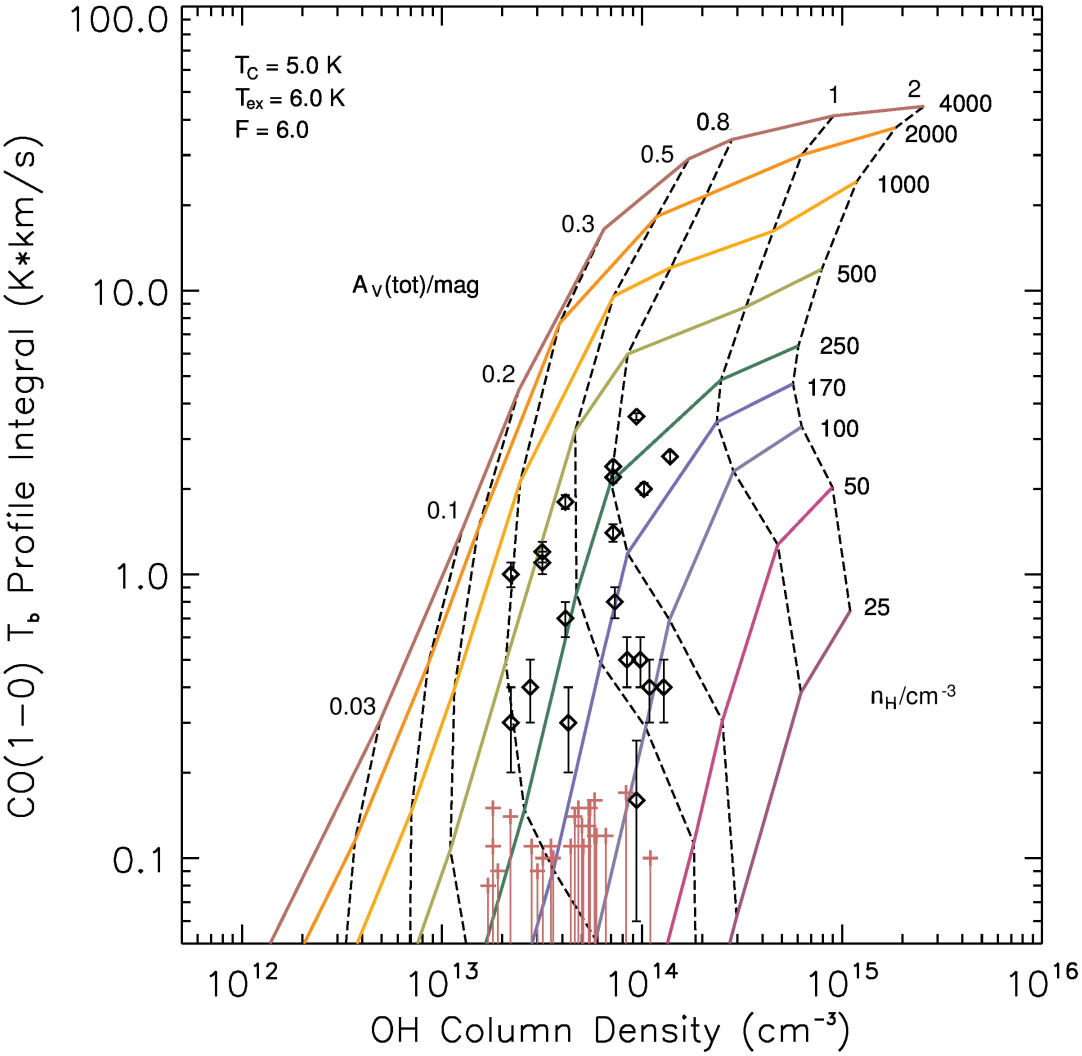

Figure 2.7: Same as Fig. 2.6 but with different input values.

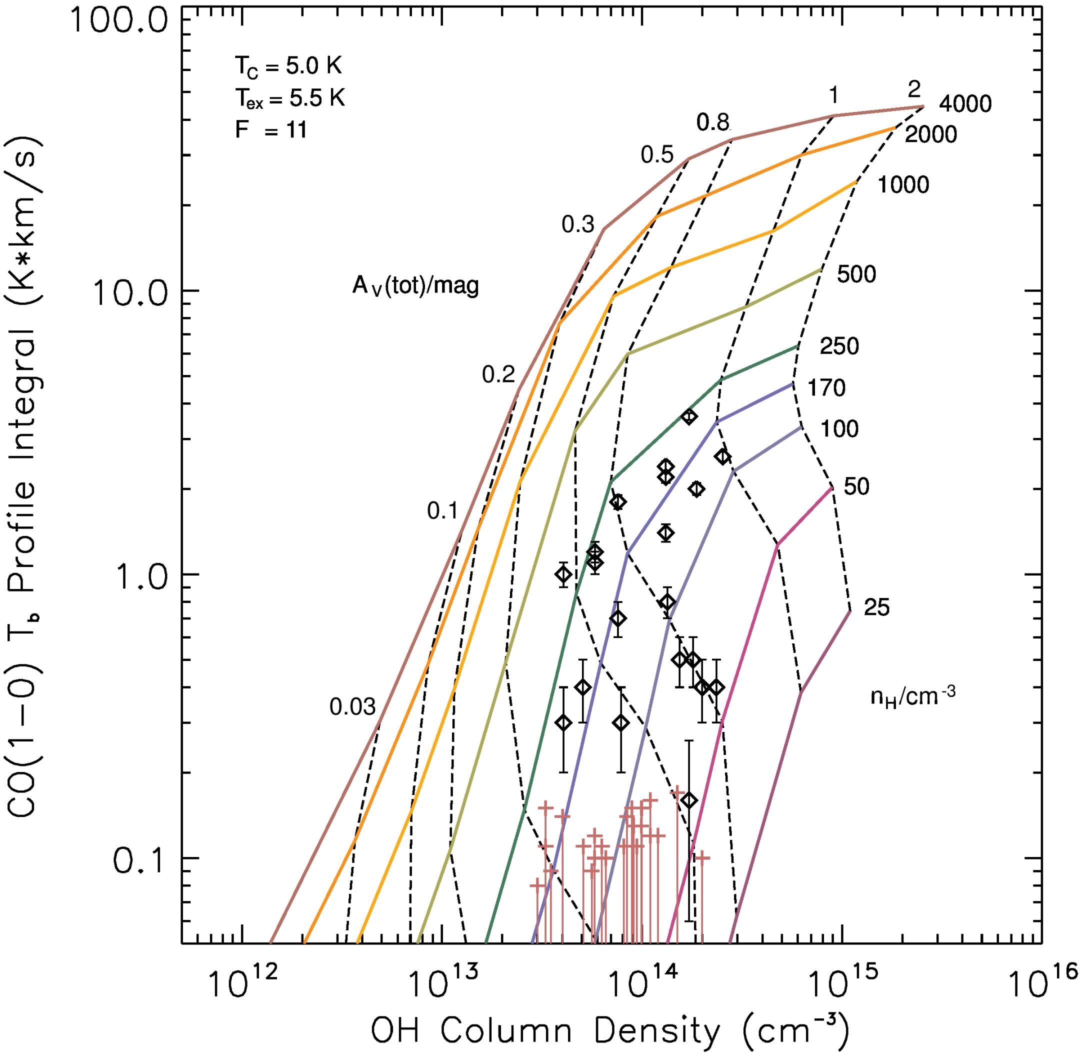

Figure 2.8: Same as Fig. 2.6 but with different input values.

References

Ackermann, M. et al. (2009). *ApJ* 710, pp. 133–149.

Ackermann, M. et al. (2011). *A&A* 538.

Allen, R. J., D. E. Hogg, and P. D. Engelke (2015). *AJ* 149.4, p. 14.

Allen, R. J. et al. (2012). *AJ* 143.4, p. 8.

Allen, R. J. et al. (2013). *AJ* 145.3, p. 85.

Bolatto, A. D., M. Wolfire, and A. K. Leroy (2013). *ARAA* 51, pp. 207–268.

Choi, Y. K. et al. (2014). *ApJ* 790.2, p. 16.

Dame, T. M., D. Hartmann, and P. Thaddeus (2001). *ApJ* 547.2, pp. 792–813.

Dawson, J. R. et al. (2014). *MNRAS* 439.2.

Dickey, J. M. et al. (2013). *PASA* 30, e003.

Donate, E. and L. Magnani (2017). *MNRAS* 472.3, pp. 3169–3176.

Draine, B. T. (1978). *ApJS* 36, p. 595.

Elitzur, M. and Moshe (1992). Vol. 170. Astrophysics and Space Science Library. Dordrecht: Springer Netherlands.

Engelke, P. D. and R. J. Allen (2018). *ApJ* 858.

Foster, T. and B. Cooper (2010). *ASPC* 438, p. 15.

Furst, E. et al. (1990). *A&AS* 85, pp. 691–803.

Garwood, R. W. et al. (2006). *ASPC* 351, p. 512.

Glover, S. C. O. and R. J. Smith (2016). *MNRAS* 462, pp. 3011–3025.

Gregory, P. C. et al. (1996). *ApJS* 103, p. 427.

Grenier, I. A., J.-M. Casandjian, and R. Terrier (2005). *Sci* 307.5713, pp. 1292–1295.

Haslam, C. G. T. et al. (1969). *A&AS* 47, p. 1.

Heyer, M. H. et al. (1998). *ApJS* 115.2, pp. 241–258.

Higgs, L. A. and K. F. Tapping (2000). *ApJ* 120.5, pp. 2471–2487.

Higgs, L. A. et al. (2005). *ApJ* 129.6, pp. 2750–2764.

Hollenbach, D. et al. (2012). *ApJ* 754.2, p. 22.

Li, D. and Z. Pan (2016). *RaSc* 51, pp. 1060–1064.

Li, D. et al. (2015). *PKAS* 30.2.

Li, D. et al. (2018). *ApJS* 235.1, p. 1.

Liszt, H and R Lucas (1996). *A&A* 314, pp. 917–926.

Liszt, H., J. Pety, and R. Lucas (2010). *A&A* 518, p. 45.

Neufeld, D. A. and M. G. Wolfire (2016). *ApJ* 826.2, p. 12.

Neufeld, D. A. and M. G. Wolfire (2017). *ApJ* 845.2, p. 15.

Nguyen, H. et al. (2018). *ApJ* 862.

Papadopoulos, P. P., W. Thi, and S. Viti (2002). *ApJ* 579.1, pp. 270–274.

Pineda, J. L. et al. (2013). *A&A* 554.

Planck Collaboration et al. (2011). *A&A* 536, p. 16.

Prestage, R. M. et al. (2015). *2015 USNC-URSI Radio Science Meeting (Joint with AP-S Symposium)*. IEEE, pp. 294–294.

Reich, P., W. Reich, and E. Fürst (1997). *A&AS* 126.3, pp. 413–435.

Reid, M. J. et al. (2009). *ApJ* 700, pp. 137–148.

Reid, M. J. et al. (2014). *ApJ* 783.

Reid, M. J. et al. (2016). *ApJ* 823.

Rugel, M. R. et al. (2018). *A&A*.

Shirley, Y. L. (2015). *PASP* 127, p. 299.

Taylor, A. R. et al. (2003). *AJ* 125.6, pp. 3145–3164.

Velusamy, T. et al. (2010). *A&A* 521.

Wannier, P. G. et al. (1993). *ApJ* 407, p. 163.

Weselak, T. et al. (2010). *MNRAS* 402.3, pp. 1991–1994.

Wiesemeyer, H. et al. (2016). *A&A* 585, p. 18.

Wilson, T. L., K. Rohlfs, and S. Hüttemeister (2013). Astronomy and Astrophysics Library. Berlin, Heidelberg: Springer.

Wolfire, M. G., D. Hollenbach, and C. F. McKee (2010). *ApJ* 716.2.

Xu, D. et al. (2016a). *ApJ* 819.1, p. 22.

Xu, Y. et al. (2016b). *SciA* 2.e1600878.

Yuan, L. and C. Wallace (1973). *ApJ* 185, p. 453.

Chapter 3

Observational Evidence for a Thick Disk of Dark Molecular Gas in the Outer Galaxy

3.1 Introduction

Molecular Hydrogen (H_2) is the most abundant molecule in the Universe (Draine, 2011). It is important for cooling of the interstellar medium and thus regulates star-formation in galaxies (Glover and Abel, 2008). It is a catalyst for interstellar chemistry. H_2 can be observed using the higher J rotational states in warm molecular gas (Goldsmith et al., 2010), but these require energies usually not available in cold molecular gas, where the bulk of the H_2 lies. This means that despite the importance of H_2 to most areas of astrophysics, it remains difficult to study.

The carbon monoxide (CO) molecule has been used historically to trace the overall distribution of molecular gas in our Galaxy and other galaxies (Bolatto, Wolfire, and Leroy, 2013), due to its substantial relative brightness and abundance. Surveys for the lowest rotational transition of ^{12}CO (J=1-0) at 2.6 mm have made invaluable contributions to our knowledge of the overall distribution, morphology and mass content of molecular gas (Heyer and Dame, 2015).

There remain difficulties in using CO as a tracer for the total H_2 content. The CO line is commonly optically thick, and thus an uncertain and indirect conversion factor, X(CO), is used to convert between a CO line intensity to a H_2 column density. Secondly, a growing body of observational research using indirect total gas tracers (Dust, γ-ray) have shown that there exists a significant portion of H_2 in diffuse regions that are not observed in CO surveys (Blitz, Bazell, and Desert, 1990; Grenier, Casandjian, and Terrier, 2005; Ackermann et al., 2010; Planck Collaboration et al., 2011). Wolfire, Hollenbach, and McKee, 2010 coined the term 'dark molecular gas' to describe the gas not observed by CO, and theorized that up to 30% of H_2 can be missed by CO in the surface layers of molecular clouds.

The physical conditions of the dark gas have been mysterious for much of the past decade, but recent research has shown that the missing portion of gas is not predominately explained by optically thick HI (Murray et al., 2018), which was a promising possible avenue for explaining the dark gas (Fukui et al., 2015). The indirect tracers of gas content such as dust emission and γ-rays are suggestive that the content is in fact molecular gas not traced by CO, but only a molecular tracer could provide such confirmation.

Additionally, these tracers cannot provide radial velocity measurements and hence we lack structure information about the distribution of the dark gas in the plane of the Galaxy. Using a molecule, and particularly for chemical reasons, an abundant hydride (Neufeld and Wolfire, 2016) such as CH (Weselak et al., 2010; Xu and Li, 2016; Jacob et al., 2019; Jacob et al., 2020) or OH (Weinreb et al., 1963; Weinreb et al., 1965; Heiles, 1968; Dickey, Crovisier, and Kazes, 1981; Wannier et al., 1993; Allen et al., 2012; Dawson et al., 2014; Allen, Hogg, and Engelke, 2015; Xu et al., 2016; Engelke and Allen, 2018; Nguyen et al., 2018; Rugel et al., 2018; Engelke and Allen, 2019; Busch et al., 2019) can provide both the unambiguous conclusion that the dark gas is indeed diffuse molecular gas, and the radial velocity information from a spectral line to describe the Galactic distribution of the gas by utilizing the velocity field of the Galaxy (Brand and Blitz, 1993) Studies of the large-scale distribution of gas have been completed mainly using HI (Kalberla et al., 2005; Peek et al., 2011; Winkel et al., 2015) or CO (Heithausen et al., 1993; Heyer et al., 1998; Dame, Hartmann, and Thaddeus, 2001; Heyer and Dame, 2015), and thus the diffuse (or “dark“) molecular gas, and its mass content and Galactic structure, are inherently excluded by these studies (Blitz, Bazell, and Desert, 1990; Goldsmith et al., 2010; Li et al., 2015; Xu et al., 2016; Li et al., 2018).

The situation also has been uncertain in the outer Galaxy, where an analysis of the diffuse Galactic γ-ray distribution from the *Fermi* LAT satellite has suggested that “vast amounts of missing gas in the outer Galaxy are also possible” (Ackermann et al., 2010). This is called the ‘CR (cosmic ray) gradient problem‘, as the observed decline of CR emissivity is inconsistent with CR propagation models. The presence of a warm ($T \sim$ 100-200 K), extremely diffuse ($n \sim$ 5-20 cm^{-3}) phase of molecular gas at large galactic radius was suggested by Papadopoulos, Thi, and Viti (2002) as an explanation for several observational facts.

These findings led us to the conclusion that an additional large-scale molecular gas tracer is needed besides CO, one that could provide an independent estimate of molecular gas content without being subject to the same set of properties and deficiencies as signals from the CO molecule. Desirable features of such a reliable, alternative molecular tracer would include being optically thin, and containing low critical densities for excitation, so as to better detect lower density, more diffuse molecular gas not traced by CO. Such a tracer would provide information on column density, structure, and kinematics, as well as possibly other physical properties of the gas (Busch et al., 2019; Engelke, Allen, and Busch, 2020; Petzler, Dawson, and Wardle, 2020).

The OH molecule, first observed in radio by Weinreb et al., 1963, is one promising alternative molecular tracer. It produces four optically thin spectral lines centered near 18 cm, with critical densities three orders of magnitude below those of the CO(1-0) transition. As such, OH 18 cm emission lines provide a tracer for molecular gas including diffuse, low density regions, and can yield direct calculation of column densities using equations of radiative transfer.

Since 2012, we have demonstrated in a series of papers Allen et al., 2012; Allen et al., 2013; Allen, Hogg, and Engelke, 2015; Busch et al., 2019 that OH successfully functions as an alternate tracer for molecular gas in observations towards a quiescent region of the Outer Galaxy; further observations in the vicinity of the W5 star-forming region extend the use of OH as an alternate tracer to star-forming regions and further develop the techniques of the field Engelke and Allen, 2018; Engelke and Allen, 2019; Engelke, Allen, and Busch, 2020. These projects confirmed the viability of OH as a tracer for molecular gas and studied the structure, column density, volume density, and kinematics of molecular gas in these regions.

We proposed another project in 2014 for the Robert C. Byrd Green Bank Telescope (GBT), aimed specifically at the Perseus Arm towards the Outer Galaxy, with the intention of analyzing several outstanding questions in the field of Galactic structure from the standpoint of molecular gas as traced by OH. During the course of this observing run, an observation at $l = 108.0^\circ$, $b = 3.0^\circ$ performed by RJA in September 2015 and reduced and analyzed by PDE, showed evidence of a broad, low bump-like feature between the narrower, taller features associated with the Perseus Arm and other clumps of molecular gas, and most notably visible near ~ -95 km/s. The feature did not go away when baseline fitting procedures were performed, and at first we contemplated the possibility that the feature was an observation of the Outer Arm. However, the feature was not amenable to Gaussian fits, and comparisons to individual peaks in the HI spectrum at that coordinate, which typically contain corresponding features, did not match. The initial conclusions were that the spectral feature was not Gaussian in shape, and did not correspond to any specific HI peaks, or that there was a source of error in the analysis. More observations were planned and carried out on the coordinate to improve the signal-to-noise on the detection during the fall of 2015 as well as observations at adjacent coordinates to see if the feature appeared in them or not. The result was an unambiguous broad feature between the spectral peaks, which continued to evade subtraction by baseline fitting procedures. At this point we hypothesized that the feature could be a baseline artifact resulting from reflections in the structure of the GBT.

Further work was carried out beginning in 2018, when MPB and RJA performed observations with the 20m telescope at the Green Bank Observatory (GBO) [1] at the same coordinates to determine whether the broad spectral feature was an artifact of the GBT or a real astronomical detection, and we developed several redundant methods to analyze the baselines attempting to demonstrate that the feature could be an artifact. Nevertheless, these observations and analyses have bolstered the evidence for a detection of a broad, diffuse OH signal in between the arms of the Galaxy. From here, we performed new observations at several other pointings in the vicinity to map out the extent of this broad Galactic feature in Galactic longitude; the full results of that survey will appear in a follow-up paper.

In this paper, we present the serendipitous discovery of extremely broad, faint OH emission towards the Outer Galaxy, seemingly underlying the narrower ($\Delta V_{LSR} = 10$ km s^{-1}), brighter ($T_{mb} > 5$mK) line emission from discrete molecular clouds in spiral arms. The velocity extent and morphology suggest that the H_2 content traced by the OH is in the form of extremely diffuse molecular gas in the geometry of a thick disk. We compute the profile integrals in HI and OH and transform those to column densities under a number of

---

[1] The Green Bank Observatory is a facility of the National Science Foundation operated under cooperative agreement by Associated Universities, Inc.

assumptions. We then compute the abundance ratio OH/HI, and, using dust reddening as a calibration for the total column density of gas in this direction, we calculate the abundance ratio of OH/H_2. Under several assumptions, we also calculate preliminary mass estimates.

3.2 Observations and Data

In this study, we present observations of the OH molecule at the main line transitions of 1667 and 1665 MHz using two telescopes, the 100m Green Bank Telescope and the 20m Telescope, at the GBO. We utilize the "SFD" (Schlegel, Finkbeiner, Davis) dust map (Schlegel, Finkbeiner, and Davis, 1997; Schlafly and Finkbeiner, 2010) through a query from the Python package *dustmaps* (M. Green, 2018).

3.2.1 100m Green Bank Telescope

We have observed the ground state, Λ-doubling OH emission lines at 18 cm with the 100m Robert C. Byrd Green Bank Telescope, located in Green Bank, West Virginia, with multiple observational projects over the past five years in order to probe the characteristics of the OH emission from diffuse molecular gas in the outer Galaxy. The project IDs: AGBT14B_031A, AGBT14B_031B, AGBT15B_004, and AGBT19A_453 were all observed for various OH emission projects in the outer Galaxy, but later were reanalyzed to probe the robustness of the result presented. The first profile showing the broad emission feature was under Project ID AGBT15B_004 at $l = 108^\circ$, $b = 3^\circ$, and was thought to be a 'baseline feature' that was difficult to subtract.

A follow-up Project, AGBT19A_484, was undertaken during the summer of 2019 with the GBT in order to directly observe the source geometry of the extremely broad OH emission as a function of Galactic longitude and latitude for the first time. These observations were completed by using frequency-switching by 2 MHz centered on 1617, 1665, and 1720 MHz (O'Neil, 2002) using the VEGAS spectrometer in the L-band range (Prestage et al., 2015). The observations cover all four ground-state OH emission lines, although the 1612 band is commonly unusable due to radio frequency interference (RFI). The beam size of the GBT at 18 cm is 7.6'.

3.2.2 20m GBO Telescope

After an initial discovery in 2015 in a GBT spectrum towards $l = 108.000^\circ, b = 3.000^\circ$, we hypothesized that the broad signal was a faint baseline artifact caused by multipath reflections in the structure of the GBT itself and endeavored to prove that the OH signal was erroneous. This type of instrumental artifact was discovered during the commissioning of the GBT (Fisher, Norrod, and Balser, 2003), where ripples affect the Y linear polarization more than the X linear polarization due to the geometry of the telescope structure.

To test this hypothesis we observed the same position with the 20m telescope at the GBO, and an additional position separated by a degree on the sky. The 20m telescope has completely different structural reflections from the GBT due to its geometry. The detection of the broad, faint OH emission with two different telescopes eliminated the possibility that the broad OH signal was a systematic inherent in the 100m dish of the GBT.

We observed the extended OH emission with the 20m telescope at the Green Bank Observatory during the summer of 2018. Observing time on the 20m telescope for this project was purchased using funds from the Director's Discretionary funds at Space Telescope Science Institute (STScI). The telescope operated in the L-band (1.3-1.8 GHz) range and provided two spectral windows with one centered on the 1667 and 1665 MHz lines, and the other on the 1720 MHz satellite line. The beam size of the 20m at 18 cm was 45′. While the observations with the GBT used frequency switching On/Off observations, the stability of the 20m receiver allowed for total power observations.

3.2.3 Dust and HI

To trace the total gas column density N_H, we use the all-sky dust reddening map from Schlegel, Finkbeiner, and Davis (1997) and Schlafly and Finkbeiner (2010); the well-known “SFD“ dust map. We integrate the entire sightline towards the outer Galaxy, hence the more updated 3D dust maps from Green et al. (2017) are not an appropriate estimation of the total gas column due to the lack of stellar measurements a few kpc outside the solar circle. Therefore, we opt to use the 2D SFD dust map. This map has an angular resolution of 6′.1, which is comparable to the GBT beam ($\sim$ 7′.8). We query the 2D SFD dustmap for the coordinates $l = 108.000°, b = 3.000°$, which returns a dust reddening value, E(B-V) of 1.86 mag.

We also use HI data to estimate the atomic hydrogen column density N(H). We use the HI profile towards $l = 108.000°, b = 3.000°$ from the Leiden-Argentine-Bonn (LAB) survey Kalberla et al. (2005) and HI4PI database (Ben

Bekhti et al., 2016). Additionally, for an estimate of the optical depth of HI towards this sightline, needed for an accurate estimate of N(H), we use two HI absorption-emission pairs from Strasser et al. (2007), to calculate the median HI optical depth along the entire line of sight.

3.3 Data Reduction

The GBT and 20m OH data were reduced using the *GBTIDL* software (Garwood et al., 2006). The quality of this data is generally very high, and each polarization of each 10 minute scan was reviewed for the presence of radio frequency interference and problems from instrumental effects. In this section, we review the experimental and observational tests of the broad OH emission that heightened our confidence in the result.

3.3.1 Separating the "ON" and "OFF" Spectrum

The observations in *AGBT15B_004* were experimented on in several stages of the frequency switching process in order to test different parts of the intermediate frequency (IF) system to make sure the signal was not introduced by some previously unknown systematic that was unaccounted for. Our observations are completed with in-band frequency switching (see e.g. O'Neil, 2002); the reference measurement of ON-OFF is completed by shifting the central frequency 2 MHz and differencing the spectrum. When we perform in-band frequency switching, the science signal is still present in the "OFF" measurement, and the final reduced signal is compiled by shifting and averaging the "OFF-ON" and "ON-OFF" measurements to decrease the noise in the final

RMS by $\sqrt{2}$. This process is demonstrated in Fig. 3.1.

In each separate ON-OFF and OFF-ON signal, we should expect two signals from the two OH lines, and the so-called "ghosts" of the subtracted signals from the shifted frequency. Whichever phase is "ON" or "OFF" is arbitrary. However, it is important that we check if the broad feature is introduced in one part of the IF by appearing in one of the "phases" and not the other. If it were to appear in "ON" but not "OFF", this would raise the alarm of an unknown systematic. We show in Fig. 3.1 that this is not the case, and the positive and negative signals of the OH emission are clearly visible in both reference spectra. The final product of the frequency switched measurement is shown in the bottom panel of Fig. 3.1, where the "OFF-ON" measurement is shifted and averaged together with the "ON-OFF" measurement.

In this final spectrum, we would expect the two signals as well as four 'ghosts', or negative, subtracted signals. Higher order polynomial fits are required for such wide, frequency-switched measurements, as opposed to the linear baseline fits typically used in position-switched measurements.

3.3.2 Baseline Fitting

We were immediately suspicious that the broad OH signal was an erroneous signal introduced by high-order polynomial baseline fitting. We performed baseline fits for a wide range of polynomial orders to test the robustness of this method. The broad emission feature is detected in spectra with polynomial baseline fits from order 8 - 23. The precision of the measurement of the profile integral from the GBT spectra is then constrained by the

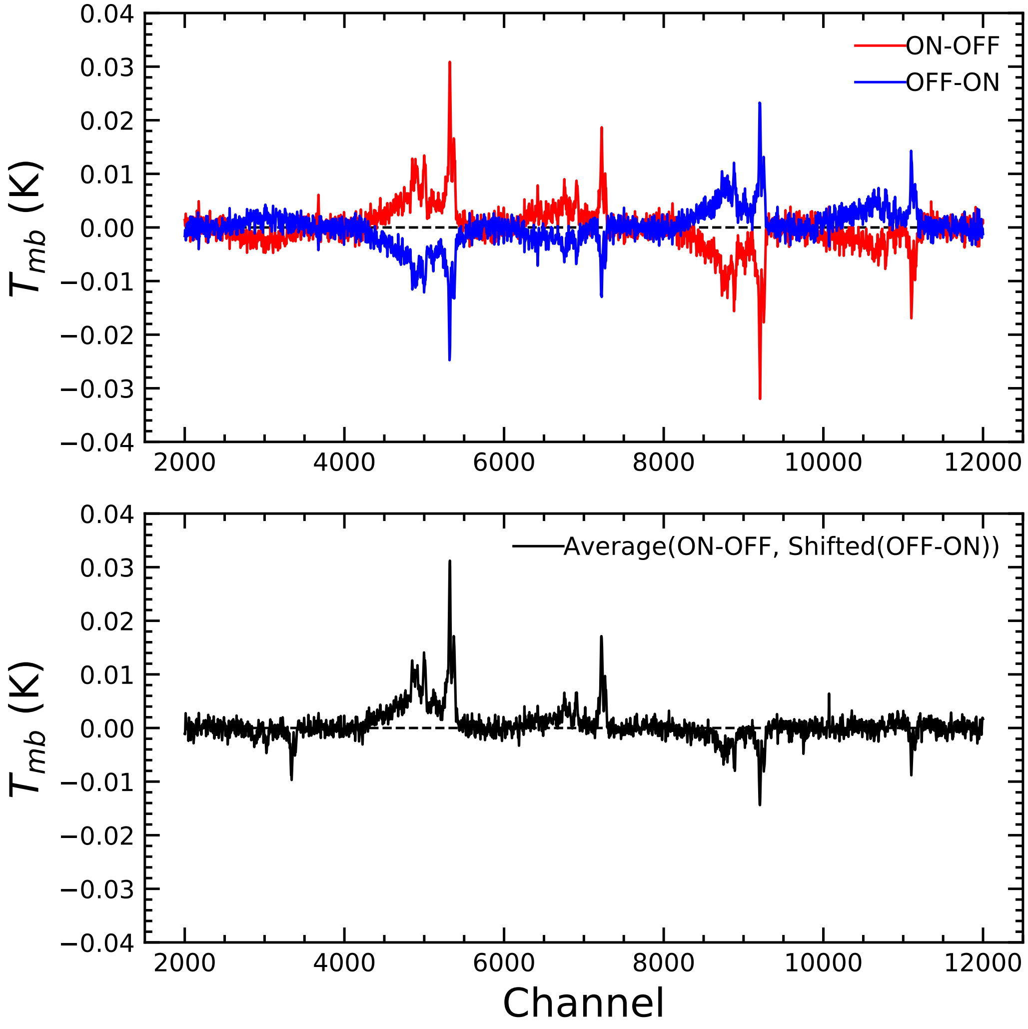

Figure 3.1: The top panel is the "ON-OFF" phase and "OFF-ON" phase plotted separately. The second spectrum is a shift and average of the top two spectra, typical of frequency-switched measurements (O'Neil, 2002).

fitting procedure, which introduces $\sim$ a few percent *systematic* error. To test the robustness of the data pipelines; we created three different data pipelines utilizing different common signal reduction techniques including: Fourier filtering (or bandstop filtering), ridge regression (or L2 Regularization), and the standard general orthogonal polynomial regression used in *GBTIDL*. None of the data pipelines generated different results.

In the case of our GBT observations, since the emission feature is very wide in velocity, and the data are frequency-switched, *linear baselines cannot be removed*. A new data fitting procedure in *GBTIDL* had to be created to deal with such wide profiles. Discontinuous regions of the bandpass that do not have 'ghosts' (negative signal) introduced by the frequency-switching, or signal from the 1667 and 1665 MHz feature, were used ($N_{chans} \sim 6000$) to fit a single high-order polynomial ranging from order 17-23 based on a few different criteria: a) there should be no positive velocity emission due to galactic structure, b) the chosen polynomial fit does not preferentially subtract or under-subtract signal from the 1667 or 1665 emission near local-gas velocities, resulting in a flat baseline, and c) the rms in the highlighted baseline regions is minimized until no further improvement occurs. This procedure produced the most consistent results for the GBT spectrum and flat baselines in all regions where no signal or 'ghost' were expected.

The pipelines were also used on the 20m spectra to produce the broad OH signal with identical results to the GBT spectra. The only noticeable difference in the spectra was the 'flattening' of 'spiral arm' emission from discrete clouds due to beam dilution. The size of the beam at 18 cm for the

GBT is 7.6′, whereas the size of the beam for the 20m is approximately 45′. While the surface brightness is larger in the larger beam, the similar surface brightness of the broad OH emission feature in both spectra indicate that the filling factor of the emitting gas is high, suggesting that the source geometry of the OH emission is extremely diffuse molecular gas that is volume filling.

In addition to replicating the GBT result with the 20m telescope, we also opted to forgo frequency-switching so that the baseline fitting of the 20m spectra would be less complex. Baseline fits of order 2-3 were fit to the total power spectrum and clearly showed the broad OH feature. This result demonstrated that detection of the broad feature does not rely on the higher order (i.e. 17-23) polynomial fits, which conceivably could have introduced spurious artificial signals into the GBT spectrum. In the 100 hour 20m OH spectrum, the RMS noise is ~ 0.3 mK at a velocity resolution of 1 km s^{-1}.

3.3.3 Separating the Linear Polarization

The emission appears to be unpolarized. This is an important check because at cm wavelengths at the GBO observers will sometimes experience weak, transient and usually polarized radio frequency interference (RFI) that is time-dependent. We expect any real thermal OH emission to be non-polarized because it is due to particle motions and collisions in gas that result in dipole oscillations among the four ground-state lines. We checked that we could reproduce the characteristics of the broad and faint OH emission features in 1667 and 1665 MHz in the independent orthogonal linear polarizations (XX and YY). While the YY polarization experiences more baseline noise due to the

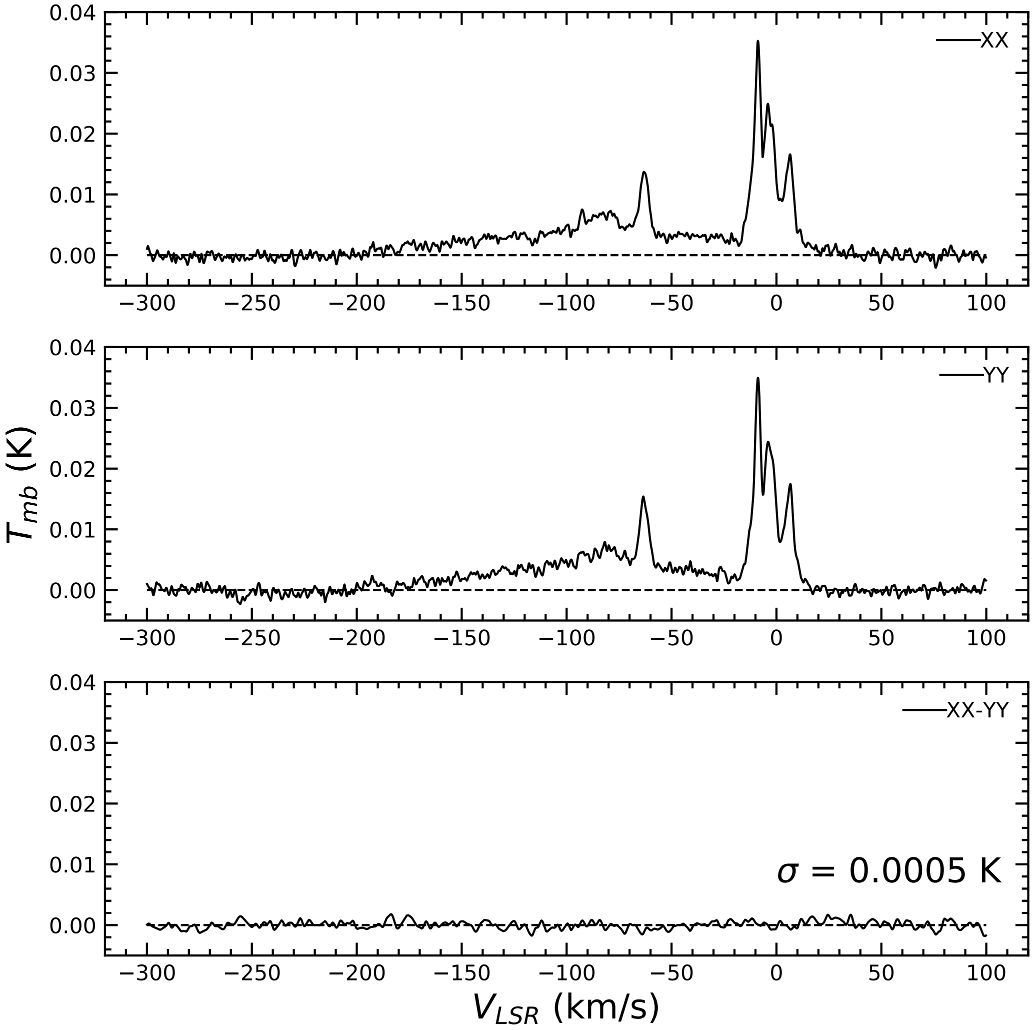

Figure 3.2: The broad OH emission feature as seen in the GBT spectra. Top Panel: A stacked 40 hr spectrum of XX linear polarization. Middle Panel: A stacked 40 hr spectrum of YY linear polarization. Bottom Panel: The resulting residual spectrum from XX-YY. The residual noise is possibly from an additional known spectral ripple in the YY polarization due to the geometry of the GBT itself (Fisher, Norrod, and Balser, 2003).

aforementioned multi-path scattering, we were able to replicate the spectrum and calculate a residual spectrum between the polarization which shows a spectrum with zero emission from the velocity range of the broad OH feature. If the emission were only detected in one polarization, that would indicate that it would be some type of systematic error that we were previously not accounting for.

In this experiment, we stacked five GBT OH spectra towards $l = 108.000^{\circ}$, $b = 3.00^{\circ}$, keeping the linear polarizations separate throughout the reduction. Then, the spectra are smoothed to a velocity resolution of 1 km s^{-1}. The XX and YY spectra are displayed in the top two panels of Fig. 3.10. The residual spectrum of XX-YY is also shown to demonstrate that the two polarizations behave differently at a very small level. The resulting integration time on the spectra in Fig. 3.10 is approximately 40 hours with a RMS noise of T_{RMS} = 300 μK. The systematic from the YY spectrum is at the level of 0.5-0.6 mK, the brightness temperature of the 1667 MHz emission is higher at $T_{mb} = 1 - 3mK$, and the 1665 MHz emission is about half of that, allowing a detection of this feature at high S/N, especially if only using XX data. We rule out the possibility that the emission from the this feature is a polarized systematic baseline ripple in the GBT.

3.4 Results

In this section we will describe the two main spectra presented in this paper, the nature of the OH main lines, and how column densities of HI, OH and H_2 are computed.

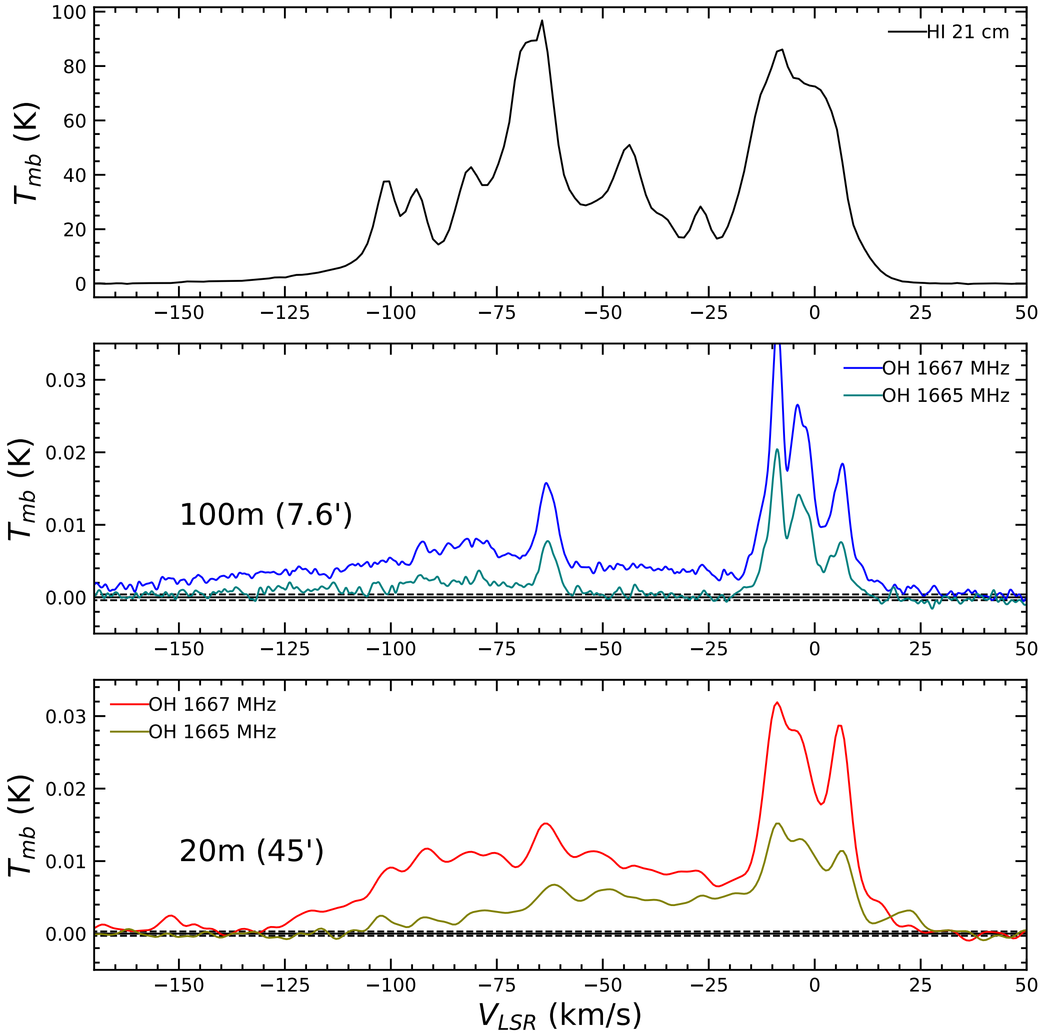

Figure 3.3: The observed broad emission in spectra towards the Outer Galaxy at $l = 108°$, $b = 3°$ comparing the results from the 100m GBT and the 20m telescope at the GBO. The top panel shows the HI emission at 1420 MHz (21 cm) observed with the GBT. The middle panel shows the OH spectra observed at 1667 MHz (blue) and at 1665 MHz (green) using the 100m GBT, while the bottom panel shows the OH spectra observed at 1667 MHz (red) and 1665 MHz (yellow-brown) using the 20m telescope at the GBO. Note that while the telescope resolution varies from 7.6′ at the GBT to 45′ at the 20m telescope, the broad emission is detected with both of these telescopes. The dashed lines are the 3σ statistical detection limit, corresponding to 3 mK for the 100m telescope and 2 mK for the 20m telescope.

3.4.1 GBT Spectra

It became apparent that many sightlines could be stacked from multiple OH projects because of the extended nature of the broad OH emission, which appeared to be beam filling. This allowed for artificially extremely long integration times (up to 300 hours). Depending on how many positions are averaged together, the rms noise in the spectra was between $\sim$ 300-800 μK. The GBT spectra shown in the middle panel of Fig. 3.3 come from an 80 hour, stacked OH spectrum centered at 1666 MHz, which was then re-centered for the 1667 and 1665 MHz lines respectively. The positions used in this spectra are seven ten-hour exposures around the coordinates ($l = 108^\circ$, $b = 3^\circ$). The main beam efficiency of the 100m at L-band is estimated to be η_{mb} = 0.95, which we used to convert antenna temperature to main beam temperature.

3.4.2 20m Spectra

After averaging 100 hrs of observations at two separate positions ($l = 108^\circ$, $b = 3^\circ$ and $l = 109^\circ$, $b = 2.5^\circ$), separated by a degree on the sky, and smoothing to 1 km s^{-1}, the rms noise in the spectrum was $\sim$ 300 μK. We have aligned the local gas emission in the two spectra using a LSR (local standard of rest) velocity correction calculator kindly provided by F. Ghigo[2]. The resulting OH spectrum at 1667 and 1665 MHz are shown in the bottom panel of Fig. 3.3. The main beam efficiency of the 20m is estimated to be η_{mb} = 0.77 (F. Ghigo, private communication), which we used to convert antenna temperature to main beam temperature.

---

[2] https://www.gb.nrao.edu/ fghigo/gbt/setups/radvelcalc.html

3.4.3 1667 and 1665 MHz OH Lines

On a GBT spectrum with 10 hours of integration time, the resulting rms at a velocity resolution of 1 km s^{-1} is close to 1 mK. Typical brightness temperatures per channel are $T_{mb} \sim 1 - 3$mK, and thus the profile integral over the large velocity width ($\Delta v_{LSR} \sim$ 150km s^{-1}) of the emission results in a signal-to-noise (S/N) of approximately 25. The emission also appears clearly in the two main lines of the OH ground state ($\Delta F = 0$) at 1667 and 1665 MHz. The profile integrals of the observed emission regularly appear to be in the 9:5 LTE ratio set by the quantum mechanical transition strengths (Townes and Schawlow, 1955; Turner and Heiles, 1971). This ratio indicates that collisional excitation of OH is the dominant radiation mechanism in the gas, as the energy levels approach the typical Boltzmann distribution as described by an excitation temperature T_{ex}, yet the brightness temperature is not near the actual gas temperature.

3.4.4 Column Density of OH

The expression for the total molecular gas column density is (Mangum and Shirley, 2015):

$$N_{tot} = \frac{3h}{8\pi^3|\mu_{lu}|^2}\frac{Q_{rot}}{g_u}\exp\left(\frac{E_u}{kT_{ex}}\right)[\exp\left(\frac{h\nu}{kT_{ex}}\right) - 1]^{-1}\int \tau_\nu d\nu \tag{3.1}$$

where Q_{rot} is the rotational partition function, the statistical sum over all rotational energy levels in the molecule (for the OH hyperfine, Λ-doubling ground states, this sum is 16), and g_u is the degeneracy of the energy level u.

In the analysis of OH emission line profiles, this equation can be converted to mostly observables. Consider a molecular cloud located in the ISM at a distance S along a line of sight from the Sun towards the outer Galaxy. The beam-averaged column density of OH molecules $\langle N(OH)\rangle$ along the line of sight through the cloud is (Liszt, Pety, and Lucas, 2010):

$$\langle N(\mathrm{OH})\rangle = C_{67}\left[\frac{T_{ex}^{67}}{T_{ex}^{67} - T_c}\right]\int \Delta T_b^{67}(v)dv; \tag{3.2}$$

where $\Delta T_b^{67}(v)$ is the (main beam) brightness temperature of the OH emission profile from the cloud as observed in one of the 18-cm OH transitions (in this example the transition that gives rise to the 1667 MHz line), minus an estimate of the underlying radio continuum brightness at the same radial velocity (the 'baseline'); T_{ex}^{67} is the excitation temperature for the 1667 line; T_c is the brightness of the Galactic continuum emission at 1667 MHz incident on the back surface of the cloud, and the integration over velocity includes all the molecular emission thought to arise in that particular cloud. This equation assumes that the Rayleigh-Jeans approximation applies, that the optical depth of the cloud in the OH line is small, that all the OH molecules are in the ground rotational-vibrational state, and that the 4 ground-state levels are populated according to LTE. Under these conditions, the constant C_ν consists of:

$$C_\nu = \frac{8\pi k \nu_{ul}\Sigma g_i}{hc^2 A_{ul} g_u} \times (\nu_{ul}/c) \tag{3.3}$$

where ν_{ul} is the transition line frequency, A_{ul} is the Einstein A coefficient for that transition, Σg_i is the sum of the statistical weights of the four levels giving rise to the 18cm lines (=16), g_u is the statistical weight of the upper energy level that gives rise to the specific line (e.g. = 5 for the 1667 line), and k, h, and c designate the usual physical constants. This equation has been grouped into two terms; the first is from Goss, 1968, and the second provides the conversion from line widths in Hertz (used by Goss) to the currently more conventional units of doppler velocity. Using the entries for the line frequencies and Einstein A coefficients found in the Splatalogue data base[3] appropriate for the 1667 MHz line, the value of C_{67} is 2.257×10^{14} cm^{-2} for ΔT_b^{67} in Kelvins and velocity in km s^{-1}.

In this analysis, we assume an excitation temperature of 5.1K ± 1K, as the excitation temperature is usually found to be within 1-2K above the continuum temperature (Li et al., 2018; Engelke, Allen, and Busch, 2020), although we stress caution because the real excitation temperature of the gas may be lower, closer to the Galactic background as found in Li et al. (2018). The possible range of excitation temperatures and continuum temperatures alone introduces systematic uncertainty in the resulting N(OH) values, which we explore below. To obtain an estimate of the continuum background brightness temperature, T_c, we estimate the synchrotron contribution from the 408 MHz continuum map of the Canadian Galactic Plane Survey (CGPS, Taylor et al. (2003)) by adopting a temperature spectral index of 2.8 (Reich and Reich, 1988):

$$T_c = 2.7 + T_{c,408}(1667/408)^{-2.8}, \tag{3.4}$$

which results in a T_c of approximately 4K. An approved GBT program

---

[3] http://www.cv.nrao.edu/php/splat/

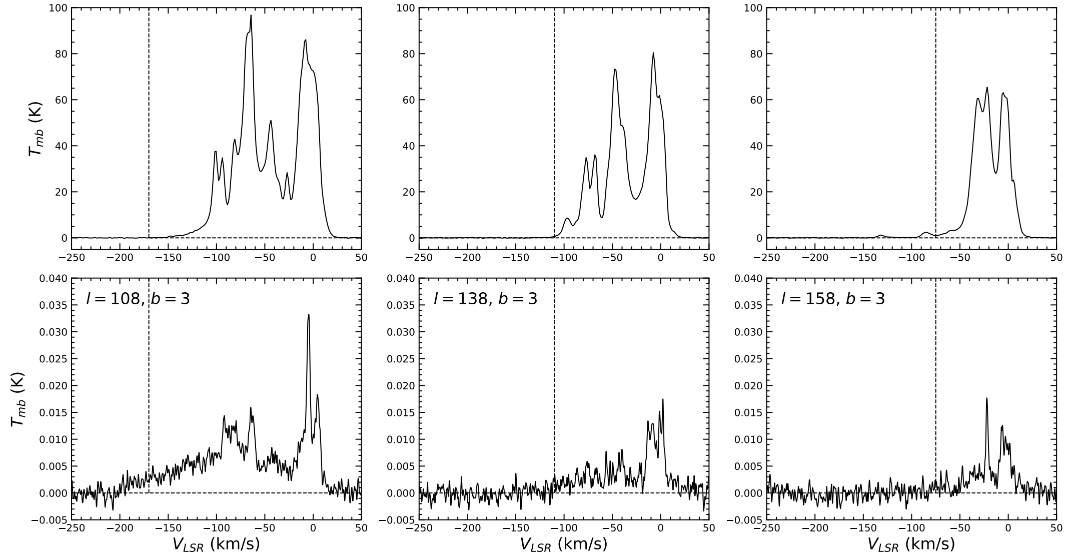

Figure 3.4: Left: The atomic (top) and molecular (bottom) content towards the sightline $l = 108°$, $b = 3°$ as traced by HI and OH with a 7.6′ beam. Middle: The same at $l = 138°$, $b = 3°$. Right: The same at $l = 158°$, $b = 3°$. Notice that because l is approaching 180°, the velocity of the emission begins to crowd towards 0 km s^{-1}due to the geometry of the Galactic velocity field.

for this coming year will attempt to observe this dark disk in absorption and emission pairs, which should unambiguously provide an accurate measurement of T_{ex} in the future. The resulting column density is: $N(\mathrm{OH}) = (7.41 \pm 0.17) \times 10^{14}$ cm^{-2}, which includes statistical error. For a sensitivity calculation on systematic errors, we calculate the possible ranges of OH column densities using 4.1K < T_c < 4.5 K, and 4.6K < T_{ex} < 6.1 K. This range results in: $N(\mathrm{OH}) =$ (1.0 $\pm$ 0.017 statistical $\pm$ 0.4 systematic) $\times 10^{15}$ cm^{-2}. Note that the systematic uncertainty due to the unknown values of T_c and T_{ex} dominate. We remind the reader here that the continuum temperature and excitation conditions are likely *not* constant through the entire outer Galaxy, and thus a more precise treatment in the future will be warranted when more data are available.

3.4.5 Column Density of HI

An accurate measurement of the column density of HI is needed to calculate the presumed amount of H_2 in the sightline from the gas content as traced by dust reddening. We estimate the optical depth of HI, τ, as a constant value across the sightline by examining two absorption-emission pairs from Strasser et al. (2007) that we read from their online data: l = 108.446°, b = 4.0498°; and l = 108.753°, b = 2.5772°. Although τ changes along the line of sight, we take the median value from these sight lines as a constant for the calculations of the column density of HI at $l = 108^\circ$, $b = 3^\circ$ because they are close in proximity and representative of the diffuse ISM in this direction. The median across the line of sight in these two directions results in a τ = 0.103 ± 0.03, which we use as the τ in the following HI column density calculations.

We use Equation 5 in Dickey and Benson (1982) to calculate the column density of HI using the LAB survey HI spectrum at l = 108°, b=3°:

$$\langle N(\mathrm{HI})\rangle = C_0 \int T_{mb}(v) \frac{\tau}{1 - e^{-\tau}} dv \tag{3.5}$$

where $C_0 = 1.82 \times 10^{18}\ \frac{\mathrm{cm}^{-2}}{\mathrm{Kkm\ s}^{-1}}$. This calculation assumes an isothermal medium along the line of sight, with constant HI spin temperatures; which is likely somewhat incorrect because there are different environmental regions along the entire line of sight towards the outer Galaxy. However, because our estimate of the total gas content, N_H is from dust IR emission, and hence does not contain radial velocity information, we cannot reliably decompose the HI and OH spectrum into their different components if the H_2 content is of pertinent interest. The resulting HI column density is $N(\mathrm{H}) = (1 \pm 0.3) \times 10^{22}$ cm^{-2}. The resulting N(OH)/N(H) ratio is $\sim$ a few $\times\ 10^{-7}$.

The HI4PI server[4] returns an HI column of $N(\mathrm{H}) = 9.58 \times 10^{21}$ cm^{-2}. Our column density differs (albeit, within error) because we restrain our column density calculation only to the Milky Way disk (-150 km $\mathrm{s}^{-1} <$ V_{LSR} < 100 km s^{-1}) and correct for τ, whereas the HI4PI N(H) maps calculate their optically-thin column densities along their entire radial velocity range, -600 km $\mathrm{s}^{-1} < V_{LSR} < 600$ km s^{-1}. This may include not only the Milky Way disk material, but also HI gas in the MW halo, intermediate and high velocity gas complexes, and extra-galactic HI objects.

3.4.6 The OH Abundance Ratio

While several estimates of the N(OH)/N($\mathrm{H_2}$) abundance ratio exist for several Galactic environments (Liszt and Lucas, 1996; Nguyen et al., 2018; Rugel et al., 2018; Jacob et al., 2019), it is unclear which value is appropriate to use for this sightline, as most of these estimates were calculated towards discrete clouds with absorption sources, and typically near the solar neighborhood. We estimate our own abundance ratio in this sightline by using dust reddening as a tracer for the total gas content, to see if it is consistent with the latest abundance ratio calculations from the THOR survey (Rugel et al., 2018) and using CH as a calibration tracer (Jacob et al., 2019). We closely followed the prescription of this method as laid out in Nguyen et al. (2018). Reddening is caused by dust grains through the absorption and scattering of

---

[4] https://www.astro.uni-bonn.de/hisurvey/AllSky_gauss/

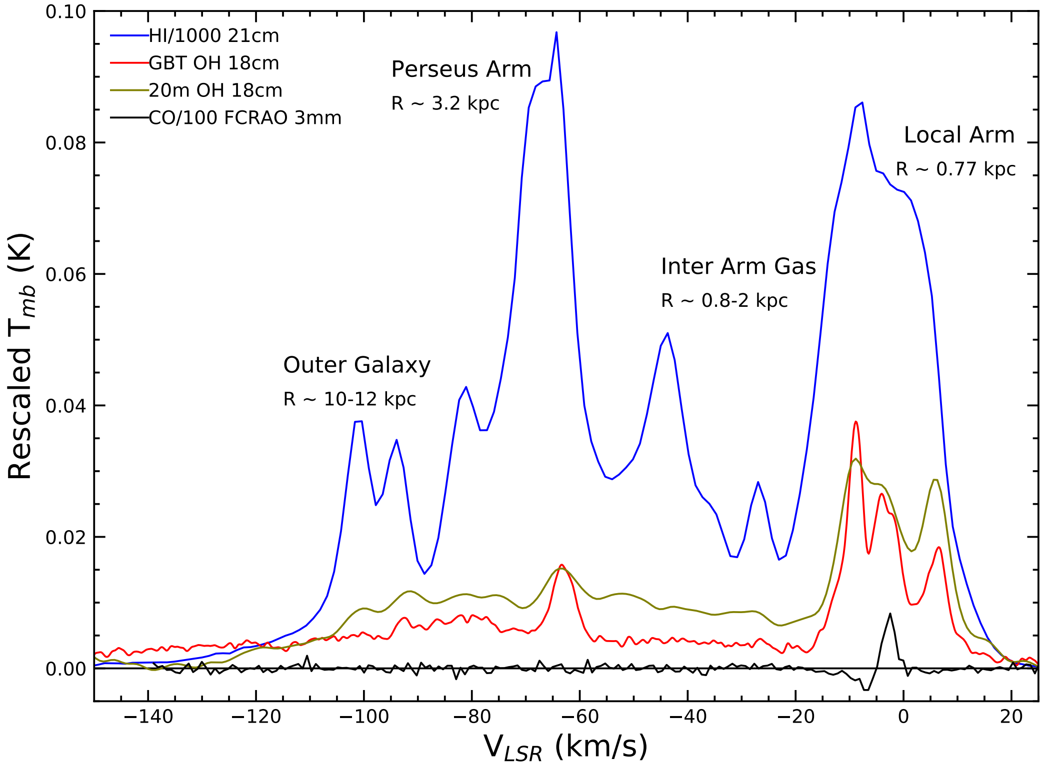

Figure 3.5: The observed 1667 and 1665 MHz OH broad emission toward the outer Galaxy ($l = 108$, $b = 3$), as observed by the 100m GBT and 20m telescope at the GBO. The dashed lines are the 3σ (corresponding to 2mK for the 20m, 3mk for the 100m) statistical detection limit. The HI spectrum is from the LAB survey (Kalberla et al., 2005). The CO spectrum is from the FCRAO spectrum (Heyer et al., 1998), kindly provided by M. Heyer.

light, defined as:

$$E(B-V) = \frac{A_V}{R_V} = 1.086\frac{\kappa}{R_V} r\mu m_H N_H \qquad (3.6)$$

where A_V is the dust extinction, R_V is an empirical coefficient, κ is the emissivity per cross section, r is the dust-to-gas mass ratio, μ is the molecular weight (=2), m_H is the weight of a hydrogen atom and N_H is the total gas content, defined as: $N_H = N(H) + 2N(H_2)$. R_V is typically assumed to be 3.1

(Cardelli, Clayton, and Mathis, 1989). While it has been shown that R_V varies on Galactic scales, it does not vary significantly (Schlafly et al., 2016). The SFD dustmap assumes a value of 3.1, which we use in this paper.

In this analysis we assume that the total gas content is a linear combination of atomic and molecular hydrogen, $N_H = N(\mathrm{H}) + 2N(H_2)$. We subtract the column density of atomic hydrogen and assume that the residual is molecular hydrogen. The uncertainties in this method include the uncertainty in the dust reddening, the uncertainty in the N_H/E(B-V) ratio, and the uncertainty in the optical depth, τ, of the HI.

Using the opacity corrected HI column density from Sect. 3.4.5, we calculate a column density of protons, N_H, of 1×10^{22}, and H_2 of $N(H_2) = 3 \times 10^{20}$ cm^{-2}. Using this to calculate an abundance ratio, N(OH)/N(H_2) = 1.5-4 $\times 10^{-6}$, which is consistent the range of abundance ratios from the literature (Nguyen et al., 2018; Rugel et al., 2018; Jacob et al., 2019). Our calculations and the predictions from theory are also consistent with expectations for diffuse regions, $A_v < 0.1$ mag (Neufeld and Wolfire, 2016).

3.5 Discussion

3.5.1 The large-scale Galactic structure of the OH Emission

In 2019 we undertook a GBT survey in longitude and latitude to probe the structure of the broad OH emission under Project ID AGBT19A_484. It was quickly discovered that the emission experiences the same expected velocity structure of the large-scale HI in the outer Galaxy. That is, the velocity distribution of the emission approaches zero with increasing l, as shown in

Fig. 3.4. This unambiguously implies that the broad OH profile is indeed a large-scale structure in the Galaxy that obeys the geometry of the velocity field (Burton and Lintel Hekkert, 1985). The HI and OH emission morphology appear to behave the same in velocity space, implying a cospatial nature of this phase of molecular gas with atomic gas in the outer galaxy. The HI associated with the Galactic disk is known to extend outward from the center farther than optically observed portions of the Galaxy such as stars, as well as known molecular components detected with CO. As such, this result extends the distance outward in the Galaxy in which molecular gas is found. At the same longitude and latitude, we demonstrate that this gas is by definition *dark*, because it lacks a similar detection in a sensitive CO spectrum (Heyer et al., 1998), see Fig. 3.5.

While the longitude-velocity dependence is suggestive of a large-scale structure, we also checked for structure between $-5^\circ < b < 5^\circ$ towards $l = 105^\circ$ by stacking in latitude the data from AGBT15B_004 in longitude. We were able to detect the broad OH emission to some level in every spectrum. It was apparent, however, that the OH emission is very small (T_{mb} = 1 mK) at high latitudes, $b = -5^\circ$ and $b = 5^\circ$. This suggests that the feature has some scale height of $\sim$ 200 pc. In a future paper we will investigate this further. Additionally, it appears that the gas has a bi-modal distribution around $b = 1^\circ$. This may be because of the Galactic warp in this direction (Yuan and Wallace, 1973), which warps the stellar and gas disk above the Galactic plane.

3.5.2 The Implied Volume Density of the Diffuse Molecular Disk

Owing to Galactic rotation, the distance s along the line of sight and the radial velocity v at that point are approximately linearly related in the outer Galaxy. This suggests that we can estimate the *volume density* n_{OH} at any point s along the line of sight by differentiating equation 3.2 with respect to distance s along the line of sight to obtain:

$$\begin{aligned} n_s(OH) &\approx C_{67}\left[\frac{T_{ex}^{67}}{T_{ex}^{67} - T_c(l \geq L)}\right] d/ds \int \Delta T_b^{67}(v)dv \qquad (3.7) \\ &\approx C_{67}\left[\frac{T_{ex}^{67}}{T_{ex}^{67} - T_c(l \geq L)}\right] \Delta T_b^{67}(v)dv/ds|_{s=S} \qquad (3.8) \end{aligned}$$

where dv/ds is in units of km s^{-1}/cm for the value of C_{67} adopted here. To determine an approximate value for dv/ds appropriate for any given Galactic longitude, we use the values of S for a given value of v returned by the VLBI “Revised Kinematic Distance Calculator“ developed by the “BeSSeL“ collaboration[5]; for additional background information see the review paper by Reid and Honma (2014). This approach allows us to estimate values for $s(v)$ and ds/dv which are less prone to local perturbations in the velocity field of the outer Galaxy. For instance, at $l = 108.0°$, $b = +3.0°$, and e.g. at $v = -80$ km s^{-1}(the approximate radial velocity of the outer arm of the Galaxy at this value of l) we obtain the linear approximation $s = a - bv$ with $a \approx 0$ and $b \approx 0.0875$ kpc/(km s^{-1}) at a distance of ≈ 7.0 kpc from the Sun. As an

---

[5] http://bessel.vlbi-astrometry.org/home

illustration, the volume density at this location is 1.8×10^{-9} OH molecules cm^{-3}per mK of 1667 MHz main-beam brightness temperature, assuming we are far enough in the outskirts of the Galaxy to set $T_c(s \geq S) = 3$K (i.e. slightly above CMB alone), and choosing $T_{ex}^{67} = 4.1$K (a reasonable value between the ones found in Engelke and Allen (2018) and Li et al. (2018)). Using the abundance ratio N(OH)/N(H_2) = 2×10^{-6}, the corresponding H_2 volume density is $\sim 7 \times 10^{-3}$ H_2 molecules cm^{-3}at this location. By changing the excitation and continuum temperatures within reasonable assumptions ($\pm$ 2 K, for either), the volume density could be higher or lower by a factor of 10. This is consistent with the volume density of the diffuse molecular gas phase suggested by Papadopoulos, Thi, and Viti (2002), and consistent with the average molecular volume density of the ISM found by Bohlin, Savage, and Drake (1978).

3.5.3 Implications for Diffuse Molecular Gas in the Outer Galaxy

An estimate of the H_2 mass implied by the broad OH emission from the diffuse OH emission can be calculated using several reasonable assumptions. It is, however, important that we treat this number with caution because the uncertainties involved in this method amount to roughly an order of magnitude. Since we calibrate our OH/H_2 abundance ratio for this sightline in an integrated fashion with dust reddening, we have no knowledge of the evolution of the OH/H_2 abundance ratio in radial velocity (and hence, distance towards the Outer Galaxy). With the assumption of excitation and continuum temperature above, we move forward by transforming our column density of

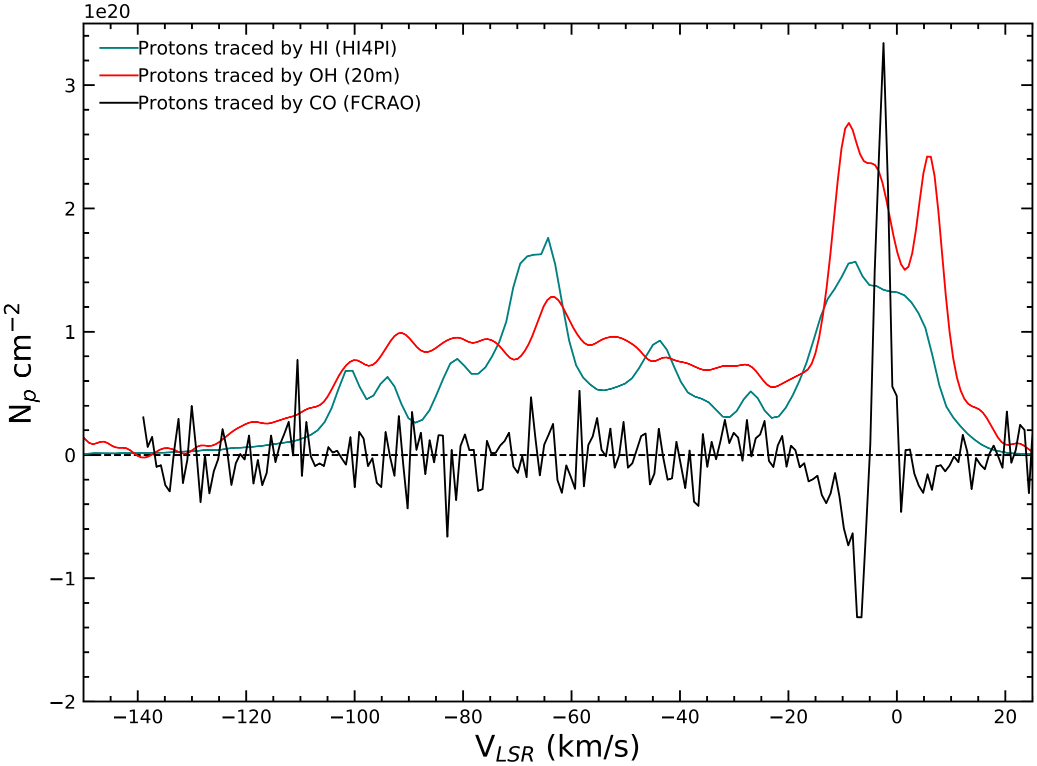

Figure 3.6: The observed HI, OH and CO spectrum from Fig. 3.5, transformed into estimated number of protons traced by each tracer. Estimated number of protons for the atomic gas component is calculated directly from the HI signal; estimated number of protons for the molecular gas component is calculated from the OH signal using our assumed value of N(OH)/N(H_2) of 2×10^{-6}, and from the CO signal using the X(CO) value 2×10^{20} cm^{-2} (K km s^{-1})$^{-1}$ from (Bolatto, Wolfire, and Leroy, 2013). We see that diffuse molecular gas (as traced by OH) may be a component in mass equal to the atomic gas traced by HI, while much of the molecular gas appears to be CO-dark.

OH to H_2 using the abundance ratio calculated in Sect. 3.4.6. The uncertainty in the abundance ratio is the dominant error in the following calculation. While we calculate an N(OH)/N(H_2), it is subject to all of the assumptions implicit in the dust reddening method, and we should also not be using one number for the abundance ratio for the sightline, as there are multiple environments in the spectrum. Nevertheless, if we use the derived abundance ratio, and the X(CO) number we can transform the T_{mb} measurements of the HI, OH and CO spectrum in proton units. This exercise, displayed in Fig. 3.6, shows that diffuse molecular gas (as traced by OH) may be a component in mass equal to the atomic gas traced by HI in the outer Galaxy.

We use a simple geometric model of the outer Galaxy: a cylinder with a hole in the middle corresponding to the solar circle (R = 8 kpc). We calculate the volume of this cylinder as $V = \pi h(r_1^2 - r_2^2)$, where we take the height of the dark molecular disk as 200 pc, which is motivated by observations but will be further investigated in a future paper. In broad strokes, the z-distribution of OH was investigated at the "Perseus Arm" gas velocity ($V_{LSR} = -60$ km s^{-1}), by fitting a Gaussian we were able to measure the scale height of the gas features. We take this as the scale height because it appears that the disk of emission peaks in surface brightness at this feature. We assume a line of sight disk length of R = 25 kpc, which is approximately the extent of the HI disk. The resulting volume of this hollow cylinder is 1×10^{67} cm^3. Using a T_{mb} = 4 mK, the number density is 7 H_2 molecules per liter, the mass in the outer Galaxy can be calculated as: $M = 2m_pVn_{\mathrm{H}_2} \sim 1 \times 10^8$ $M_\odot$ The main uncertainties here are: the excitation temperature of OH and the abundance ratio of OH to H_2 the abundance ratio being the dominant contribution to the uncertainty.

The current literature values of OH/H_2 cluster around $\sim 1 \times 10^{-7}$ (Liszt and Lucas, 1996; Nguyen et al., 2018; Rugel et al., 2018; Jacob et al., 2019); a possible value of the mass using this ratio (which results in 150 H_2 molecules per liter) is $\sim 2 \times 10^9$ $M_\odot$, which is about equal to current estimates of CO-traced H_2 mass in the Galaxy at $\sim 1 \times 10^9 M_\odot$ (Heyer and Dame, 2015), and within an order of magnitude of the HI mass, at $\sim 8 \times 10^9 M_\odot$ (Kalberla and Kerp, 2009).

If we use our calculated value for the abundance ratio for the lower limit of mass, and the literature value of the abundance ratio for the upper limit of the mass, the resulting range of molecular disk mass values is $\sim 10^{8-9}$ $M_\odot$. The existence of a mass of dark H_2 in our Galaxy equal to the CO-bright-traced H_2 has been inferred from the indirect observations of γ-ray (Grenier, Casandjian, and Terrier, 2005) and dust (Planck Collaboration et al., 2011). We provide with this measurement concrete evidence of the existence of these diffuse molecules and, with the radial velocity distribution, the geometry of the diffuse molecular gas as a thick disk beyond the Solar circle. Note that the newly discovered diffuse molecular disk contains CO-dark molecular gas in addition to the previously reported clouds of CO-dark molecular gas found during our OH observing program in the arms of the Galaxy (Allen, Hogg, and Engelke, 2015; Busch et al., 2019). Moreover, it is interesting to examine to what extent the diffuse molecular disk might affect the total baryonic mass of the Galaxy. Using an estimate of stellar mass of $\sim 6 \times 10^{10} M_\odot$ (Licquia and

Newman, 2015; McMillan, 2017) and an estimate of the known mass of the interstellar medium of $\sim 1 \times 10^{10} M_{\odot}$ (Kalberla and Kerp, 2009), we roughly estimate that this newly discovered diffuse molecular disk could increase the baryonic mass estimate of the Galaxy by $\sim$ 0.1 % to $\sim$ 2 %. We anticipate that further sensitive surveys of this broad OH emission throughout the Galaxy will refine the measurement of the mass of the diffuse molecular disk in the future.

The scale height of the diffuse OH emission corresponds extremely well with the thick diffuse molecular gas disk found in M51 in extended CO emission (Pety et al., 2013). This comparison raises the question as to why the CO sightlines in the Milky Way are CO-dark, when the diffuse molecular gas in certain other galaxies others are not. One possible explanation for the detectable CO emission in M51 is the geometric effect of M51 being face-on. This orientation could result in enough radiative trapping in the z-direction for the emission from the diffuse component to be detectable at a sensitivity of $\sim$ 1 K km s^{-1}. We show in Busch et al. (2019) that CO is subthermally excited below its critical density of 1000 cm^{-3}, and below this threshold the surface brightness of CO is heavily dependent on gas volume density. While the CO emission in Pety et al. (2013) appears to come from diffuse molecular gas of n $\sim$ 300-500 cm^{-3}, the OH emission may yet still be tracing an even more diffuse component in addition to the CO-traced diffuse molecular gas because its critical density is n $\sim$ 1 cm^{-3}. A future study intended to search for OH emission from diffuse disks in external galaxies known to contain CO-bright disks, as well as several that do not contain detected CO disks, could provide more information about the differences between conditions in the disks of these galaxies and the properties that lead to a diffuse disk being CO-bright or CO-dark. Such a study could also demonstrate whether OH traces a larger total mass of diffuse molecular gas in these disks even for galaxies that already contain a detectable disk in CO.

Papadopoulos, Thi, and Viti (2002) lays out a theoretical basis for both H_2 formation and shielding at large Galactic distances. They argue that both the ingredients (HI and dust grains) and environmental conditions exist for H_2 formation well inside the Galactic HI disk. The existence of abundant dark H_2 may also shed light on the puzzling star formation behaviours in HI dominated regions (Krumholz, 2013). Star formation correlates with H_2 down to the lowest column densities that can be detected by CO, but then also begins to correlate with HI in the outer parts of the Galaxy. If there were a thick disk of diffuse molecular gas in the outer Galaxy, this may help explain the star formation in the HI dominated portions of the outer Galaxy, as opposed to alternative explanations such as high-velocity runaway stars (Andersson, Renaud, and Agertz, 2021).

Modeling and observations in future papers will have to study the distinction between the OH and CO-traced diffuse molecular gas disks in order to fully understand the transition zone between CO-bright and CO-dark molecular gas.

3.6 Conclusions

We have discovered an extremely broad OH emission profile towards the outer Galaxy that is cospatial with the HI velocity distribution. We have convinced ourselves that it is a real astronomical signal by observing the feature in: both 1667 and 1665 MHz OH lines, two different telescopes with vastly different beams and associated instrumental effects, and using three different data pipelines with which to reduce the data.

This result indicates that the molecular disk of the Galaxy is significantly more extended than previously suspected. We believe that the geometry of the molecular gas traced by the emission is in the form of an extremely diffuse disk, with a thickness observed in the Galactic latitude range $-5^\circ < b < 5^\circ$. The signal is indicative of large-scale structure because it obeys the velocity field of the Galaxy.

A conceptual model of the outer Galaxy using our derived value of the volume density of $\sim$ tens of H_2 molecules per liter (7-70 $\times\ 10^{-3}$ cm^{-3}) results in a molecular mass value for the dark molecular disk of $\sim 10^{8-9}$ $M_\odot$, with the order of magnitude uncertainty resulting from the adopted range of values of the abundance ratio, N(OH)/N(H_2).

We plan multiple follow up surveys to probe the latitude and longitude dependence of the OH emission, and to characterize the structure of the diffuse molecular gas using OH emission. We hope this discovery will motivate similar searches for extremely diffuse molecular gas using dark molecular gas tracers on a large, Galactic scale. We anticipate there is much to learn about

Galactic structure by using an optically thin, widely observed molecular gas tracer in the Galaxy.

3.7 Appendix A: Several Systematic Tests of the OH Emission

In 2015 the first emission from a wide OH feature (nicknamed, "the Pedestal") was observed by R. Allen, D. Hogg and P. Engelke with the 100m Green Bank Telescope (GBT) and later re-observed in 2018 by R. Allen, D. Hogg and M. Busch with the 20m telescope at the GBO (see Fig 3.7). This feature appears to have very a low surface brightness and the emission approached the typical rms level per channel with 2 hours of integration time on the GBT, which has a typical $T_{sys} \sim$ 18K. The "pedestal" appears as a nearly constant surface brightness, wide velocity profile "underneath" the conventional spiral arm emission. The similar velocity structure of the atomic gas tracer (HI) and the molecular gas tracer (OH) suggest that the gas is in the geometry of a thick disk, and co-spatial with the atomic gas. Multiple followup observations were completed at the 10 hour level around l = 108.000$^{/circ}$, B = 3.00$^{/circ}$ to probe the feature.

With 10 hours of integration time, the resulting rms at a velocity resolution of 1 km s^{-1}is close to 1 mK. Typical "pedestal" brightness temperatures per channel are $T_{mb} \sim 1 - 3$mK, and thus the profile integral over the large velocity width ($\Delta v_{LSR} \sim$ 150km s^{-1}) of the *typical "pedestal" results in a signal-to-noise (S/N) of approximately 25.* The pedestal emission also appears clearly in the two main lines of the OH ground state ($\Delta F = 0$) at 1667.359 and 1665.402 MHz.

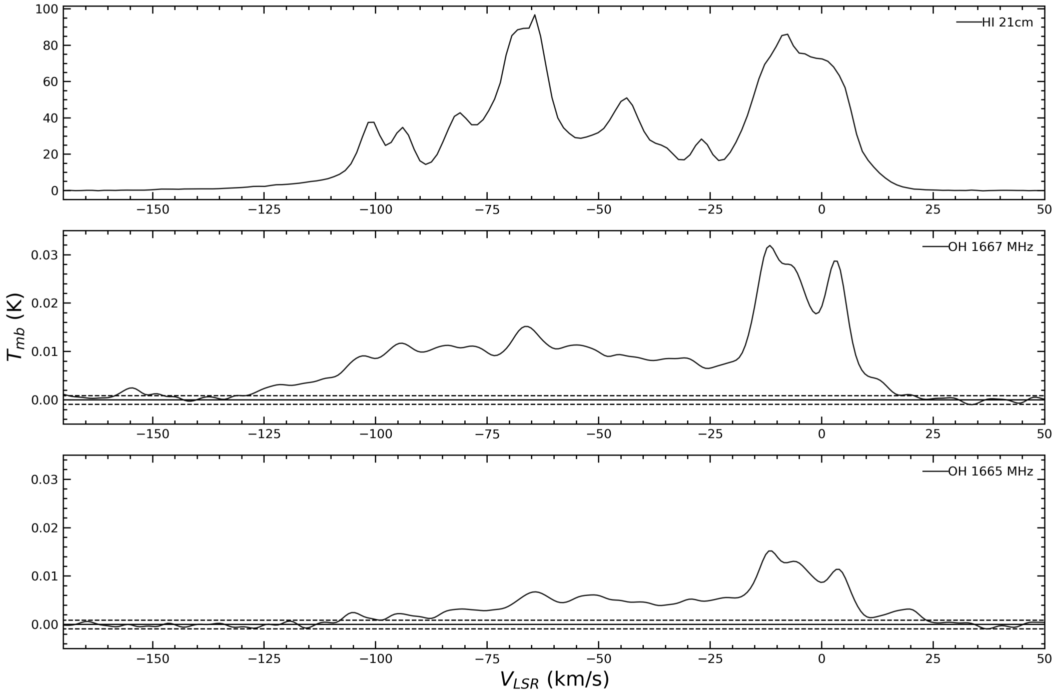

Figure 3.7: The observed 20m OH 1667 pedestal emission toward the outer galaxy compared with HI data from the LAB survey (Kalberla et al., 2005). Note that at these galactic coordinates, no positive emission is expected and none is seen. The dashed lines are the 3σ (corresponding to 1mK) statistical detection limit. We have aligned the local gas emission in the two spectra.

The profile integrals of the observed emission regularly appears to be in the 9:5 LTE ratio set by the quantum mechanical transition strengths (Townes and Schawlow, 1955).

Many different tests were completed to test the robustness of this result in terms of the data reduction itself. Different data pipelines were created with 3 different reduction methods including: fourier filtering (or bandstop filtering), ridge regression (L2 Regularization), general orthogonal polynomial regression. None of the data pipelines generated different pedestal results, therefore we moved forward with using the general orthogonal polynomial fitting as used by *GBTIDL*. We conducted redundant tests in the "order" of polynomial as well. Since the "pedestal" emission is very wide, and the data is frequency-switched, *linear baselines cannot be removed*. Discontinuous regions of the bandpass that do not have "ghosts" introduced by the frequency-switching, or signal from the 1667 and 1665 MHz pedestal, were used ($N_{chans} \sim 6000$) to fit a single high-order polynomial ranging from order 17-23 based on a few different criteria: **a)** there should be no positive velocity emission due to galactic structure, **b)** the order of polynomial does not preferentially subtract or under-subtract signal from the 1667 or 1665 emission at local-gas velocities, **c)** the RMS in the highlighted baseline regions is minimized until no further improvement occurs.

In the following sections we describe three different experiments including: the expected sensitivity in long exposures, inspecting the residuals of the linear polarization data, and inspecting the "ON" and "OFF" phases of the frequency-switched data.

3.7.1 RMS of Extremely Long L-Band Observations

To test the validity and stability of the L-band receiver of the GBT, and whether or not it acts in the expected according to the idealized radiometer equation:

$$\sigma_{T_{mb}} = \frac{T_{sys}}{\sqrt{\Delta v t}} \tag{3.9}$$

We stacked OH spectra from a compilation of data sets we have recently observedd with the GBT. These data sets come from observing project IDs: $AGBT14B\_031B$, $AGBT15B\_004$, and $AGBT19A\_484$. The compiled RMS calculated from *GBTIDL* (Garwood et al., 2006) using the *stats* command in a region of flat baselines with no expected signal or ghosts from the frequency-switched observations. The results are listed in Table 1. The resulting plot is also shown in Fig. 3.8.

The observational results and GBT sensitivity calculator[6] agree remarkably well only after $\sim$ 2-4 hours of integration time. The results demonstrate that while instrumental ripples may be a problem for shorter observing runs, they are not an impediment for extremely long integration times, and may in fact be averaged out after successive observing sessions and integration time is increased. After $\sim$ 6 hours, the observed RMS and calculated RMS is practically identical.

Since the observed brightness temperature of the pedestal emission is faint per channel, we need at least 10 hours of integration time to begin to

---

[6] https://dss.gb.nrao.edu//calculator-ui/war/Calculator_ui.html

notice the pedestal feature. This is why our previous observations of 2 hours were not sufficient enough to detect this signal. There is also a noticeable "point of diminishing returns" on the decreasing RMS around $t \sim 20$ hours. Any further reduction in noise should come from smoothing of the velocity resolution by factors of 2. For example, a 10 hour spectrum with 1 mK RMS at a velocity resolution of 1 km s^{-1}will have an RMS of 0.5 mK at a velocity resolution of 2 km s^{-1}. While the lower resolution is not ideal for studying the narrow emission of the spiral arms, the pedestal emission is a constant surface brightness feature over a large velocity width, making such velocity smoothing a reasonable method to obtain sufficient S/N to detect the pedestal emission at high S/N.

3.7.2 Separating Linear Polarization Data

Since the pedestal emission is expected to be thermal emission, it is important to confirm the emission is unpolarized. It is expected that the radiation mechanism is largely from collisional excitation between OH and H atoms, either in the atomic of molecular form. Thus, the emission should not be polarized. If the emission were only detected in one polarization, that would indicate that it would be some type of systematic error that we were previously not accounting for.

In this experiment, we stacked five GBT OH spectra towards l = $108.000^{/circ}$, B = $3.00^{/circ}$, keeping the linear polarizations separate throughout the reduction. Then, the spectra are smoothed to a velocity resolution of 1 km s^{-1}. The XX and YY spectra are displayed in the top two panels of Fig. 3.10. The

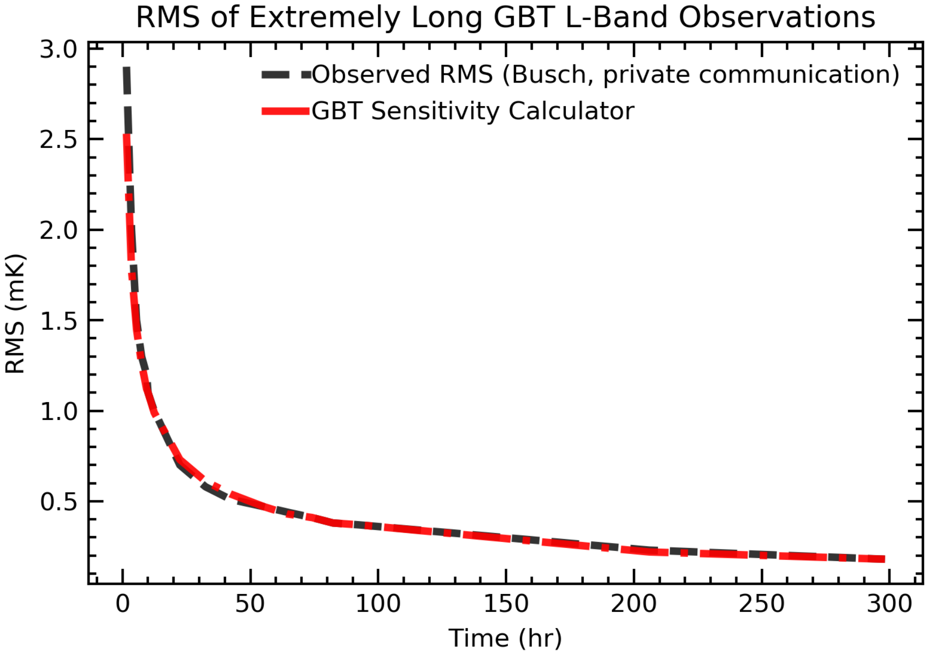

Figure 3.8: The observed RMS plotted against the RMS calculated from the GBT sensitivity calculator in a linear scale to demonstrate the disagreement at shorter integration times.

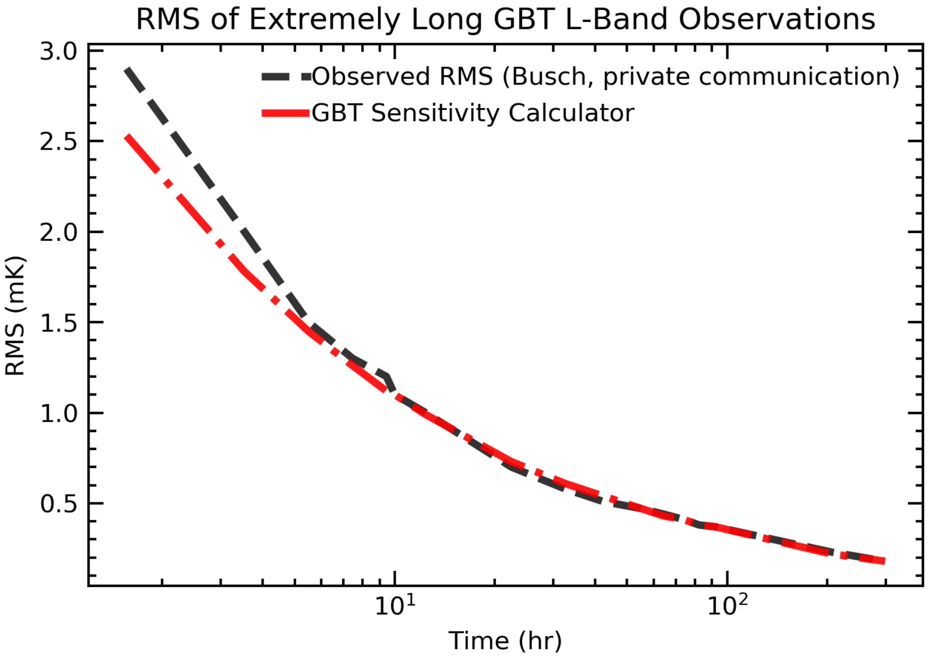

Figure 3.9: The observed RMS plotted against the RMS calculated from the GBT sensitivity calculator in a logarithmic scale to demonstrate the disagreement at shorter integration times.

residual spectrum of XX-YY is also shown to demonstrate that the two polarizations behave differently at a very small level. The YY polarization is known to have additional spectral baselines than the XX polarization due to multipath scattering, discovered during the commissioning of the GBT (Fisher, J. R., Norrod, R.D., and Balser, D.S. 2003, Electronic Division Internal Report No. 312). The resulting integration time on the spectra in Fig. 3.10 is approximately 40 hours with a RMS noise of T_{RMS} = 300 μ K. The systematic from the YY spectrum is at the level of 0.5-0.6 mK, however the brightness temperature of the pedestal 1667 MHz emission is higher at $T_{mb} = 1 - 3mK$, and the 1665 MHz emission is about half of that, allowing a detection of this feature at high S/N, especially if only using XX data.

We rule out that the emission from the this feature is a polarized systematic baseline ripple in the GBT. It appears to behave like OH thermal emission.

3.7.3 Separating the "ON" and "OFF" Pedestal Emission

The observations in *AGBT15B_004* were experimented on in several stages of the frequency switching process in order to test different parts of the intermediate frequency (IF) system to make sure the signal was not introduced by some previously unknown systematic that was unaccounted for. Our observations are completed with in-band frequency switching (see e.g. O'Neil, 2002), the reference measurement of ON-OFF is completed by shifting the central frequency 2 MHz and differencing the spectrum. When we perform in-band frequency switching, the science signal is still present in the "OFF"

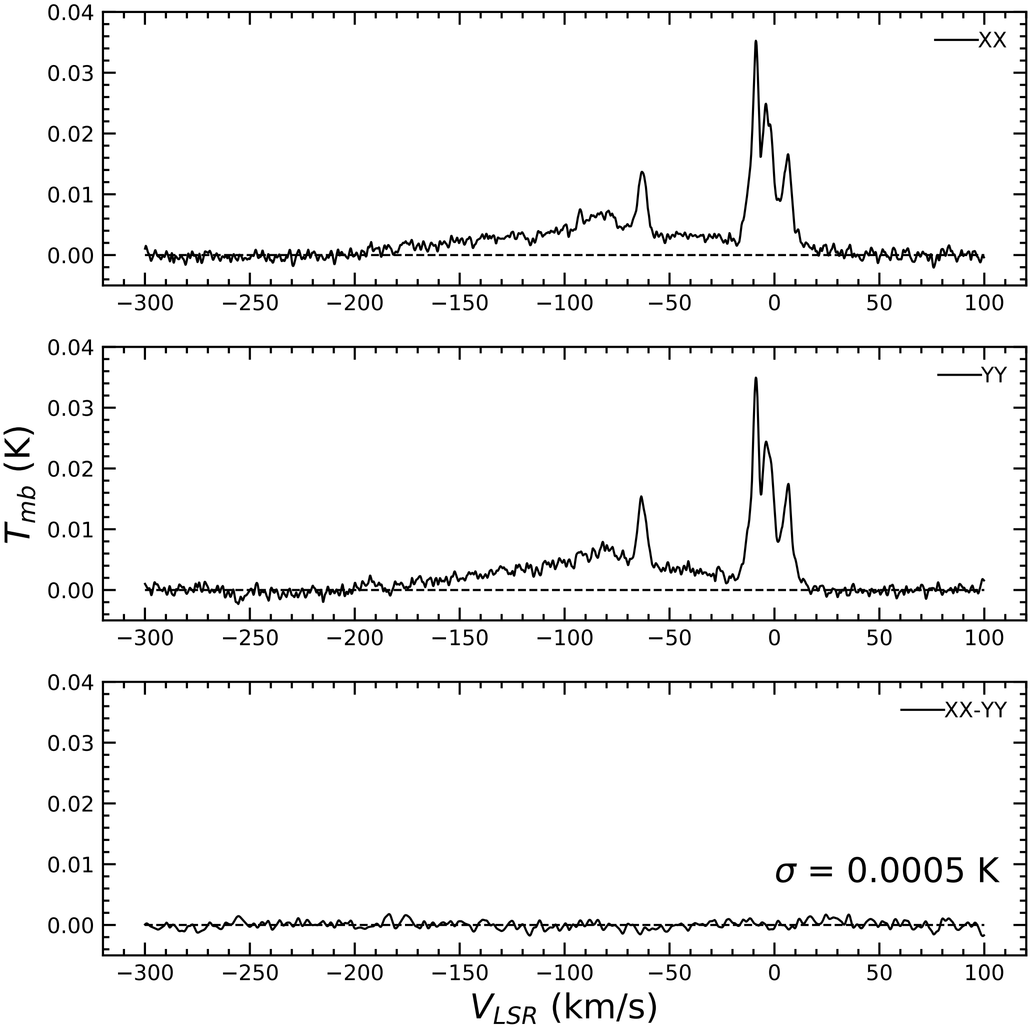

Figure 3.10: Top Panel: A stacked 40 hr spectrum of XX linear polarization. Middle Panel: A stacked 40 hr spectrum of YY linear polarization. Bottom Panel: The resulting residual spectrum from XX-YY. The residual noise is possibly from an additional known spectral ripple in the YY polarization due to the geometry of the GBT itself (Fisher, J. R., Norrod, R.D., and Balser, D.S. 2003, Electronic Division Internal Report No. 312). This noise is responsible for the *systematic error* reported in our measurement. In this example, it is roughly double the statistical error, and dominates the reported errors. It approximately translates into a 6% error on the total profile integral.

measurement, and the final reduced signal is compiled by shifting and averaging the "OFF-ON" and "ON-OFF" measurements to decrease the noise in the final RMS by $\sqrt{2}$. This process is demonstrated in Fig. 3.1.

In each separate ON-OFF and OFF-ON signal, we should expect two signals from the two OH lines, and the so-called "ghosts" of the subtracted signals from the shifted frequency. Whichever phase is "ON" or "OFF" is arbitrary. However, it is important that we check if the pedestal is introduced in one part of the IF by appearing in one of the "phases" and not the other. If it were to appear in "ON" but not "OFF", this would raise the alarm of an unknown systematic. However, we show in Fig. 3.1 that this is not the case, and the positive and negative signals of the pedestal signal are clearly visible in both reference spectra. The final product of the frequency switched measurement is shown in the bottom panel of Fig. 3.1, where the "OFF-ON" measurement is shifted and averaged together with the "ON-OFF" measurement. In this final spectrum, we would expect the two signals, and four ’ghosts’ (or negative, subtracted signals), making baseline fitting of such wide, frequency-switched signals requiring more than linear baselines (typically used in position-switched measurements), as explained above.

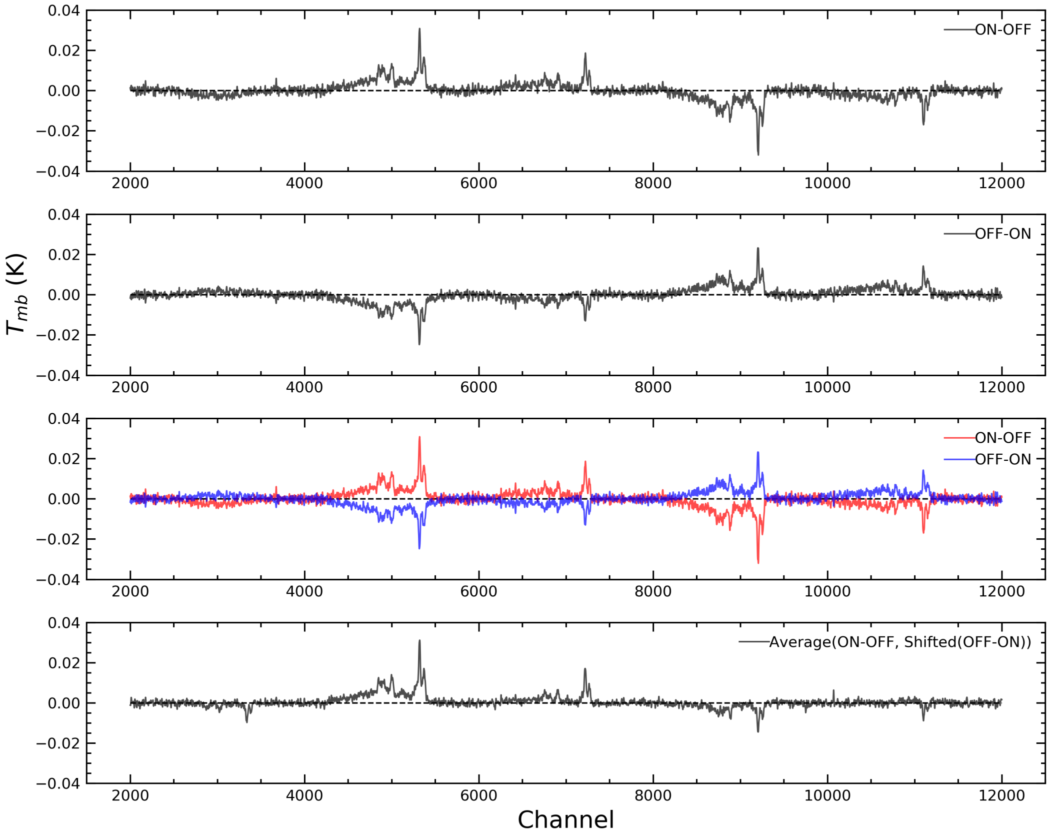

Figure 3.11: The top two panels are the "ON-OFF" phase and "OFF-ON" phase plotted separately. The third panel is an overplot demonstrating the features of the pedestal in the middle of the data reduction. The final spectrum is a shift and average of the top two spectra, typical of frequency-switching measurements.

References

Ackermann, M. et al. (2010). *ApJ* 726.

Allen, R. J., D. E. Hogg, and P. D. Engelke (2015). *AJ* 149.4, p. 14.

Allen, R. J. et al. (2012). *AJ* 143.4, p. 8.

Allen, R. J. et al. (2013). *AJ* 145.3, p. 85.

Andersson, E. P., F. Renaud, and O. Agertz (2021). *MNRAS* 502.1, pp. L29–L34.

Ben Bekhti, N. et al. (2016). *A&A* 594, p. 116.

Blitz, L., D. Bazell, and F. X. Desert (1990). *ApJ* 352, p. L13.

Bohlin, R. C., B. D. Savage, and J. F. Drake (1978). *ApJ* 224, p. 132.

Bolatto, A. D., M. Wolfire, and A. K. Leroy (2013). *ARAA* 51, pp. 207–268.

Brand, J. and L. Blitz (1993). *A&A* 275, pp. 67–90.

Burton, W. B. and P. te Lintel Hekkert (1985). *A&AS* 62, p. 645.

Busch, M. P. et al. (2019). *ApJ* 883.2, p. 158.

Cardelli, J. A., G. C. Clayton, and J. S. Mathis (1989). *ApJ* 345, p. 245.

Dame, T. M., D. Hartmann, and P. Thaddeus (2001). *ApJ* 547.2, pp. 792–813.

Dawson, J. R. et al. (2014). *MNRAS* 439.2.

Dickey, J. M. and J. M. Benson (1982). *AJ* 87.2, p. 278.

Dickey, J. M., J. Crovisier, and I. Kazes (1981). *A&A* 98, pp. 271–285.

Draine, B. T. (2011). Princeton University Press, p. 540.

Engelke, P. D. and R. J. Allen (2018). *ApJ* 858.

Engelke, P. D. and R. J. Allen (2019). *ApJ* 874.1, p. 49.

Engelke, P. D., R. J. Allen, and M. P. Busch (2020). *ApJ* 901.1, p. 50.

Fisher, J. R., R. D. Norrod, and D. S. Balser (2003). Tech. rep. NRAO Electronics Division Internal Report No. 312.

Fukui, Y. et al. (2015). *ApJ* 798.1.

Garwood, R. W. et al. (2006). *ASPC* 351, p. 512.

Glover, S. C. O. and T. Abel (2008). *MNRAS* 388.4, pp. 1627–1651.

Goldsmith, P. F. et al. (2010). *ApJ* 715.2, pp. 1370–1382.

Goss, W. M. (1968). *ApJS* 15, p. 131.

Green, C. E. et al. (2017). *ApJS*, p. 12.

Grenier, I. A., J.-M. Casandjian, and R. Terrier (2005). *Sci* 307.5713, pp. 1292–1295.

Heiles, C. E. (1968). *ApJ* 151, p. 919.

Heithausen, A. et al. (1993). *A&A* 268, pp. 265–275.

Heyer, M. and T. M. Dame (2015). *Annu. Rev. Astron. Astrophys* 53, pp. 583–629.

Heyer, M. H. et al. (1998). *ApJS* 115.2, pp. 241–258.

Jacob, A. M. et al. (2019). *A&A* A60.636.

Jacob, A. M. et al. (2020). *A&A* 640.

Kalberla, P. M. W. et al. (2005). *A&A* 440.2, pp. 775–782.

Kalberla, P. M. and J. Kerp (2009). *ARA&A* 47.1, pp. 27–61.

Krumholz, M. R. (2013). *MNRAS* 436.3, pp. 2747–2762.

Li, D. et al. (2015). *PKAS* 30.2.

Li, D. et al. (2018). *ApJS* 235.1, p. 1.

Licquia, T. C. and J. A. Newman (2015). *ApJ* 806.1, p. 96.

Liszt, H and R Lucas (1996). *A&A* 314, pp. 917–926.

Liszt, H., J. Pety, and R. Lucas (2010). *A&A* 518, p. 45.

M. Green, G. (2018). *JOSS* 3.26, p. 695.

Mangum, J. G. and Y. L. Shirley (2015). *PASP*.

McMillan, P. J. (2017). *MNRAS* 465.1, pp. 76–94.

Murray, C. E. et al. (2018). *ApJ* 862.

Neufeld, D. A. and M. G. Wolfire (2016). *ApJ* 826.2, p. 12.

Nguyen, H. et al. (2018). *ApJ* 862.

O'Neil, K. (2002). *PASP* 278, pp. 293–311.

Papadopoulos, P. P., W. Thi, and S. Viti (2002). *ApJ* 579.1, pp. 270–274.

Peek, J. E. G. et al. (2011). *ApJS* 194.2, p. 13.

Pety, J. et al. (2013). *ApJ* 779.1, p. 43.

Petzler, A., J. R. Dawson, and M. Wardle (2020). *MNRAS* 497.4, p. 4066.

Planck Collaboration et al. (2011). *A&A* 536, p. 16.

Prestage, R. M. et al. (2015). *2015 USNC-URSI Radio Science Meeting (Joint with AP-S Symposium)*. IEEE, pp. 294–294.

Reich, P. and W. Reich (1988). *A&AS* 74, pp. 7–23.

Reid, M. and M. Honma (2014). *ARA&A* 52.1, pp. 339–372.

Rugel, M. R. et al. (2018). *A&A*.

Schlafly, E. F. et al. (2016). *ApJ* 821.2, p. 78.

Schlafly, E. F. and D. P. Finkbeiner (2010). *ApJ* 737.2, p. 103.

Schlegel, D. J., D. P. Finkbeiner, and M. Davis (1997). *ApJ* 500.2, pp. 525–553.

Strasser, S. T. et al. (2007). *AJ* 134.6, pp. 2252–2271.

Taylor, A. R. et al. (2003). *AJ* 125.6, pp. 3145–3164.

Townes, C. H. and A. L. Schawlow (1955).

Turner, B. E. and C. Heiles (1971). *ApJ* 170, p. 453.

Wannier, P. G. et al. (1993). *ApJ* 407, p. 163.

Weinreb, S. et al. (1963). *Natur* 200.4909, pp. 829–831.

Weinreb, S. et al. (1965). *Nature* 208.5009, pp. 440–441.

Weselak, T. et al. (2010). *MNRAS* 402.3, pp. 1991–1994.

Winkel, B. et al. (2015). *A&A* 585, p. 22.

Wolfire, M. G., D. Hollenbach, and C. F. McKee (2010). *ApJ* 716.2.

Xu, D. and D. Li (2016). *ApJ* 833.1, p. 90.

Xu, D. et al. (2016). *ApJ* 819.1, p. 22.

Yuan, L. and C. Wallace (1973). *ApJ* 185, p. 453.

Chapter 4

First Detection of Thermal 18cm OH Emission in Another Galaxy: A Pilot search for 18cm OH in M31

4.1 Introduction

The hydroxyl radical (OH) was the first molecule discovered in the radio regime in absorption against Cas A almost 60 years ago (Weinreb et al., 1963). Surveys for OH in our own Galaxy quickly revealed that absorption measurements were far easier to carry out than emission due to the often times low excitation temperature (a few K above background continuum) of the Λ-doubling OH ground state main lines (Penzias, 1964). The first major survey for OH was carried out by Goss (1968) in absorption. Within a year, the detection of OH emission was announced by Weaver et al. (1965); however the discovery of the masing phenomenon of the OH molecules captured the most attention (Baan and Haschick, 1987)[1]. It was the discovery and detection

---

[1] Additional historical information concerning the early observations and discoveries of OH in both emission and absorption can be found in Allen et al. (2012).

of the CO molecule, and its relative brightness and abundance, that led to it taking over as the choice tracer for H_2 (for a review see, Bolatto, Wolfire, and Leroy, 2013; Heyer and Dame, 2015).

Early work towards detecting OH in external Galaxies were largely prohibited once again by lack of sufficient sensitivity. The first systematic search for OH in 63 nearby spiral galaxies was led by Schmelz and Baan (1988) using the 305m Arecibo Observatory, which failed to detect any OH. An early search for OH in the Large Magellanic Cloud (LMC) using the Parkes Telescope also failed to detect OH emission (Radhakrishnan, 1967). The detection of masing emission from OH/IR stars in the LMC (Wood, Bessell, and Whiteoak, 1986) prompted additional searches for OH masers in the Magellanic clouds (Wood et al., 1992). A large absorption survey of OH in the Magellanic systems is expected to be carried out by GASKAP this decade (Dickey et al., 2013). A recent search for OH absorption using the FAST telescope by Zheng et al. (2020) failed to detect any extragalactic OH absorption sources, but placed stringent upper limits, and also reviewed the existing literature on extragalactic OH absorption sources, which we recommend for the interested reader.

Local group galaxies are natural choices for the first searches for faint OH emission because they can be resolved by current available telescopes, allowing for future experiments to be carried out to trace both the OH and CO detections along an axis of these galaxies and for a direct comparison of the H_2 traced by multiple molecular tracers. Such studies will allow for a statistical comparison and check of the efficacy of using the CO as a tracer of the total H_2 reservoir of galaxies. Having more *molecular* tracers (as opposed to indirect gas tracers, like dust extinction) could also offer a possible calibration for the CO-to-H_2 conversion factor (usually called X(CO)) that will account for CO-dark molecular gas (or 'dark gas') in extragalactic CO measurements. Hydrides like OH (Wannier et al., 1993; Allen et al., 2012; Allen et al., 2013; Allen, Hogg, and Engelke, 2015; Nguyen et al., 2018; Busch et al., 2019; Engelke and Allen, 2018; Engelke and Allen, 2019; Donate et al., 2019; Donate, White, and Magnani, 2019; Engelke, Allen, and Busch, 2020; Busch et al., 2021; Tang et al., 2021) and CH (Neufeld and Wolfire, 2016; Chastain, Cotten, and Magnani, 2009; Weselak et al., 2010; Xu and Li, 2016; Jacob et al., 2019; Jacob et al., 2020) seem particularly promising for this enterprise. Such efforts to calibrate X(CO) for extragalactic measurements have made great strides recently by using [CII] and to account for the total carbon budget in galaxies (see e.g. Madden et al., 2020, and references therein).

The recent renewed interest in faint OH emission is primarily due to the utility of OH to trace the 'CO-dark' molecular gas. The diffuse molecular gas phase is the second most massive in the ISM after the atomic phase, due to its much larger volume than the 'CO-bright' component of the molecular gas, which is observed to be clumpier, filamentary, and colder (Heyer and Dame, 2015). In contrast, the diffuse molecular gas fills more volume, but is largely invisible to conventional all-sky CO surveys (Grenier, Casandjian, and Terrier, 2005; Pineda et al., 2013; Wolfire, Hollenbach, and McKee, 2010; Planck Collaboration et al., 2011; Allen et al., 2012; Allen et al., 2013; Allen, Hogg, and Engelke, 2015; Rugel et al., 2018; Busch et al., 2019).

The theory posited in Busch et al. (2019) and Engelke, Allen, and Busch

(2020) explaining why OH can trace the dark gas relies on the concept of the critical density of the two tracers. This is the density required to balance the collisional excitation rate with H_2 and the spontaneous emission rate of the molecular line. This density for the optically thin approximation of CO(J=1-0) is 1000 cm^{-3} (Bolatto, Wolfire, and Leroy, 2013), whereas for 18cm OH this critical density is 1 cm^{-3}, meaning that the brightness of the OH line will not be a strong function of volume density in most quiescent ISM environments. The CO(J=1-0) line, on the other hand, quickly becomes fainter and subthermally emitting as most of the molecules will lie in the J=0 state (Yang et al., 2010), and the practical implication of this is that all-sky CO surveys will be biased towards gas volume densities approaching and above the critical density. Some authors argue for increased sensitivity in CO surveys (Donate and Magnani, 2017) to lower the fraction of ′dark gas′ in CO surveys. This will indeed will help, but undoubtedly there will still exist large fractions of diffuse molecular gas that will be primarily 'CO-free' (Wolfire, Hollenbach, and McKee, 2010; Li et al., 2018), where the gas phase carbon will reside in C^0 or C^+ rather than CO, due to the lack of sufficient self-shielding from the interstellar radiation field.

In this paper we present, to our knowledge, the first detection of thermal OH emission in another Galaxy, M31. We stress that by 'thermal', we mean strictly that the emission is not obviously caused by discrete maser sources, which would require specific energetic physical processes (Elitzur and Moshe, 1990; Elitzur and Moshe, 1992; Lockett, Gauthier, and Elitzur, 1999; Hewitt, Yusef-Zadeh, and Wardle, 2008), and is instead likely from an extended diffuse molecular gas distribution; analogous to the recently discovered thick disk of diffuse molecular gas in the Milky Way (Busch et al., 2021). Maser emission is markedly brighter, and results in line ratios inconsistent with the LTE ratio (1:5:9:1). Historically, the type of emission discussed in this paper has been called 'normal' to distinguish from the masing OH emission (e.g. Heiles, 1968). The lack of previous thermal OH emission detections is not surprising given the growing body of literature that has demonstrated that the excitation temperature of the ground-state OH lines are usually close to the background continuum, and thus the emission is suppressed and faint (Dawson et al., 2014; Li et al., 2018; Engelke and Allen, 2018; Busch et al., 2019; Engelke, Allen, and Busch, 2020).

In section 4.2 of this paper we discuss the technical aspects of the observations, the search construction and rationale. In section 4.3 we explain the source of CO data that we choose to compare our results to. Section 4.4 briefly explains how the GBT data were reduced using *GBTIDL*. In section 4.5 we present the profile integrals, line parameters, uncertainties and statistical significance of the observed OH emission profiles. Section 4.6 presents the calculation of the dark H_2 traced by OH and relevant discussion of uncertainties, along with a discussion about the relation of OH and HI emission. We conclude the paper with a look forward to potential further extragalactic searches for thermal OH emission.

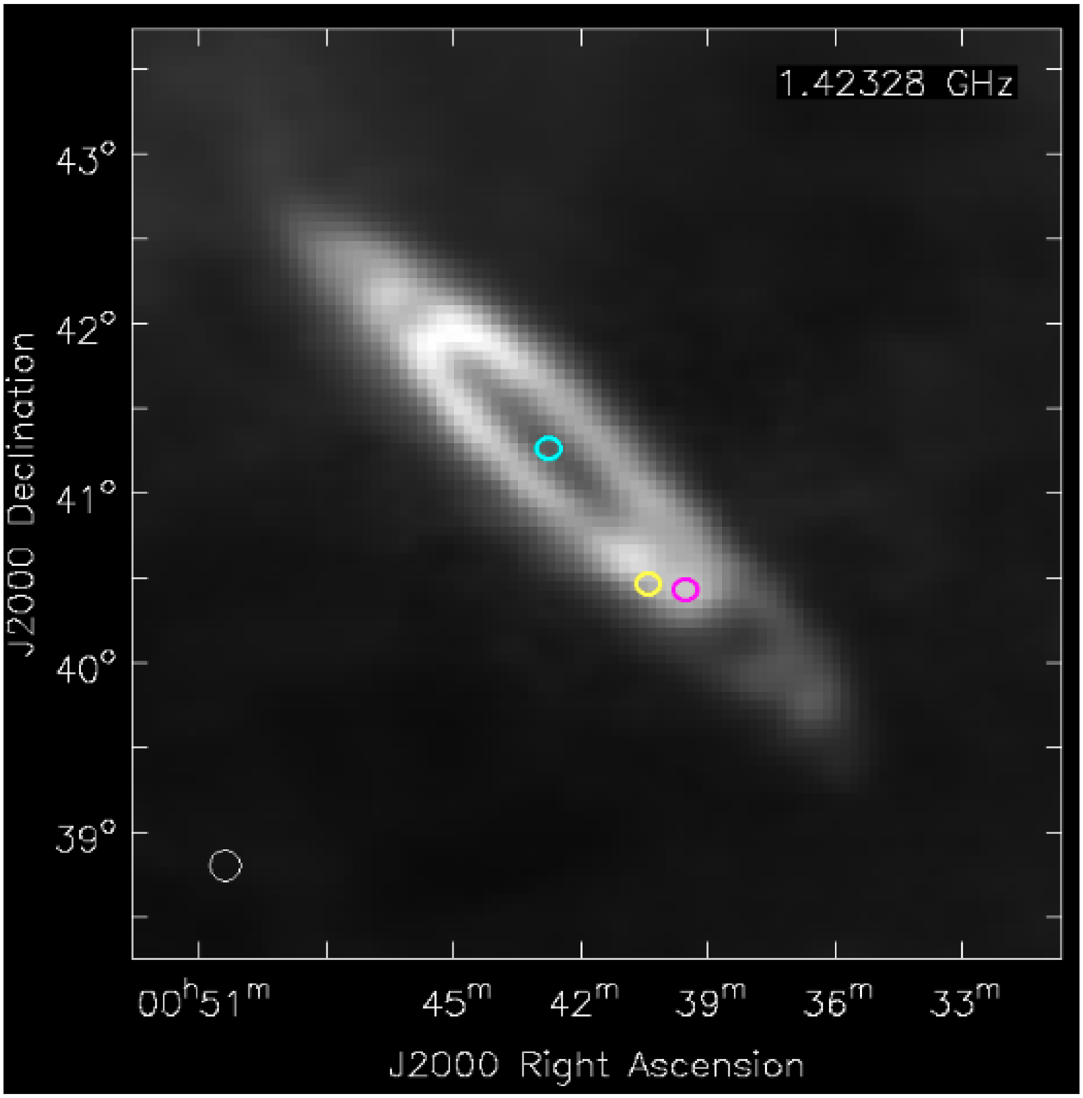

Figure 4.1: An HI emission map of M31 from the EBHIS survey (Winkel et al., 2015). The beam size of the Effelsburg telescope at 21cm is shown in the bottom left. Overlaid are apertures the size of approximately the GBT beam at 18cm (7.6′). The nucleus of M31 (teal) is shown for reference at $\alpha = 0^h42^m44^s$, $\delta = +41°16'$ (J2000). The spectroscopic measurement of 18cm OH (magenta) is also shown at $\alpha = 0^h39^m32^s$, $\delta = +40°26'$ (J2000), approximately 62′ from the nucleus, aligned with the major axis of the galaxy. The yellow aperture is the sightline with a non-detection at $\alpha = 0^h40^m24^s$, $\delta = +40°28'$ (J2000).

.

4.2 Observations

We have observed the ground state, Λ-doubling OH emission lines at 18 cm as well as the 21 cm HI line with the 100m Robert C. Byrd Green Bank Telescope, located in the radio quiet zone of Green Bank, West Virginia. These observations involved frequency-switching by 2 MHz centered on 1420, 1617, 1665, and 1720 MHz (O'Neil, 2002) using the VEGAS spectrometer in the 1.15 - 1.73 GHz ("L-band") range (Prestage et al., 2015). The observations cover all four ground-state OH emission lines, although the 1612 MHz band is unusable due to radio frequency interference (RFI).

The receiver is a single-beam, dual-polarization instrument, with an effective system temperature in the range of 16-20 K, depending upon the weather and the background continuum emission. The observed signal is fed through an IF system to the control room, for which we have a chosen a bandwith of 11.7 MHz in order to minimize the possibility of harmful radio interference. The beam size of the GBT at 18 cm is 7.6′. The antenna efficiency of the GBT in this frequency band is $\eta = 0.95$, as determined by NRAO staff[2]. Thus the antenna and main-beam brightness temperatures, $T_{mb} = T_A/0.95$, are virtually identical; we choose to present the data in T_{mb}.

Two sightlines (see Fig. 4.1) were observed in the summer of 2020 under project ID AGBT20A_556, which was proposed in response to a call for Director's Time proposals during the observatory's infectious disease operating status. The lack of observatory staff on site limited receiver changes during this time. 70 hours were requested for this exploratory search.

---

[2] https://www.gb.nrao.edu/GBT/Performance/PlaningObservations.htm

As the OH emission is expected to be faint from experience (Allen et al., 2012; Busch et al., 2019; Busch et al., 2021), any mapping or grid surveys of local group galaxies would likely take hundreds of hours with a single-beam receiver, and necessitate a larger observing program.

4.2.1 Blind Search Construction

This search for OH emission in M31 was blind, and not directed at any previously discovered supernova remnant, HII region, or any potential absorption source. The sightlines were chosen for predominantly two reasons: firstly, they were far away enough ($\sim$ 13 kpc from the nucleus) from the canonical molecular ring of M31 as detected in CO (Dame et al., 1993) to be astronomically interesting as any OH emission would likely be linked to 'CO-dark' molecular gas (Wannier et al., 1993; Grenier, Casandjian, and Terrier, 2005; Wolfire, Hollenbach, and McKee, 2010; Li et al., 2015; Li et al., 2018). Secondly, we chose sightlines that had relatively bright HI emission, as recent OH surveys in our Galaxy have empirically shown that HI and OH emission are tightly correlated (Allen et al., 2012; Busch et al., 2021). We used the relation from Allen et al. (2012): $T_{mb}(OH_{1667}) = 1.5 \times 10^{-4}\ T_{mb}(HI)$ (with a suggested scatter of 3mK) as a guide to our OH observations.

4.3 Archival CO Data

.

In comparing the OH emission to the canonical molecular gas tracer, CO, we opt to compare with the 1.2 mm telescope at the Harvard Center for

Astrophysics (CFA) (Dame et al., 1993). This survey has observed all of M31 out to a radius of at least 15 kpc, which is well suited to compare to our data set because it's beamsize is similar at 8.7′ to the GBT beam at OH (7.6′), and it is extremely sensitive, at an RMS of 18mk per 1.3 km s^{-1}channel.

4.4 Data Reduction

The HI observations required no correction for baselines at the scale of interest here. The OH data required more careful treatment. Each 10 minute scan in each polarization is reviewed for the presence of interference or other instrumental problems. In general, little editing is needed. After averaging, the final spectra are smoothed by Gaussian convolution (with decimation) by 27 channels to a velocity resolution of 4 km s^{-1} to decrease rms noise per channel. An order 4 polynomial baseline was subtracted from the final baseline by fitting 100 km s^{-1} on either side of the expected signal. The boundaries for the baseline fitting followed the extent of the HI emission. This was done using the usual baseline fitting procedures in *GBTIDL* (Garwood et al., 2006).

4.5 Results

These results pertain to the sightline with the OH detection (magenta in Fig. 4.1). The observed HI and OH spectra from the GBT are displayed in Figure. 4.2. Before smoothing and decimation, the noise is in the spectrum is approximately 5mK, the spectral resolution is 1.88 kHz corresponding to a

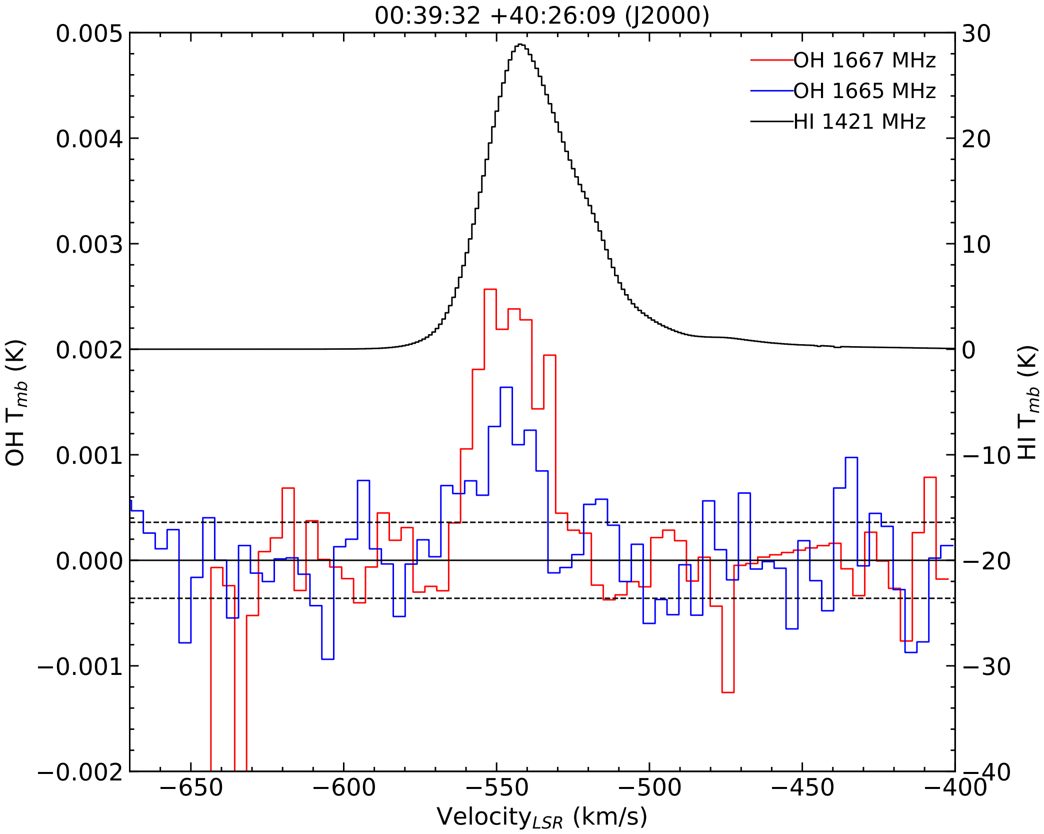

Figure 4.2: 21cm HI and 18cm OH lines overplotted. The scale on the left axis is for the OH data while the right is for HI. Both spectra were smoothed to 4 km s^{-1}per channel with decimation. The dashed line corresponds to ± 1-σ statistical noise, $\Delta T_{mb} \sim 0.4$mK. The steep drop off at the edge of the bandpass at -650 km s^{-1}in the 1667 MHz spectra is an artifact of baseline subtraction.

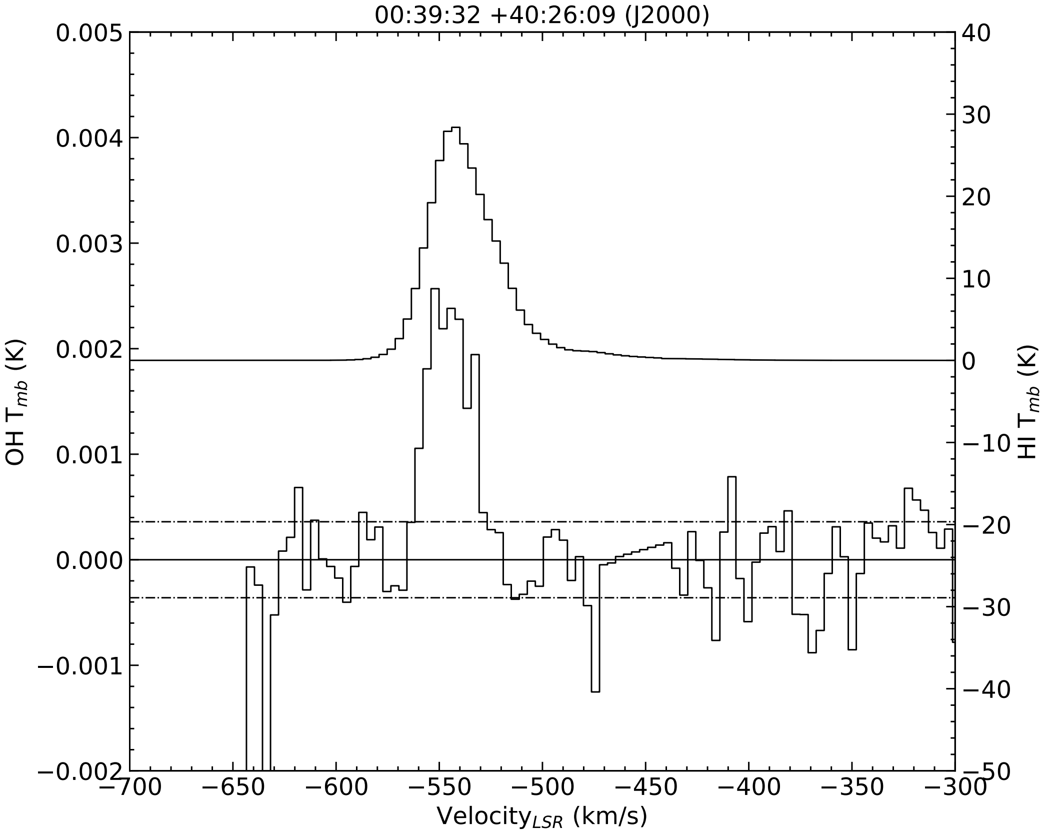

Figure 4.3: Both sightlines discussed in this paper. OH was detected at the coordinates presented in the left panel. No significant OH signal was detected in the right panel (the 1667 MHz line is shown). Both OH spectra were reduced using the same procedures discussed in Section 4.4. The observed GBT HI spectra for both positions are also overplotted. The dashed line corresponds to ± 1-σ statistical noise, Δ T_{mb} $\sim$ 0.4mK.

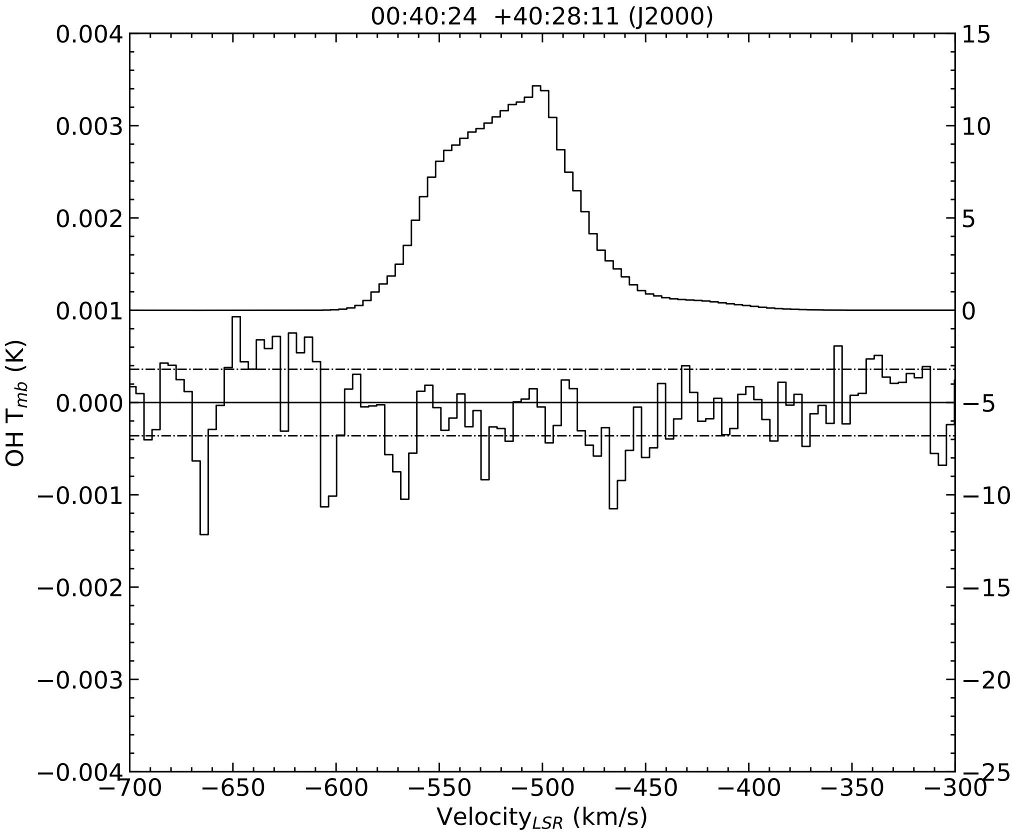

Figure 4.4: Same as Fig. 4.3

velocity resolution of 0.34 km s^{-1}. The resultant noise per channel is 0.4 mK at the final chosen velocity smoothing of 4 km s^{-1}, which corresponds to a spectral resolution of 22.24 kHz.

The peak of the OH emission at 1667 MHz is 2.4 mK, whereas the peak of the 1665 MHz emission is is 1.5mK, close to the expected LTE ratio of the lines. The 1612 MHz line is unusable due to RFI at Green Bank. We do not detect any emission, or absorption, in the 1720 MHz line. If the 1720 MHz emission were in LTE (1:5:9:1) as well, then the peak emission would be buried in the noise, as $T_{mb,1720} = T_{mb,1667}/9 \sim 0.3$ mK. As the rms noise per channel is about 0.4 mK, it makes physical sense for 1720 MHz emission to be absent at the sensitivity of the observations discussed here.

4.5.1 Line Profiles, Widths and the OH Line Ratio

We analyze the HI and OH profiles by fitting a Gaussian profile to each line to derive the line parameters: the line integral, velocity dispersion, line width, line center, and their corresponding statistical uncertainties. We used the interactive routine *fitgauss* in the *GBTIDL* software. The profile integral of the OH 1667 and 1665 MHz lines appear to be in the expected LTE ratio: R = $\int T_{67}\, dv / \int T_{65}\, dv = 1.8$, at least within the statistical error. The FWHM of the HI and OH (1667 and 1665 MHz) profiles are 36.73 ± 0.35 km s^{-1} 31 $\pm$ 31.58 $\pm$ 2.07 km s^{-1} and 32.21 ± 0.43 km s^{-1} respectively. The similar morphology of the velocity width between the HI and OH appear to indicate that both are obeying the velocity structure of galactic rotation experienced along the line of sight.

The integrated line emission, W(OH), from -600 km s^{-1} to -500 km s^{-1} are 0.056 ± 0.008 K km s^{-1} and 0.039 ± 0.008 K km s^{-1} for the 1667 and 1665 MHz lines respectively. This corresponds to a S/N of 7 for W(OH_{1667}) and 5 for W(OH_{1665}). As the 1665 MHz OH line is expected to be weaker in the LTE ratio, this is not surprising.

The statistical error in W(OH) is calculated as the square root of the number of channels ($\mathrm{N}_{chan} \sim$ 100-110) in the profile integral times the 1-σ baseline rms. The rms is calculated by the *stats* routine in *GBTIDL* between -900 km $\mathrm{s}^{-1}$and -600 km s^{-1} (where no signal is present). Typical rms values calculated this way are in the range of $\Delta \mathrm{T}_{mb}$ = 0.4-0.5 mK, with a slight dependence on the order of baseline polynomial subtracted.

4.5.2 Column Densities of HI and OH

The beam-averaged column density of HI can be calculated in the optically thin assumption by (e.g. Dickey and Benson, 1982). The optically thin assumption leads to a lower limit for the HI column density. The column density can be calculated directly from the measured T_b:

$$\langle N(\mathrm{HI}) \rangle = C_0 \int \Delta T_b(v) dv; \tag{4.1}$$

where the constant C_0 is 1.82×10^{18} cm^{-2} K km s^{-1} . The beam-averaged column density of OH $\langle N(OH) \rangle$ along the line of sight is calculated by (e.g. Liszt, Pety, and Lucas, 2010; Allen et al., 2012; Allen, Hogg, and Engelke, 2015; Busch et al., 2019):

$$\langle N(\mathrm{OH})\rangle = C_0 \left[\frac{T_{ex}}{T_{ex} - T_c}\right] \int \Delta T_b(v) dv; \tag{4.2}$$

where $\Delta T_b^{67}(v)$ is the (main beam) brightness temperature of the OH emission profile from the cloud as observed in one of the 18-cm OH transitions, minus an estimate of the underlying radio continuum brightness at the same radial velocity; T_{ex}^{67} is the excitation temperature for either the 1667 or 1665 line; T_c is the brightness of the continuum emission at 1666 MHz incident on the back surface of the cloud, and the integration over velocity includes all the molecular emission thought to arise in that particular cloud.

We require a reasonable measurement of the continuum temperature, T_c in order to calculate the OH column density. The usual prescription is to find a continuum survey at a similar frequency and assume a spectral index. We choose the 20.5cm (1462 MHz) Effelsburg+VLA continuum survey of M31 presented in Beck, Berkhuijsen, and Hoernes, 1998. Inspecting their Figure 4 map, we adopt the intensity range of 5-1 mJy/beam. Using their angular resolution of 45 arcseconds, we transform this to temperature units and then use the following equation to calculate T_C at 18cm (1666 MHz) assuming a spectral index of -2.8:

$$T_{c,1666} = 2.7 + T_{C,1462}(1666/1462)^{-2.8} \tag{4.3}$$

This results in a typical T_C in the range of 2.8-2.9K.

We assume an excitation temperature of the OH lines from the distribution found in Li et al. (2015), which samples diffuse sightlines in the Milky Way.

Thus we take T_{ex} = 3.4±1K for both lines respectively. The constant C_0 is 2.257×10^{14} cm^{-2} K km s^{-1} for the 1667 MHz line. The value of C_0 for the 1665 MHz line is 4.0×10^{14} cm^{-2} K km s^{-1}. The computed HI column density is N(HI) = $1.83 \pm 0.01 \times 10^{21}$, where the error is statistical. The column density of OH calculated from the 1667 MHz line is N(OH) = $8 \pm 1 \times 10^{13}$. The column density calculated from the 1665 MHz line is N(OH) = $9 \pm 2 \times 10^{13}$, which is statistically consistent.

4.5.2.1 The OH Non-Detection

After approximately 25 hours of the exploratory search program, faint OH emission was discovered in the first planned sightline (α = $0^h39^m32^s$, δ = $+40^\circ26'$ (J2000)), which had the higher peak brightness temperature in HI (T_{mb} = 30K). We then spent the rest of the observing time searching for OH in a nearby sightline (α = $0^h40^m24^s$, δ = $+40^\circ28'$ (J2000)) with the hope of detecting OH in another position. The second sightline had a peak brightness temperature in HI of T_{mb} = 13K, and thus we expected a weaker signal (see Section 4.6.2). A total of 37 hours of integration time was spent on this sightline; there was no statistically significant detection of OH at 1665, 1667 or 1720 MHz. While the lack of a secondary OH detection is overall disappointing, it is also a confirmation that the detection in the first sightline is not an unknown instrumental effect of the telescope or receiver which might have introduced an erroneous signal. The spectra of both sightline are compared in Fig 4.4.

4.6 Discussion

4.6.1 The Mass of Dark H_2 Traced by OH

While we lack empirical knowledge of the abundance ratio of OH/H_2 in this diffuse molecular gas regime, we can start a rudimentary estimate by assuming a value for the OH/H_2 abundance ratio, we adopt the median literature value of 1×10^{-7} (Liszt and Lucas, 1996; Wiesemeyer et al., 2016; Rugel et al., 2018; Jacob et al., 2019). This value for the abundance ratio appears to hold for $N(\mathrm{OH})$ values as low as $\sim$ a few $\times$ 10^{13} cm^{-2}. Most of the literature values were derived for local, solar metallicity gas. The metallicity in M31 at the galactic radius discussed here ($\sim$ 13 kpc) is statistically consistent with solar metallicity (Sanders et al., 2012).

We stress that the calculation of H_2 mass traced by OH is heavily dependent on the abundance ratio, OH/H_2. While chemical model calculations tend to produce abundance ratio of varying values over differing cloud parameter space (8×10^{-9} to 4×10^{-6}), we adopt the median *observed* literature value of 1×10^{-7} (Nguyen et al., 2018), as observations of the abundance ratio cluster fairly tightly around 1×10^{-7}.

OH is almost always optically thin, we can directly calculate the column density and transform this into a column of H_2. Using the adopted value of the distance from Li et al. (2021), the updated Cepheid distance to M31 is $D = 761 \pm 11$ kpc. Then we can calculate the total mass in the enclosed beam via the equation:

$$M_{\mathrm{H}_2} = N(\mathrm{H}_2)\ A_{\mathrm{H}_2} \mu\ m_{\mathrm{H}} \tag{4.4}$$

where $N(\mathrm{H}_2)$ is the traced H_2 column. $\mathrm{A}_{\mathrm{H}_2}$ is the physical area covered by the GBT beam (which is related to the GBT solid angle and distance to M31 by: $\mathrm{A}_{H_2} = \Omega\ d^2$), μ is the molecular weight which we set to 2 to ignore any contribution to the mass by helium, and m_H is the weight of the hydrogen atom.

The variation of T_{ex} in diffuse clouds is not well known, but the distribution of T_{ex} in Li et al. (2018) is a good starting assumption when we lack coincident absorption and emission profiles. The mass of H_2 traced by OH is: $\mathrm{M}_\odot$ = 2-6 $\times\ 10^7$. For comparison, the amount of mass traced by HI in this same sightline is: $\mathrm{M}_\odot = 3.1 \pm 0.01 \times 10^7$. The mass of H_2 from OH error includes variation in T_{ex} by 1K, and the error in the HI calculation is statistical. Transforming the data to physical units (proton column density per channel) is demonstrated in Fig. 4.5. The CO spectrum is dominated by noise, but the change of axis to a physical unit demonstrates that the molecular gas traced by OH discussed here is 'CO-dark' in nature.

4.6.2 The Relation between OH and HI Revisited

In recent studies, there appears to be a correlation between optically thin HI and faint optically thin OH emission on large spatial scales (Allen et al., 2012; Allen et al., 2013; Busch et al., 2021). A corollary was discussed in Allen et al. (2012) from the data presented from that survey that related the main-beam temperature of HI and OH (1667 MHz) as $\mathrm{T}_{mb}(\mathrm{OH}) = 1.5 \times 10^{-4}\ \mathrm{T}_{mb}(\mathrm{HI})$, with a scatter of 3mK. This relation seems to hold for T_{mb}(HI) < 60K, above which the HI readily saturates, but OH temperature continues to rise because it remains optically thin. As discussed in section 3.2, this relation guided the exploratory search discussed in this paper. The relationship predicts a peak OH signal of 2.6 ± 3 mK in the sightline without a detection, which is consistent with no signal, so perhaps this is not surprising. The sightline with the OH detection was chosen because the predicted peak signal here is 5.3 ± 3mK. In building further extragalactic OH searches, this relationship should be consulted and refined. It is especially unknown how this relationship differs with metallicity, which should be a topic of further research.

4.7 Conclusion

We have detected statistically significant extragalactic emission from faint, thermal (non-maser) OH for the first time. The emission is detected in the southern disk of M31 using very sensitive GBT observations towards one sightline aligned with the major axis, $\sim 62'$ from the nucleus of the galaxy. A non-detection is also presented. The velocity structure of the OH follows closely that of the HI, implying the existence of diffuse H_2 on the same spatial scale as the HI as the large velocity extent is mostly due to galactic rotation. This emission could be potentially related to the detection of the thick disk of dark molecular gas in the 2nd quadrant of the Outer Galaxy of the Milky Way (Busch et al., 2021), as both OH profiles have similar surface brightness' and follow the corresponding HI velocity morphology almost identically.

As receiver technology progressively allows for higher sensitivity to be achieved, single-dish telescopes with large amounts of spare time at cm wavelengths (cm observations can normally be completed in any atmospheric conditions and at any time of day), could systematically search for OH emission in local group galaxies at large galactic radii, where the continuum temperature is slightly above T_{CMB}. While single-beam instruments would potentially require a prohibitive amount of time to survey local group galaxies, new multi-beam phased array feeds (e.g. Roshi et al., 2018; Pingel et al., 2021) could potentially alleviate this issue.

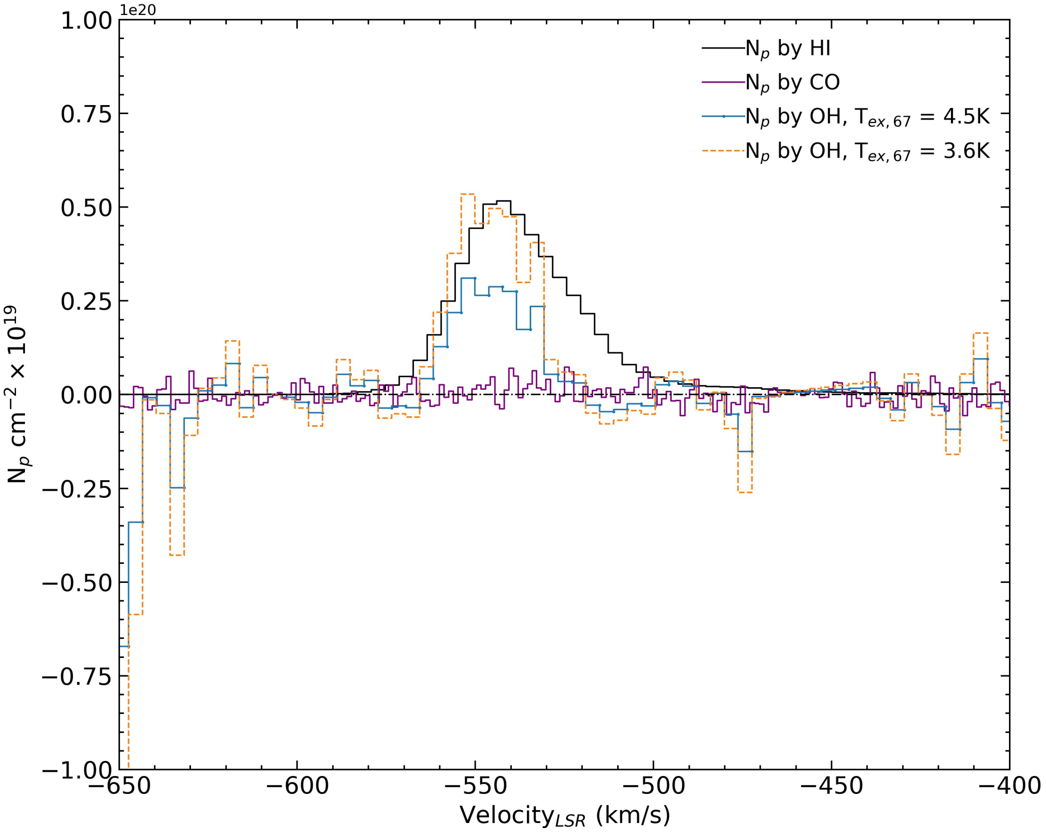

Figure 4.5: HI, OH and CO for the sightline discussed in this paper, transformed into proton (atomic hydrogen for HI, molecular hydrogen for OH, CO) column density per channel (N_p). We use the Galactic X(CO) value suggested from Bolatto, Wolfire, and Leroy (2013). The abundance ratio of $N(\mathrm{OH})/N(\mathrm{H}_2) = 1 \times 10^{-7}$ was used to convert the OH 1667 line to a proton column. The variation of the protons traced by OH with the chosen excitation temperature is demonstrated with two choices of T_{ex}, 4.5K and 3.6K.

References

Allen, R. J., D. E. Hogg, and P. D. Engelke (2015). *AJ* 149.4, p. 14.

Allen, R. J. et al. (2012). *AJ* 143.4, p. 8.

Allen, R. J. et al. (2013). *AJ* 145.3, p. 85.

Baan, W. A. and A. D. Haschick (1987). *ApJ* 318, p. 139.

Beck, R., E. M. Berkhuijsen, and P. Hoernes (1998). *A&AS* 129.2, p. 329.

Bolatto, A. D., M. Wolfire, and A. K. Leroy (2013). *ARAA* 51, pp. 207–268.

Busch, M. P. et al. (2019). *ApJ* 883.2, p. 158.

Busch, M. P. et al. (2021). *ApJ* 914.1, p. 12.

Chastain, R. J., D. Cotten, and L. Magnani (2009). *AJ* 139.1, pp. 267–278.

Dame, T. M. et al. (1993). *ApJ* 418, p. 730.

Dawson, J. R. et al. (2014). *MNRAS* 439.2.

Dickey, J. M. and J. M. Benson (1982). *AJ* 87.2, p. 278.

Dickey, J. M. et al. (2013). *PASA* 30, e003.

Donate, E. and L. Magnani (2017). *MNRAS* 472.3, pp. 3169–3176.

Donate, E., J. White, and L. Magnani (2019). *MNRAS* 486.3, pp. 4414–4422.

Donate, E. et al. (2019). *MNRAS* 486.2, pp. 2281–2289.

Elitzur, M. and Moshe (1990). *ApJ* 363, p. 628.

Elitzur, M. and Moshe (1992). Vol. 170. Astrophysics and Space Science Library. Dordrecht: Springer Netherlands.

Engelke, P. D. and R. J. Allen (2018). *ApJ* 858.

Engelke, P. D. and R. J. Allen (2019). *ApJ* 874.1, p. 49.

Engelke, P. D., R. J. Allen, and M. P. Busch (2020). *ApJ* 901.1, p. 50.

Garwood, R. W. et al. (2006). *ASPC* 351, p. 512.

Goss, W. M. (1968). *ApJS* 15, p. 131.

Grenier, I. A., J.-M. Casandjian, and R. Terrier (2005). *Sci* 307.5713, pp. 1292–1295.

Heiles, C. E. (1968). *ApJ* 151, p. 919.

Hewitt, J. W., F. Yusef-Zadeh, and M. Wardle (2008). *ApJ* 683.1, pp. 189–206.

Heyer, M. and T. M. Dame (2015). *Annu. Rev. Astron. Astrophys* 53, pp. 583–629.

Jacob, A. M. et al. (2019). *A&A* A60.636.

Jacob, A. M. et al. (2020). *A&A* 643.

Li, D. et al. (2015). *PKAS* 30.2.

Li, D. et al. (2018). *ApJS* 235.1, p. 1.

Li, S. et al. (2021).

Liszt, H and R Lucas (1996). *A&A* 314, pp. 917–926.

Liszt, H., J. Pety, and R. Lucas (2010). *A&A* 518, p. 45.

Lockett, P., E. Gauthier, and M. Elitzur (1999). *ApJ* 511.1, pp. 235–241.

Madden, S. C. et al. (2020). *A&A* 643, A141.

Neufeld, D. A. and M. G. Wolfire (2016). *ApJ* 826.2, p. 12.

Nguyen, H. et al. (2018). *ApJ* 862.

O'Neil, K. (2002). *PASP* 278, pp. 293–311.

Penzias, A. A. (1964). *AJ* 69, p. 146.

Pineda, J. L. et al. (2013). *A&A* 554.

Pingel, N. M. et al. (2021). *AJ* 161.4, p. 163.

Planck Collaboration et al. (2011). *A&A* 536, p. 16.

Prestage, R. M. et al. (2015). *2015 USNC-URSI Radio Science Meeting (Joint with AP-S Symposium)*. IEEE, pp. 294–294.

Radhakrishnan, V (1967). *Aust. J. Phys.* 20, p. 203.

Roshi, D. A. et al. (2018). *AJ* 155.5, p. 202.

Rugel, M. R. et al. (2018). *A&A*.

Sanders, N. E. et al. (2012). *ApJ* 758.2, p. 133.

Schmelz, J. T. and W. A. Baan (1988). *AJ* 95, p. 672.

Tang, N. et al. (2021). *ApJS* 252.1, p. 1.

Wannier, P. G. et al. (1993). *ApJ* 407, p. 163.

Weaver, H. et al. (1965). *Nature* 208.5005, pp. 29–31.

Weinreb, S. et al. (1963). *Natur* 200.4909, pp. 829–831.

Weselak, T. et al. (2010). *MNRAS* 402.3, pp. 1991–1994.

Wiesemeyer, H. et al. (2016). *A&A* 585, p. 18.

Winkel, B. et al. (2015). *A&A* 585, p. 22.

Wolfire, M. G., D. Hollenbach, and C. F. McKee (2010). *ApJ* 716.2.

Wood, P. R., M. S. Bessell, and J. B. Whiteoak (1986). *ApJL* 306, p. L81.

Wood, P. R. et al. (1992). *ApJ* 397, p. 552.

Xu, D. and D. Li (2016). *ApJ* 833.1, p. 90.

Yang, B. et al. (2010). *ApJ* 718, pp. 1062–1069.

Zheng, Z. et al. (2020). *MNRAS* 499.3, pp. 3085–3093.

Chapter 5

Epilogue

While my scientific work in observing and searching for OH in our Galaxy and beyond is far from over, this nominally concludes the thesis. I hope you find the results and discussion presented intriguing and stimulating; I have had quite the adventure in studying them.

I look forward to continuing my study of the interstellar medium as a postdoctoral research at Australian National University starting in 2022 under the supervision of Dr. Naomi McClure-Griffiths.

Vita

Michael P. Busch was born on May 20th, 1994 in Los Angeles, California. He graduated from Casa Verde High School in Casa Grande, Arizona in 2012. In the fall of 2012, he began his undergraduate studies at Arizona State University (ASU). In the summer of 2015, he was awarded a REU position at University of Michigan and studied under Prof. Eric Bell. In the summer of 2016, he worked under the supervision of Prof. Ralf-Juergen Dettmar and Prof. Marcus Bruggen at the University of Hamburg. He received a B.S. in Astrophysics and a B.S. in Physics from ASU in 2016, where he studied under Prof. Judd Bowman of the School of Earth and Space Exploration. He began his graduate studies at at the Physics and Astronomy Department of Johns Hopkins University in the fall of 2016. He was awarded a NSF Graduate School Research Fellowship starting in 2016. He began his graduate studies on observational cosmology under Prof. Adam Riess until the Spring of 2019. He then studied under the late Space Telescope Science Institute (STScI) Emeritus Astronomer, Ron Allen on using the OH molecule to trace dark molecular gas for his thesis work. After the passing of Ron Allen in the fall of 2020, he worked under the guidance of STScI Astronomer Joshua Peek on finishing his thesis work.